

A Thesis Submitted for the Degree of PhD at the University of Warwick

Permanent WRAP URL:

<http://wrap.warwick.ac.uk/157499>

Copyright and reuse:

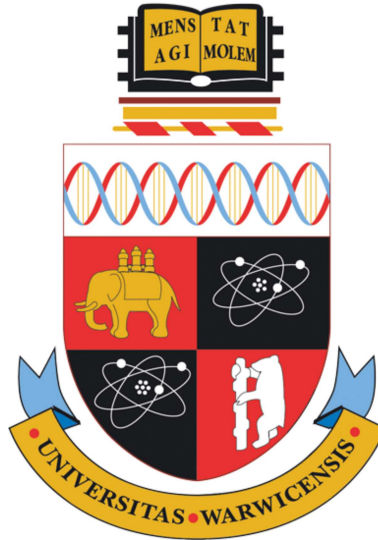
This thesis is made available online and is protected by original copyright.

Please scroll down to view the document itself.

Please refer to the repository record for this item for information to help you to cite it.

Our policy information is available from the repository home page.

For more information, please contact the WRAP Team at: wrap@warwick.ac.uk



Flight Control of Very Flexible Unmanned Aerial Vehicles

by

Pengyuan Qi

Thesis

Submitted to the University of Warwick

for the degree of

Doctor of Philosophy

School of Engineering

December 2019

THE UNIVERSITY OF
WARWICK

*Delicated
to
my parents and the memory of my grandparents*

Contents

List of Tables	v
List of Figures	vi
Acknowledgments	xii
Declarations	xiii
Abstract	xv
Abbreviations	xvii
Chapter 1 Introduction	1
1.1 Background	1
1.2 Review of Aeroelastic Modelling and Control	6
1.2.1 Aeroelastic Modelling	7
1.2.2 Aeroelastic control	13
1.3 Motivations and Research Contributions	15
1.4 Outline of Thesis	17
Chapter 2 Modelling of the very flexible flying wing	19
2.1 Intrinsic Beam Equations	19
2.2 Modal Aeroservoelastic Description	21
2.3 Model Order Reduction	22
2.4 Test Case	24
2.5 Conclusions	27
Chapter 3 Aeroelastic and Trajectory Control	28
3.1 Introduction	28
3.2 Control System Design	30

3.2.1	Inner-Loop H_∞ Control Design	33
3.2.2	Outer-Loop LADRC Control Design	36
3.3	Simulation Study	41
3.3.1	Stability Analysis	41
3.3.2	Step Response	43
3.3.3	Trajectory Tracking Performance	46
3.3.4	Gust Response	46
3.3.5	Continuous turbulence response	52
3.4	Conclusions	57
Chapter 4	Autonomous Landing Control using Lidar Preview	58
4.1	Introduction	58
4.2	Landing Trajectory Design	61
4.3	Lidar Simulator Design	63
4.3.1	Line-of-Sight Wind Measurement	63
4.3.2	Three-dimensional Wind Measurement	65
4.4	Control Design	67
4.4.1	Inner-Loop H_∞ Preview Control Design	69
4.4.2	Outer-loop Control Design	74
4.5	Simulation Results	74
4.5.1	Robustness against Modeling Uncertainties	75
4.5.2	Lidar Wind Measurement	76
4.5.3	Wind Turbulence Response	77
4.5.4	Modal Analysis	82
4.5.5	Measurement Noise Analysis	85
4.6	Conclusions	88
Chapter 5	Data-driven Flight Control	89
5.1	Introduction	90
5.2	Guidance System	93
5.3	Control System	94
5.3.1	MFAC Algorithm Preliminaries	95
5.3.2	Longitudinal Inner-loop Control Design	98
5.3.3	Lateral Inner-loop Control Design	100
5.3.4	Longitudinal Outer-loop Control Design	101
5.3.5	Stability Analysis	101
5.4	Simulation Results	101
5.4.1	Step Response	102

5.4.2	Disturbance Rejection	102
5.4.3	Robust Performance	108
5.4.4	Path following in Turbulence	108
5.5	Conclusions	116
Chapter 6	Conclusions and Future Work	117
6.1	Conclusions	117
6.2	Future Work	119

List of Tables

1.1	Key properties of example prototype HALE UAVs.	4
2.1	Definition of measurement outputs	26
2.2	Natural frequencies of the first few structural modes. The number of the first structural mode starts from seven as modes 1~6 are the rigid-body ones.	26
3.1	Coordinates of the waypoints.	46
4.1	Modal energy contributions and degrees of performance improvements by preview control.	84

List of Figures

1.1	<i>The Solar Impulse 2 aircraft.</i>	2
1.2	Examples of prototype HALE UAVs	3
1.3	Structure failure of the <i>Helios</i> .	5
1.4	The XHALE very flexible aircraft.	12
2.1	Illustration of the very flexible flying wing.	20
2.2	Geometric configuration and control surfaces on the aircraft: simultaneous flaps (δ_1), symmetric (δ_2) and antisymmetric (δ_3) differential flaps, simultaneous thrust (f_{T1}), and symmetric (f_{T2}) and antisymmetric (f_{T3}) differential thrust.	25
3.1	Control structure of the aeroelastic and trajectory control system. H , S , θ , V , ϕ , bm and tw denote the altitude, lateral displacement, pitch angle, forward velocity, roll angle, symmetric root bending measurement and anti-symmetric twist measurement respectively. The subscript r denotes the reference command, while $\dot{\bullet}$ denotes time derivative. K_{lon} and K_{lat} are the H_∞ controllers. ESO_H and ESO_S are the extended state observers (ESO) in LADRC. K_{hp} , K_{hd} , K_{sp} , K_{sd} , K_{vp} and K_{vi} are the controller parameters.	31
3.2	Standard H_∞ tracking problem. d , r , u_c , e , z denote the external disturbance, reference command, control input, error signal, and weighted output, respectively. y_m is the measurement output. \mathbf{G} and \mathbf{C} are the transfer functions of the plant and the H_∞ controller.	33
3.3	Convergence of the PSO algorithm. The algorithm converges after about 25 iterations in this case.	37

3.4	The structure of LADRC. The variables r , e , \hat{y} , \hat{y}_* , y , d denote the reference command, error signal, estimated state of the plant, extended estimated disturbance, output and disturbance applied to the plant, respectively. The variables u_0 , u_* , u denote the original control input computed by the linear control law, the compensated input computed by the control compensator and the actual control inputs to the plant, respectively.	38
3.5	Simplified model of the lateral motion. The dashed line denotes the desired flight path and the solid line denotes the actual flight path. The lateral displacement is defined as the lateral deviation of the aircraft's current position to the desired flight path.	40
3.6	Low frequency poles in the test case. The poles are obtained based on the linear reduced-order model.	42
3.7	Bode diagram of the altitude control system and the lateral displacement control system. The left pair is the Bode diagram of altitude control system while the right pair is that of the lateral displacement control system.	43
3.8	Step response of the altitude. δ_1 , δ_2 , f_{T1} , f_{T2} are the control actions of the simultaneous flap, symmetric differential flap, simultaneous thrust and symmetric differential thrust, respectively, as defined in Fig. 2.2.	44
3.9	Step response of the lateral displacement. δ_3 and f_{T3} are the control actions of the antisymmetric differential flap and the antisymmetric differential thrust respectively, as defined in Fig. 2.2.	45
3.10	Trajectory tracking performance. The red solid line indicates the desired flight path, which are defined by the actual geographic longitude, latitude and altitudes, the blue dot-dashed line indicates the actual flight path. The red asterisks denote the defined multiple waypoints A to E.	47
3.11	DARPA discrete gust velocity distribution with respect to position and time. The gust duration is $t_g = 1s$ in this figure.	48
3.12	Gust wind response with gust applied in the vertical direction.	49
3.13	Gust wind response of lateral variables with gust applied in the lateral direction.	50
3.14	Gust wind response of longitudinal variables with gust applied in the lateral direction.	51

3.15	Altitude responses of a flying wing with two different types of controller (LADRC vs PID) in the longitudinal outer loop.	52
3.16	Time history of the wind turbulence used in simulations. From top to bottom are the lateral, forward and vertical components, respectively.	53
3.17	Responses with 3D turbulence applied. In the upper two subfigures, the trajectories of the center of gravity and the center of the flying wing are plotted.	54
3.18	Control inputs of the responses with 3D turbulence applied.	55
3.19	Instantaneous shape of the flying wing during flight in the presence of von Kármán turbulence. The upper, middle and lower subfigures are the side view, front view and 3D view, respectively.	56
4.1	Illustration of the landing process. R_0 is the projected distance from the final approach phase start point P_A to the desired touchdown point O . P_B is the flare phase start point and O is the desired touchdown point. γ_L is the descent flight path angle in the final approach phase.	61
4.2	Structure of the landing trajectory generator. Pre-defined parameters include the projected travelling distance since entering the final approach phase (R), the projected distance from the final approach phase starting point to the desired touchdown point (R_0), altitude of the final approach phase starting point (H_0) and the flare phase starting point (H_1), the descent flight path angle (γ_L) and the desired vertical speed at the touchdown point (v_{zr}). H is the aircraft's current altitude.	63
4.3	Illustration of the line-of-sight measurement.	64
4.4	Illustration of the Lidar scanning pattern. w_u, w_v, w_w are the respective mean value of the three-dimensional velocity components of the wind disturbance in the measurement plane. The number of measurement points is assumed to be 12 in this work.	65
4.5	Illustration of the measurement data fitting. The asterisks denote the set of LOS measurement data during a scanning cycle, the solid line is the fitted function.	66

4.6	Structure of the preview-based landing control system: the upper part is for the longitudinal channel while the lower part is for the lateral channel. Output feedback signals are altitude H , lateral displacement S , forward velocity V , pitch angle θ , roll angle ϕ , root bending moment bm and twist moment tw . R is the travelling distance since entering the final approach phase. ESO_{lon} and ESO_{lat} are the extended state observers (ESO) in the outer-loop LADRC controller. \hat{d} is the actual wind disturbance at a distance in front of the aircraft, \tilde{d}_i is the Lidar wind measurements with the subscript $i = 1, 2, 3$ denotes the lateral, forward and vertical component, respectively. d is the wind disturbance that actually impact the aircraft, and Φ is the delay chain. K_{lonp} and K_{latp} are the H_∞ preview controllers in the longitudinal and lateral channel, respectively. The subscript symbol r denotes the reference command, while the $\dot{\bullet}$ symbol denotes time derivative. K_{hp} , K_{hd} , K_{sp} , K_{sd} , K_{vp} and K_{vi} are the corresponding controller parameters.	68
4.7	H_∞ tracking problem with Lidar preview. \hat{d} , \tilde{d} , d , r , u_c denote the wind disturbance in front of the aircraft, wind measurements from Lidar, the wind disturbance actually impact the aircraft, reference commands and control inputs, respectively. $z_{i=1,2,3}$ are the performance outputs, y_m is the measurement output. Φ is the N -step delay chain. G and K are the transfer functions of the plant and the preview controller.	70
4.8	Pitch responses of the preview control system based on three types of very flexible configurations with varying bending stiffness.	75
4.9	Sample series of the three-dimensional synthetic turbulence at $h = 5m$ with $w_{20} = 5m/s$ and the corresponding Lidar wind measurements. w_u, w_v, w_w denote the lateral, forward and vertical component of the wind disturbance, respectively.	77
4.10	Time histories of the landing trajectories with the preview-based and non-preview landing control systems in the presence of three-dimensional turbulence. The green cross symbol denotes the flare phase starting point. The altitude response without wind turbulence is also plotted in the top diagram.	78
4.11	Time histories of the aircraft responses by the preview-based control system with measurement noise in the Lidar system.	80

4.12	Time histories of the control actions by the preview-based control system with measurement noise in the Lidar system.	81
4.13	Trajectories of the center of gravity (cg) and the center of the flying wing (cw) during landing.	82
4.14	Modal amplitudes of the first symmetric out-of-plane bending mode with and without preview-based landing control systems in the landing simulations.	83
4.15	Time histories of the aircraft responses using noisy Lidar wind measurements as prior information to the preview control system. In the top diagram, only the first 50 seconds of the Lidar wind measurements of the non-stationary crosswind are plotted for better view of the measurement noises.	85
4.16	Time histories of the aircraft responses with the preview-based and non-preview landing control systems in the presence of wind turbulence.	86
4.17	Time histories of the control actions with the preview-based and non-preview landing control systems in the presence of wind turbulence.	87
5.1	Illustration of the guidance system. The blue solid line denotes the predefined route.	93
5.2	Control structure of the data-driven flight control system. \dot{H}, θ, V, bm and ϕ are the climb rate, pitch angle, forward velocity, root bending moment and roll angle, respectively. X, Y, Z are the geometric position of the aircraft. The subscript symbol r denotes the reference command. MFAC-H, PD-MFAC-Lon and PD-MFAC-Lat denote the longitudinal outer-loop climb rate controller, the longitudinal inner-loop controller and the lateral inner-loop controller, respectively. . .	94
5.3	Control structure of the cascaded PD-MFAC-MIMO algorithm. \mathbf{G} denotes the unknown nonlinear system plant.	99
5.4	Equivalent control structure of the cascaded PD-MFAC-MIMO algorithm. \mathbf{P} denotes the augmented system plant consisting of the original system plant and the damping terms.	101
5.5	Step response of the inner-loop control system designed using the PD-MFAC approach and the original MFAC approach, respectively.	103
5.6	Time history of the synthetic von Kármán turbulence. u, v, w denote the lateral, forward and vertical component, respectively.	104

5.7	Time histories of the altitude, lateral displacement and forward velocity responses with the data-driven and H_∞ control systems in the presence of wind turbulence.	105
5.8	Time histories of the pitch, roll, bending moment, left wingtip and right wingtip responses with the data-driven and the H_∞ control systems in the presence of wind turbulence.	106
5.9	Time histories of the control inputs with the data-driven and the H_∞ control systems in the presence of wind turbulence.	107
5.10	Time histories of the altitude, lateral displacement, forward velocity and pitch response with the data-driven and the H_∞ control systems in turbulence, based on two very flexible configurations with varying bending stiffness.	109
5.11	Time histories of the roll angle, bending moment, left wingtip and right wingtip response with the data-driven and the H_∞ control systems in turbulence, based on two very flexible configurations with varying bending stiffness.	110
5.12	Time histories of control inputs with the data-driven and the H_∞ control systems in turbulence, based on two very flexible configurations with varying bending stiffness.	111
5.13	Time histories of the responses with the data-driven control system for path-following in the presence of wind turbulence.	112
5.14	Time histories of the control actions with the data-driven control system for path-following in the presence of wind turbulence.	113
5.15	Modal amplitudes of the rigid-body modes with the data-driven control systems for path-following in presence of wind turbulence.	114
5.16	Modal amplitudes of the first five dominant flexible modes with the data-driven control systems for path-following in presence of wind turbulence.	115
1	Illustration of the waypoint tracking.	125

Acknowledgments

I would like to express my sincere gratitude and great respect to my supervisor Prof. Xiaowei Zhao for his guidance and encouragement throughout my four-year Ph.D study. He is not only a supervisor on academic research but also an excellent friend sharing wisdoms in all aspects of life. I would also like to thank Dr. Yinan Wang for his selfless help and advice.

Declarations

This thesis is submitted to the University of Warwick in support of my application for the degree of Doctor of Philosophy. It has been composed by myself and has not been submitted in any previous application for any degree.

Parts of this thesis have been published by the author:

Journal (Peer Reviewed)

1. P. Qi, X. Zhao, Y. Wang, R. Palacios and A. Wynn, Aeroelastic and trajectory control of High Altitude Long Endurance aircraft, *IEEE Transactions on Aerospace and Electronic systems*, vol. 54, no. 6, pp. 2992-3003, 2018.
2. P. Qi, X. Zhao, and R. Palacios, Autonomous landing control of highly flexible aircraft based on Lidar preview in the presence of wind turbulence, *IEEE Transactions on Aerospace and Electronic systems*, vol. 55, no. 5, pp. 2543-2555, 2019.
3. P. Qi, and X. Zhao, Flight control for very flexible aircraft using Model Free Adaptive Control, *Journal of Guidance, Control, and Dynamics*, vol. 43, no. 3, pp. 608-619, 2020.

Conference (Peer Reviewed)

1. P. Qi, Y. Wang, X. Zhao, R. Palacios, and A. Wynn, Trajectory control of a very flexible flying wing, *2017 American Control Conference*, Seattle, USA, May 2017.
2. P. Qi, X. Zhao, Y. Wang, R. Palacios, and A. Wynn, Automatic landing control of a very flexible flying wing, *2018 American Control Conference*, Milwaukee, USA, June 2018.

3. P. Qi, X. Zhao, and R. Palacios, Preview-based altitude control for a very flexible flying wing, *2018 IEEE Conference on Decision and Control*, Miami, USA, December 2018.

Abstract

This thesis aims to investigate the flight control of a very flexible flying wing model already developed in the literature. The model was derived from geometrically nonlinear beam theory using intrinsic degrees of freedom and linear unsteady aerodynamics, which resulted in a coupled structural dynamics, aerodynamics, and flight dynamics description. The scenarios of trajectory tracking and autonomous landing in the presence of wind disturbance are considered in control designs.

Firstly, the aeroelastic and trajectory control of this very flexible flying wing model is studied. The control design employs a two-loop PI/LADRC (proportional-integral/linear active disturbance rejection control) and H_∞ control scheme, based on a reduced-order linear model. The outer loop employs the PI/LADRC technique to track the desired flight paths and generate attitude commands to the inner loop, while the inner loop uses H_∞ control to track the attitude command and computes the corresponding control inputs. The particle swarm optimization algorithm is employed for parameter optimization in the H_∞ control design to enhance the control effectiveness and robustness. Simulation tests conducted on the full-order nonlinear model show that the designed aeroelastic and trajectory control system achieves good performance in aspects of tracking effectiveness and robustness against disturbance rejection.

Secondly, the preview-based autonomous landing control of the very flexible flying wing model using light detection and ranging (Lidar) wind measurements is studied. The preview control system follows the above two-loop control structure and is also designed based on the reduced-order linear model. The outer loop em-

employs the same LADRC and PI algorithms to track the reference landing trajectory and vertical speed, respectively. But the inner loop is extended to introduce Lidar wind measurements at a distance in front of the aircraft, employing H_∞ preview control to improve disturbance rejection performance during landing. Simulation results based on the full-order nonlinear model show that the preview-based landing control system is able to land the aircraft safely and effectively, which also achieves better control performance than a baseline landing control system (without preview) with respect to landing effectiveness and disturbance rejection.

Finally, the data-driven flight control of the very flexible flying wing model using Model-Free Adaptive Control (MFAC) scheme to reduce the dependence of control design on system modeling is studied. A cascaded proportional-derivative MFAC (PD-MFAC) approach is proposed to accommodate the MFAC scheme in a flight control problem, which shows better control performance over the original MFAC algorithm. Based on the PD-MFAC approach, the data-driven flight control system is developed to achieve gust load alleviation and trajectory tracking. Simulation results based on the full-order nonlinear model show that the proposed data-driven flight control system is able to properly regulate all the rigid-body and flexible modes with better effectiveness and robustness (against disturbance rejection and modeling uncertainties), compared to a baseline H_∞ flight control system.

Abbreviations

ARE	algebraic Riccati equation
BIBO	bounded-input bounded-output
CASTC	China Aerospace Science and Technology Corporation
CFD	computational fluid dynamics
CFDL	compact form dynamic linearization
DARE	discrete-time algebraic Riccati equation
DOF	degree-of-freedom
ERAST	Environmental Research Aircraft and Sensor Technology
EOM	equation of motion
ESO	extended state observer
FFDL	full form dynamic linearization
FI	full information
GLA	gust load alleviation
GPS	global positioning system
HALE	High Altitude Long Endurance
LADRC	linear Active Disturbance Rejection Control

Lidar	light detection and ranging
LOS	line-of-sight
LQG	linear quadratic Guassian
LQR	linear quadratic regulator
LTR	loop transfer recovery
MFAC	Model-Free Adaptive Control
MIMO	multiple-input multiple-output
MISO	multiple-input single-output
MPC	model predictive control
NASA	National Aeronautics and Space Administration
OF	output feedback
PD-MFAC	proportional-derivative Model-Free Adaptive Control
PFDL	partial form dynamic linearization
PID	proportional-derivative-integral
PPD	pseudo partial derivative
PSO	particle swarm optimization
RMS	root mean square
SISO	single-input single-output
SNR	signal-to-noise ratio
UAV	unmanned aerial vehicle
UVLM	unsteady vortex lattice method
VAD	velocity azimuth display

VFA	very flexible aircraft
VTP	virtual target point
2-D	two-dimensional
3-D	three-dimensional

Chapter 1

Introduction

1.1 Background

Unmanned Aerial Vehicle (UAV) is a type of aircraft without human pilot on board and can fly with different levels of autonomy, operated either remotely by a human pilot through the ground control system or autonomously by the airborne flight control system. With rapid advances in relevant technology in the disciplines of materials science, control engineering, communication, computer science, etc., the performance of UAVs has seen a significant development over the past few decades, which enables them with better capability to be applied in various fields [1, 2]. In the military field, UAVs have been deployed to carry out multiple types of missions, such as intelligence, electronic attack, strike missions and so forth, making them a vital tactical weapon on modern battlefields. While in the civilian field, UAVs can replace human in dangerous or repeated labour tasks, for example, industrial inspection, surveying and mapping, search and rescue, agricultural monitoring, etc., in which UAVs have shown their capacities to improve industrial efficiency and boost economic growth.

Flight endurance is one of the many key specifications to evaluate an aircraft's performance. It is defined as the amount of time an aircraft can continuously fly in the air without landing. Longer endurance typically means longer continuous mission time. In general, the flight endurance ranges from dozens of minutes to dozens of hours depending on the categories of the aircraft (without considering in-flight refuelling). It has long been a challenging research target to pursue significantly extended flight endurance. At the moment, the electric solar-powered platforms are very promising candidates. A well-known solar-powered aircraft is the *Solar Impulse 2* as shown in Fig. 1.1, which successfully completed its circumnav-

igation of the globe in July 2016 using only solar energy. During this journey, the longest flight duration was 117 hours 52 minutes in its travel from Japan to Hawaii. The Solar-powered aircraft gather solar energy during the day to power the whole system and simultaneously save extra energy into the batteries, on which the aircraft rely to continue flying during the night. In this manner, the flight endurance can be significantly increased. Given an appropriate design, endurance of months or years, even perpetual flight might be achieved [3–5]. However, the design of such solar-powered aircraft is not a simple replacement of relevant systems on a conventional aircraft, but requires careful and comprehensive consideration. In order to achieve the endurance target, the solar-powered aircraft need to be designed with extreme aerodynamic efficiency, which is usually done by employing light-weight materials to reduce the structural weight, as well as high aspect-ratio wings to increase the lift-to-drag ratio [6, 7].



Figure 1.1: *The Solar Impulse 2 aircraft.*

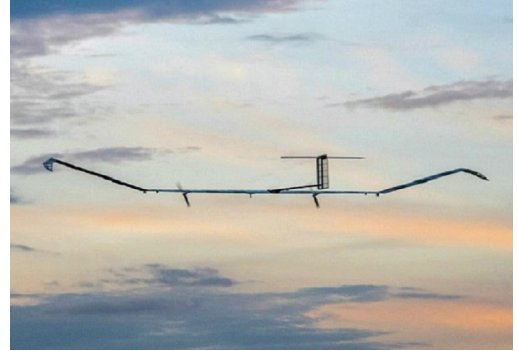
On the other hand, the service ceiling, namely the maximum altitude at which an aircraft can maintain a specified climb rate, is another important specification to reflect an aircraft’s performance. Generally, flying at high altitudes provides a large mission coverage area and reduces the disrupts from other airborne traffic or threats from hostile air vehicles. Since the air gets thinner and smoother at high altitudes, the aircraft can travel more efficiently because of less air resistance, and can also face less safety concerns caused by wind disturbance. Particularly for solar-powered aircraft, solar cells can absorb and convert more energy because of the clear weather condition at high altitudes. Combining the aforementioned factors eventually lead to the concept of High Altitude Long Endurance (HALE) UAVs.

The HALE UAVs are designed to optimally operate at high altitudes (typically 15~30 *km*) with considerable endurance. Due to their advantages of long

endurance, low cost and easy maintenance, the HALE UAVs have huge potential in undertaking a wide range of military and civilian missions [8–10], such as long-range telecommunication relay, aerial surveillance, internet beaming, storm tracking studies, etc., offering an alternative to the satellite technology that is currently used in these fields. In the past few decades, several experimental prototype HALE UAVs have been built to demonstrate their performance. Among them, some well-known examples include the *Helios* (see Fig. 1.2a) developed by AeroVironment under NASA’s ERAST programme, the *Zephyr* (see Fig. 1.2b) developed by QinetiQ which holds the current endurance record of two weeks for solar-powered UAVs [11], the *Aquila* (see Fig. 1.2c) developed by Ascenta (now acquired by Facebook), and the *Rainbow Solar UAV* (see Fig. 1.2d) developed by CASTC which successfully completed its maiden flight and reached the near space in 2017. At the time of writing (November 2019), other HALE UAVs are also reported to be under development. For example, the BAE Systems and Prismatic are collaborating to build the PHASA-35 UAV which aims to stay airborne for one year and offer persistent low-cost service. The main properties of these mentioned HALE UAVs are summarized in Table 1.1.



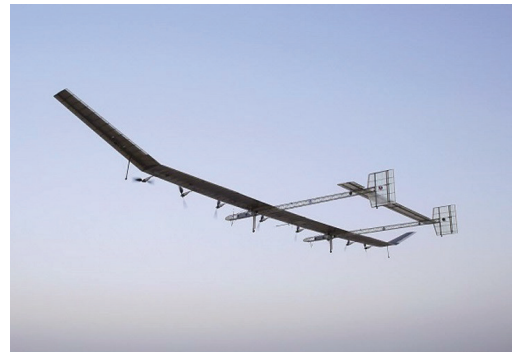
(a) Helios



(b) Zephyr



(c) Aquila



(d) Rainbow Solar UAV

Figure 1.2: Examples of prototype HALE UAVs

Table 1.1: Key properties of example prototype HALE UAVs.

	Wing span (m)	Weight (kg)	Aspect ratio	Configuration
Helios	75	1052	≈ 31	flying wing
Zephyr	22.5	53	> 20	wing-body-tail
Aquila	42	400	> 35	flying wing
Rainbow	45	- ¹	-	wing-body-tail
PHASA-35	35	150	-	wing-body-tail

Among them, the *Helios* prototype series are considered to have laid the foundations of this research area. The *Helios* has a wing-span of 75 *m* (the aspect-ratio is around 31) which is larger than the wing-span of a Boeing 747 (68 *m*), but only weighs approximately 1052 *kg* while Boeing 747 has a weight of over 320 tonnes. The aircraft employs a flying wing configuration, the control surfaces mounted on the airframe consist of 14 electric motors and 72 trailing-edge elevators providing necessary thrust and control torque. The aircraft was designed to have an endurance of more than 24 hours and reached the altitude of 29,524 *m* in 2001, which is still the world record ever made by winged aircraft [12]. Unfortunately, the *Helios* prototype crashed in a mission in 2003, due to the encountered turbulence forced the aircraft into a persistent high-dihedral configuration which caused unstable dynamics in a very divergent pitch mode, the airspeed then exceeded its design value and eventually led to substantial structure failure, as indicated in Figure 1.3. It is afterwards recognized that conventional linear methodologies are not capable of analysing the complex interactions on the aircraft’s characteristics [13]. Therefore, one of the key recommendations in the investigation report to this accident [13] emphasized the need to: “Develop more advanced, multidisciplinary (structures, aeroelastic, aerodynamics, atmospheric, materials, propulsion, controls, etc.) time-domain analysis methods appropriate to highly flexible, morphing vehicles.”, which is still very constructive to the development of this research area nowadays.

Another prototype whose progress does not go smoothly is the Facebook *Aquila*, which was intended to act as relay stations to beam internet to rural areas. The *Aquila* has a wing span of 42 *m* (the aspect-ratio is around 35) and weighs only around 400 *kg*. The aircraft employs a swept-wing configuration and is designed to operate at altitudes between 18~27 *km* with the endurance of up to three months. In June 2016, *Aquila* took its first flight and completed a 96-minute flight

¹The symbol “-” indicates the specific data is not available.

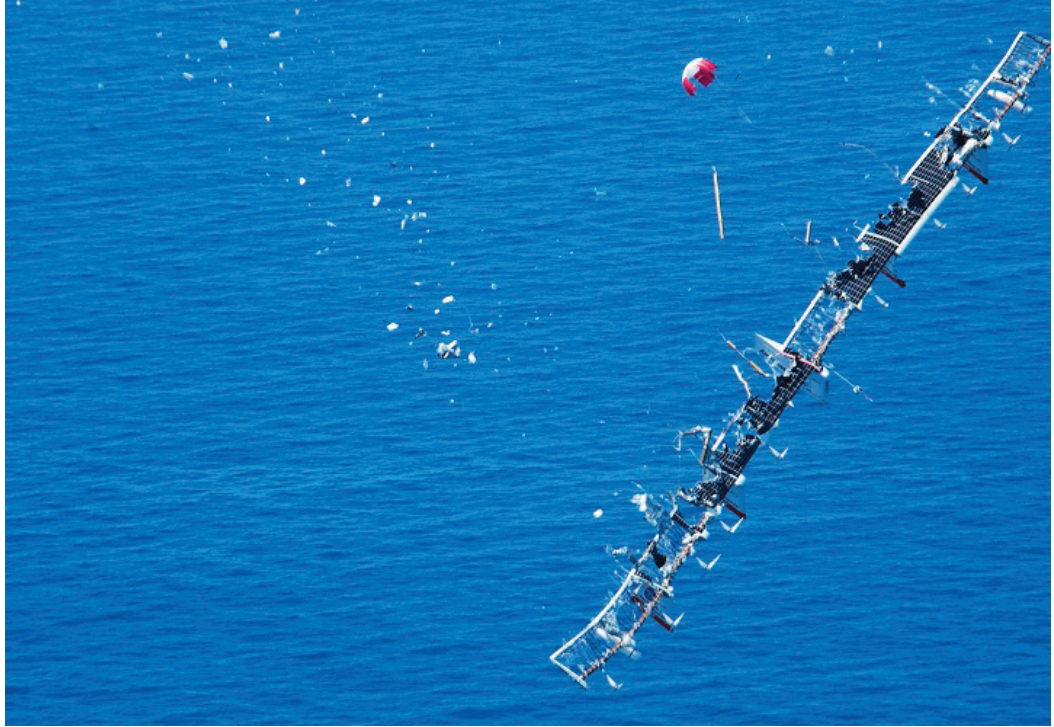


Figure 1.3: Structure failure of the *Helios*.

successfully, but was reported to experience a crash upon landing [14], as a result of the unexpected strong gust wind lifted the aircraft above its flight path right before touchdown, causing the control system reacted to lower the nose, the aircraft then speeded up to hit the ground and ended with substantial damage in its right wing [15].

In brief, despite the progress made by experimental designs of various prototypes, the lack of a comprehensive understanding into the complex dynamics exhibited in HALE aircraft has ultimately led to these disastrous accidents. It is therefore imperative to promote research into the coupled nonlinear aeroelastic and flight dynamic behaviours of HALE aircraft. Essentially, the use of light-weight high-aspect-ratio wings (to meet the efficiency targets) significantly reduces structure stiffness and leads to a very flexible aircraft (VFA), of which the dynamic responses are very different from those of rigid ones. Due to the inherent high flexibility of the airframe, the aerodynamic load will considerably deform the wing shape during flight and affect the stability of the aircraft. Furthermore, considering the fact that the aeroelastic effect can be slow enough to excite rigid-body instabilities, there exists an overlap in the lowest elastic mode frequencies and the rigid-body flight dynamic frequencies [16], resulting in strong couplings between the structural

dynamics, aerodynamics and flight dynamics. These aspects not only imply the demand for advanced analysis methods, but also pose great challenges in terms of airframe modelling and dynamic control [16–25] of VFA.

To be specific, for airframe modelling, since the dynamics associated with large structural deformations are geometrically nonlinear, standard linear theories and analysis tools are no longer adequate to accurately capture these effects [26,27]. It is necessary to develop a nonlinear simulation framework to account for the geometrically-nonlinear structural behaviours, coupled with proper aerodynamic descriptions. Moreover, such aeroelastic formulations typically incorporate thousands of degrees-of-freedom (DOF) and have to be reduced to manageable size for the purpose of control design and time-domain simulations, which further requires nonlinear model reduction on both the structural and aerodynamic models. With regards to dynamic control, since VFA are very sensitive to atmospheric disturbance, one of the major challenges focuses on the design of flight control strategies for dynamic stabilization, gust load alleviation (GLA) and trajectory tracking, subject to the coupled aeroelastic response and flight dynamics. The designed control system must be able to properly regulate the rigid-body modes as well as the flexible modes, especially in the presence of wind disturbance. In addition, it is crucial to ensure the flight control system with sufficient robustness against modelling uncertainties and unmodelled dynamics for them to serve in practice.

These are the main challenges that have motivated relevant research in this field. Developing efficient methods to address these challenges are beneficial to other research areas as well, such as the modelling and control of flapping wing aircraft [28–32], helicopter and wind turbine with large slender blades [33–37], where the geometrically-nonlinear aeroelastic effect also constitutes the key challenges.

1.2 Review of Aeroelastic Modelling and Control

Aeroelasticity in aeronautics concerns the interactions between structural dynamics, unsteady aerodynamics and flight dynamics. To study the nonlinear aeroelastic characteristics of very flexible aircraft (VFA), considerable efforts have been devoted into the research area of aeroelastic modelling and dynamic control during the past few decades. In this section, we will try to provide a brief overview of the recent developments in these two aspects. First, we will review the aeroelastic modelling methods which are relevant to those used in this work, specifically, the geometrically nonlinear structural modelling methods and the unsteady aerodynamics modelling methods. The existing aeroelastic formulation frameworks will also be reviewed.

Subsequently, we will review the studies on the active aeroelastic control for VFA.

1.2.1 Aeroelastic Modelling

The earliest example of work to study the aeroelasticity of slender wings was conducted by Goland [38]. In this work, linear structural model and unsteady aerodynamic theory were used to model the pure aeroelastic behaviour of a low-aspect-ratio wing in cantilever configuration, the flight dynamics were assumed to be neglected. This work studied the predictions of flutter speed and frequency and has been widely used as benchmark test case for aeroelastic analysis.

Tang et. al. [39] studied the limit cycle oscillations and flutter response of a high-aspect-ratio cantilevered wing, in which the structural model was developed using nonlinear beam models and the aerodynamics was described by the combination of ONERA aerofoil model and strip theory. Experiment tests were carried out in a wind tunnel to validate the theoretical model. Through comparisons with collected experiment data, the static deflections predicted by the nonlinear beam model were observed to be more consistent than those predicted by the linear model, which demonstrated the necessity of using nonlinear beam models for the structural modeling of slender wings. In particular, the modeling of VFA requires the incorporation of coupled structural dynamics, aerodynamics and flight dynamics to describe the aeroelastic response. Due to the high flexibility of the airframe, VFA typically exhibit large structural deformations during flight, the aircraft's dynamics are significantly affected by the resulting geometrical nonlinearities. Since standard linear solutions are based on the assumption of small structural deformations, the nonlinear structural modelling of VFA should be able to capture such nonlinear interactions.

Very high-fidelity approaches based on nonlinear 3-D finite element method [40–42] and nonlinear plate model [43] have been investigated. However, it is generally acknowledged that such methods require very high computational costs for full aircraft dynamics analysis and suffer from numerical problems. As structures undergoing large deformations by nature have dominant dimensions, a fidelity reduction is possible using geometrically-nonlinear composite beam or shell theory [44, 45], which is developed based on the original Euler-Bernoulli beam theory and extends to include geometrical nonlinearities by solving the beam kinematics in the presence of finite rotations. The 3-D structural dynamics are described as the dynamics of a reference line in the beam model, in which the full 3-D degrees-of-freedom are reduced into a smaller number of variables (e.g. sectional stress and strains) with equivalent cross-sectional properties. The process to obtain such cross-sectional

properties, called homogenisation, were discussed in [46, 47]. As a result of the reduction in fidelity, the geometrically-nonlinear beam and shell theories require less computational costs. It should be emphasized that despite being geometrically nonlinear, the beam and shell theories are developed under the assumption of linear elasticity, which means that although the displacement and rotation due to structural deformation can be large, the internal strains remain small and are within the range of linear material behaviour. Please refer to [45, 48] for a detailed review on the geometrically-nonlinear composite beam theory.

The geometrically-nonlinear beam equations to model the structural dynamics of VFA associated with large deformations have been formulated by using different variables to describe the displacement field and the beam reference line's rotation. A common approach is the displacement-based formulation. Simpson et al. [49] formulated the beam equations using nodal displacement described in the body-fixed frame and nodal orientation in the form of Cartesian rotation vector described in each node's local frame, as primary state variables, based on which the flexible-body equations of motion were derived using Hamilton's principle. The displacement-based formulation was also used in the works of [22, 50, 51] for the structural modelling of VFA. This type of formulation facilitates the advantage of the nodal displacement and rotation information being directly available, however, the order of the description of geometrical nonlinearities is high, which results in complexity of the formulation and moderate computational cost.

In contrast, the strain-based formulation is developed to provide a computationally effective approach. The beam's internal strains are used as primary state variables to describe the beam deformation. Example works can be found in [52–54]. In the strain-based formulation, the internal forces and moments can be easily derived from strain variables, without requiring differentiation operations as in the displacement-based formulation. The strain-based formulation features a constant stiffness matrix that does not need update, which can reduce the computation cost to derive the solution. The displacement and rotation variables can be retrieved via an additional post-processing step. An alternative approach to effectively solve the geometrically nonlinear beam problems is the mixed-form formulation [55, 56], in which the internal velocities, strains and rotations are used as primary state variables. Such formulation requires a larger number of state variables but leads to more simplified equations.

Another type of formulation is the intrinsic formulation. Hodges [44] developed a two-field intrinsic formulation using the internal velocities and stresses, and demonstrated the unique advantage of formulating the geometrical nonlinearities

ties by second-order terms in the equation. Palacios et al. [20] provided detailed a comparison between the above different types of formulation in terms of numerical efficiency and simplicity of integration, which concluded that the intrinsic formulation and strain-based formulation are more computationally effective. Wang et al. [19, 27] developed an intrinsic modal framework to describe the geometrically-nonlinear structural dynamics. The framework is developed initially based on the intrinsic formulation using the sectional inertial linear and angular velocities, and the resultant sectional forces and moments as primary state variables. The intrinsic degrees of freedom are then projected onto a set of linear structural normal modes and the quadratic nonlinearity terms are retained. The formulation can be easily reduced to obtain a reduced-order description to benefit the control synthesis.

On the other hand, the aerodynamics modelling of VFA has been subject to much research. The aerodynamic model calculates the aerodynamic forces and moments applied on the aircraft. Very high-fidelity aerodynamics modelling approaches using computational fluid dynamics (CFD) techniques have been investigated in numerous works [57–59]. The major issue of using CFD methods lies in the expensive computational cost required for the dynamic simulations for VFA which operate at relatively low Reynolds number. In addition, when large wing deformations happen, re-meshing of the aerodynamic surfaces to adapt the fluid domain discretization are also very expensive operations. Despite the advances in computing power and available acceleration algorithms, CFD is still impractical for full-vehicle dynamic simulations for VFA. Hence, research on the aerodynamic modelling of VFA has instead focused on developing aerodynamic models with reduced fidelities.

The potential flow methods are very good candidates in this capacity and have been studied extensively for low-speed aerodynamics modelling [60]. The governing equations of potential flow methods can be formulated as a boundary-value problem and solved by finding a superposition of singularities that satisfies the boundary condition, instead of solving the entire field through discretization of the entire volume. In this manner, the computational cost can be largely reduced compared to CFD methods. As a standard formulation of the potential flow methods, the doublet lattice method (DLM) which uses doublet panels gives a frequency-domain formulation with the assumption of flat wake, and is commonly used in the aircraft industry. However, it is known that DLM is difficult to model the in-plane motions of the aerodynamic surfaces. In contrast, the vortex lattice method (VLM) which uses vortex panels is able to solve this problem. A very popular extension to VLM is the unsteady VLM (UVLM) and has been used to capture the three-dimensional aerodynamics of VFA in a number of works [20, 51, 61–63]. The UVLM

is described in the time-domain with the assumption of free wake and enables the prediction of wing-tip effects [20], as well as the modelling of the aerodynamic interference between wakes and lifting surfaces [51]. However, in the UVLM formulation, the number of wake panels increases as the simulation time rises, which brings computational burdens for long simulations.

To further reduce the computational cost of panel methods, the 2-D unsteady strip theory has been developed and formulated in both time-domain (Wagner’s function) and frequency-domain (Theodorsen’s function). The unsteady strip theory models the response of each aerofoil section separately and integrates 2-D loads to estimate the 3-D aerodynamics. Palacios et al. compared the 2-D unsteady strip theory with 3-D UVLM in [20] and found that the 3-D models give more accurate predictions for low-aspect-ratio cases with high frequency oscillations while the 2-D models are justifiable to predict the critical behaviours of high-aspect-ratio wings with low frequency oscillations. Compared with potential flow methods, the 2-D aerofoil models have an additional advantage of being easier to apply aerodynamic coefficients of the practical aerofoil. The use of 2-D unsteady strip theory for the aerodynamics modelling of VFA has been investigated in various works such as [8, 19, 21, 39, 42, 64]. It is necessary to mention that the 2-D aerodynamic models cannot capture the lift loss due to the wing tip effects for a finite wing. However, as the aspect-ratio increases, the wing tip effect decreases [60]. Hence, it is acceptable to ignore such effect for the aerodynamics modelling of VFA with high-aspect-ratio configuration [17, 19]. Alternatively, a correction factor can be applied in the wing tip region to compensate the 3-D aerodynamics as did in the works of [6, 20].

Based on the above structural and aerodynamic modelling techniques, a number of simulation frameworks have been developed to investigate the coupled aeroelastic and flight dynamic responses of very flexible aircraft. Patil et al. [8, 17, 56] developed a simulation framework called NATASHA, using the mixed variational beam formulation and 2-D aerodynamics model. The modelling framework was applied to a free-flying high-aspect-ratio wing [56] and a HALE aircraft [8], respectively. An additional stall model was included to account for the stall effects at high angles-of-attack caused by wing deformations. The authors studied the phenomenon of limit-cycle oscillation in the presence of large displacements and rotations, and the impact of airframe flexibility on rigid-body flight dynamics. Subsequently, the authors used this framework on a *Helios*-like very flexible flying wing model and studied its trim, stability and nonlinear flight dynamics [17], which provided a good benchmark for following aeroelastic studies.

Cesnik et al. developed an integrated modelling framework using the strain-

based beam formulation and 2-D aerodynamics model, called UM/NAST, which has been applied to a range of VFA configurations [16, 65–69]. Shearer and Cesnik [65] focused on the analysis of the flight dynamics of a twin-tailed HALE aircraft with conventional wing/body/tail configuration. The strain-based geometrically nonlinear beam formulation and the unsteady aerodynamic model are integrated using an implicit modified Newmark method. Through simulations conducted on the nonlinear rigid-body case, nonlinear rigid-body coupled with linear structural model and nonlinear rigid-body coupled with nonlinear structural model, respectively, this work demonstrated the importance of incorporating nonlinear structural solutions for the dynamics analysis of VFA. In a subsequent work [66], the authors investigated the trajectory control of the same HALE aircraft, and the control design was facilitated by the modelling framework to allow for a low-order nonlinear formulation. Su and Cesnik employed this modelling framework to study the coupled nonlinear flight dynamics and aeroelastic responses of a very flexible blended-wing-body aircraft [67] and a very flexible flying wing [16], respectively. Discrete gust models were integrated into the framework to study the gust responses. In [16], the authors also analysed the flight dynamic stability of the very flexible flying wing at trimmed conditions subject to different payloads. Numerical simulations showed that the phugoid mode became unstable soon after the payload reached to 50% full-payload. Dillsaver et al. [69] studied the impact of structural stiffness on the gust response of VFA based on the same very flexible flying wing model in [16, 17]. Simulations were conducted on thirteen aircraft configurations with different stiffness parameters subject to spatially and temporally distributed gusts. The simulation results revealed the change of the maximum pitch angle excursion/root curvature with respect to bending/torsional stiffness. Dillsaver et al. [68] also studied the gust load alleviation control of a small-scale very flexible aircraft, called X-HALE (see Fig. 1.4), formulated by UM/NAST modelling framework. This was subsequently followed by an experimental project [70] to validate the UM/NAST modelling framework against experimental data. The preliminary results in [71] showed that the designed prototype aircraft did exhibit obvious aeroelastic behaviours with large wing-tip displacement. However, the experiment data collected from initial flight tests were yet to support validation of the framework, due to a limited sensor payload and poor quality of data.

Palacios et al. [22, 49, 50, 72] developed the SHARPy modelling framework based on the displacement-based beam formulation and 3-D UVLM aerodynamic model. The SHARPy modelling framework is coded in Python and has been used to study the nonlinear trim, stability and flight dynamics of VFA. Through lin-



Figure 1.4: The XHALE very flexible aircraft.

earisation of the aeroelastic and flight dynamic equations of motion around a trim equilibrium, the framework can provide linearised state-space models suitable for model reduction and control synthesis. The implementation of UVLM aerodynamic model facilitates the framework with capability to model wake-tail interactions and wake roll-up effects. The SHARPy framework can also be employed to study the aeroelastic dynamics for large wind turbines [73]. Wang et al. [18] developed the NANSI modelling framework also using 3-D UVLM aerodynamic model but intrinsic beam formulation in the structural modelling. A stall model was integrated in the framework to account for stall effects. The modelling framework has been verified against the very flexible flying wing model developed in [17].

Wang et al. [19, 37, 74] developed a nonlinear modal framework based on the intrinsic beam formulation coupled with 2-D unsteady aerodynamics. The intrinsic beam equations are projected onto a set of modal basis and use the structural normal modes as primary state variables. The developed framework can well capture the nonlinear aeroelastic dynamics of VFA and formulate the geometrical nonlinearities in the form of second-order terms. It can also provide a more simplified way to perform model reduction and identify the contributions of each structural mode. The modelling framework has been verified against the Goland cantilever wing model

in [38] and the very flexible flying wing model in [17], and will be used as a basis for the control synthesis and numerical studies in this work.

1.2.2 Aeroelastic control

Since very flexible aircraft (VFA) are very sensitive to external atmospheric disturbance, active aeroelastic control is typically required for disturbance rejection or gust load alleviation [68, 75–79], which constitutes a crucial control loop for VFA. Before we dive into the details of aeroelastic control design, it is worth noting that the structural and aerodynamic models mentioned above are generally developed with a large number of states, rendering high orders of the nonlinear systems. For the purpose of control design, model order reduction is usually applied on the full nonlinear system to obtain a reduced-order representation that is suitable for control synthesis but preserves the dynamics of interest. A widely-used reduction technique on linear aeroelastic systems is the balanced model reduction method [80–82]. The method retains the modes with most significant contributions to the system’s input-output behaviour (measured by the Hankel singular values), eventually leading to a reduced-order description with manageable size but very similar input-output behaviour to the original system. By contrast, nonlinear model reduction is more problem-dependent [19, 22, 42, 83]. In addition to using general model reduction techniques, methods taking advantage of the particular form of the nonlinearities are utilized to facilitate this process. For example, in [19], the use of linear structural normal modes as primary state variables enables the geometrical nonlinearities being formulated in quadratic terms and facilitates a direct and easier model reduction.

Linear control methods have been widely used for the aeroelastic control of VFA. Among them, the robust H_∞ control is very attractive due to its capability to guarantee the control system’s robustness with respect to modelling uncertainties. Silvestre and Paglione [84] employed H_∞ control to design the control augmentation system for a flexible aircraft based on the approximated rigid-body motion, taking elastic deformations as disturbance. Cook et al. [79] investigated the gust load alleviation (GLA) and stabilization of a HALE aircraft which has a design of conventional wing-body-tail configuration and low structural stiffness in the wings. The robust H_∞ controller was designed based on a linearised reduced-order model of 169 states. Simulation studies showed that the controller was able to reduce the root bending moment under different gust excitations. Wang et al. [19] designed the GLA control system for the very flexible flying wing model [17] using H_∞ control. Due to the advantage of the modal intrinsic modelling framework, a 20-state linearised reduced-order model was derived to benefit the control synthesis. Similarly, the

closed-loop responses under different gust excitations were studied to demonstrate the performance of the H_∞ control system.

Besides, H_2 control methods have been used in the literature. Aouf et al. [85] designed H_2 and H_∞ controllers to regulate the body acceleration for a simple flexible aircraft model, which was augmented from a linear rigid aircraft model and five most influential flexible modes, without considering unsteady aerodynamics. Simulation results showed that the H_∞ controller outperformed the H_2 controller in reducing the body accelerations through wind gust. Alazard [86] designed a lateral controller using H_2 control for a flexible carrier aircraft, the model used in this work was a linearised one around an equilibrium point. For the applications of H_2 control methods on very flexible aircraft model which considers geometrically nonlinearities and unsteady aerodynamics, Dillsaver et al. [68] designed a LQG controller to reduce the effect of wind gust for the X-HALE aircraft model developed in [70], with an integrator added to enable pitch angle tracking. Only longitudinal dynamics were considered in this work, assuming symmetric wind gust. The LQG controller was shown to achieve good gust load alleviation performance in minimizing the wing curvature. The authors [69] further investigated the GLA for the very flexible flying wing model developed in [17] using the same LQG controller. The controller's performance was examined via simulations on thirteen aircraft configurations with different structural stiffness parameters subject to spatially and temporally distributed gusts. However, from the perspective of control theory, it is known that LQG is essentially lack of robustness to system uncertainties. Thus, the loop transfer recovery (LTR) technique is developed and combined with LQG to ensure guaranteed stability margin of the closed-loop system, leading to the LQG/LTR approach. Gibson et al. [87] designed a linear LQG/LTR controller and an adaptive LQG/LTR controller to stabilize the VFA at large dihedral excursions, respectively. Simulation results demonstrated that the adaptive LQG/LTR controller achieved better control performance over the linear one.

Apart from the above linear approaches, nonlinear control methods have also been applied for the aeroelastic control of VFA. The model predictive control (MPC) is mostly used in the literature. The essence of MPC is to online update the control inputs by solving an optimization problem over a finite horizon at each time step and allows to take account of nonlinear effects in the internal model [88, 89]. Haghighat et al. [90] employed MPC to achieve dynamic stabilization and gust load alleviation for a very flexible aircraft. An additional prediction enhancement feedback loop was added in this work to improve future state predictions, thereby improving the performance and robustness of the conventional MPC formulation. The designed MPC

controller showed better control performance than a linear quadratic controller at regulating the maximum stress and rigid-body variables. Similar conclusions can be drawn from the work of Simpson et al. [91], which investigated the gust load alleviation control subject to input constraints for a cantilever wing model. Wang et al. [27] applied MPC control to suppress wing oscillations of the very flexible flying wing model in response to wind gusts. By taking advantage of quadratic nonlinear couplings, a computationally-efficient MPC controller was designed based on rapid online re-linearisation of the nonlinear reduced-order model. The control design assumes full-state feedback and no control saturation constraints were applied. Simulation results demonstrated that significant improvements in stability boundary of the nonlinear MPC controller against wind disturbances were achieved. Moreover, Giessler et al. [92] and Liu et al. [93] investigated the gust load alleviation for a flexible aircraft using MPC control and light detection and ranging (Lidar) technique. Wind measurement of the incoming gust disturbance by Lidar was used by the MPC controller to improve disturbance rejection performance. In addition, adaptive control methods have been studied for gust load alleviation of VFA in [94, 95], but the control systems were all designed based on linear aircraft models.

1.3 Motivations and Research Contributions

From the previous section, we can see that most studies in this problem area have been focused on the aeroelastic modelling and aeroelastic control of very flexible aircraft (VFA). A few modelling frameworks have been developed to formulate the dominant nonlinear aeroelastic dynamics of VFA and provide the foundation for flight control synthesis and numerical simulations. However, the flight control of VFA should not only achieve a desirable aeroelastic response (aeroelastic control) but is able to drive the aircraft to effectively follow desired flight paths (trajectory control). Currently, there has been limited research on the aspect of trajectory control. Hence, it is of great necessity to investigate the combined aeroelastic and trajectory control of VFA, especially in the presence of wind disturbance. The contribution of this work is threefold:

- (1) We investigate the aeroelastic and trajectory control for VFA in the presence of wind disturbance, using robust control methods and parameter optimization scheme to enhance robustness and effectiveness. The very flexible flying wing model formulated by the modal modelling framework developed in [19] is used as numerical test case. As introduced earlier, the modal modelling framework is developed based

on geometrically nonlinear beam theory using intrinsic degrees of freedom coupled with 2-D unsteady aerodynamics. The structural, aerodynamic and flight dynamic models are projected onto a set of structural normal modes, which largely facilitates the process of model reduction to obtain a reduced-order model suitable for control synthesis and the identification of modal contributions. Since VFA exhibit highly complex dynamics and are very sensitive to wind disturbance, it is crucial to design a flight control system with sufficient robustness against modelling uncertainties/unmodelled dynamics and disturbance rejection. For this purpose, we propose a two-loop PI/LADRC (linear active disturbance rejection control) and H_∞ robust control scheme to achieve the combined aeroelastic and trajectory control. We employ the particle swarm optimization (PSO) algorithm for parameter optimization in the H_∞ control design to enhance robustness and effectiveness. The performance of the designed aeroelastic and trajectory control system is tested by simulations conducted on the nonlinear aeroservoelastic model of the flying wing under wind gust and turbulence excitations. Simulations results demonstrate that good performance of the control system with respect to trajectory tracking and disturbance rejection are achieved.

(2) Furthermore, we investigate the autonomous landing control for VFA using Lidar (light detection and ranging) preview to improve control performance and ensure safe landing in the presence of wind turbulence. As a critical flight phase, landing determines whether an aircraft can be safely recovered. Current research on landing control is mostly devoted to rigid-body aircraft and has rarely touched flexible ones. Moreover, as mentioned earlier, the HALE UAV *Aquila* was substantially damaged in a crash due to wind gusts during landing [15], which implies that the autonomous landing control remains one of the current bottlenecks in large UAV development. We propose to design a preview-based autonomous landing control system for the same very flexible flying wing model as in (1) using H_∞ preview method with short-range Lidar wind measurement. The Lidar system is used to measure the velocity of the approaching wind disturbance at a distance in front of the aircraft. These wind measurements are provided to the landing control system as preview knowledge, which enables the control system to act before the wind disturbance actually affect the aircraft. In this manner, the preview-based landing control system achieves improved control performance and can largely benefit the autonomous landing scenario for VFA. The landing control system follows the same two-loop structure for the aeroelastic and trajectory control system as in (1) but extends the inner-loop H_∞ controller to incorporate Lidar preview wind measurements. Simulation tests are again conducted on the nonlinear aeroservoelastic

model, which show that the preview-based landing control system is able to land the aircraft safely and effectively, and also achieves better effectiveness and disturbance rejection performance than a baseline landing control system (without preview).

(3) At last, we investigate the aeroelastic and trajectory control for VFA using data-driven control methods to reduce the dependence of control design on system modelling. By far, almost all the flight control systems for VFA, including the control designs discussed above, are using various types of conventional linear or nonlinear model-based control methods. The conventional model-based control design is typically based on a mathematical model with the faith that it represents the practical system. However, it is well-known that the issues of modelling uncertainties and unmodelled dynamics are inevitable in the modelling process, and the situation is more severe for VFA due to their complex system dynamics. Moreover, the mathematical model of VFA usually contains a large number of states and is unsuitable for direct control synthesis, thus, model order reduction is required which further introduces modelling uncertainties. The performance and reliability of the control system designed based on such inaccurate model may lead to degraded performance or even unstable closed-loop response. Hence, it is of great significance to design a flight control system which can overcome the above issues of conventional model-based control methods. We propose to design a data-driven flight control system for the same very flexible flying wing model as in (1) using the data-driven Model-Free Adaptive Control (MFAC) scheme to reduce the dependence of control design on explicit system modelling. A cascaded proportional-derivative MFAC (PD-MFAC) scheme is proposed to accommodate the MFAC scheme in a flight control problem, based on which the data-driven control system is designed to achieve gust load alleviation and trajectory tracking. By running simulations on the nonlinear aeroservoelastic model, we compare the performance of the developed data-driven flight control system with a baseline H_∞ flight control system. The simulation results demonstrate that the data-driven control system is able to properly regulate all the rigid-body and flexible modes, and achieves better effectiveness and robustness against disturbance rejection and modelling uncertainties.

1.4 Outline of Thesis

The structure of this thesis is organized as follows: Chapter 2 briefly presents the aeroelastic modelling of a very flexible flying wing using intrinsic description and the nonlinear model reduction to obtain the reduced-order design model. Chapter 3 designs the aeroelastic and trajectory control system for the very flexible flying

wing model employing a two-loop PI/LADRC and H_∞ control scheme. The particle swarm optimization algorithm is employed to enhance control effectiveness and robustness. Chapter 4 investigates the preview-based autonomous landing control of the very flexible flying wing in the presence of wind turbulence. The H_∞ preview control is employed to incorporate Lidar preview wind measurements to improve control performance. Chapter 5 designs the data-driven flight control system using the proposed PD-MFAC approach to reduce the dependence of control design on modelling. Its performance is compared with the model-based control system using H_∞ control. Finally, Chapter 6 concludes this thesis and lists a couple of interesting future research areas.

Chapter 2

Modelling of the very flexible flying wing

In this thesis, we use the very flexible flying wing model developed in [19] to investigate flight control design in the Chapters 3-5. The modelling of the very flexible flying wing presented in this chapter has been investigated in the work of [19]. For ease of reference, we summarize the aeroelastic modelling of the aircraft in [19] and briefly introduce the key results of the aeroelastic formulations and the nonlinear model reduction to obtain a system model of appropriate order for control synthesis. We refer to [19] and the references therein for more details.

2.1 Intrinsic Beam Equations

Consider a very flexible high-aspect-ratio airframe with control surfaces and variable engine thrust. As shown in Fig. 2.1, the airframe is modelled as a collection of geometrically-nonlinear composite beams, of which the equations of motion (EOM) are described using the intrinsic beam theory. On the basis of Hamilton's principle [96], the strong form of the beam equations is derived with additional compatibility relations and constitutive relations as

$$\begin{aligned} \mathbf{M}\dot{\mathbf{x}}_1 - \mathbf{x}'_2 - \mathbf{E}\mathbf{x}_2 + \mathcal{L}_1(\mathbf{x}_1)\mathbf{M}\mathbf{x}_1 + \mathcal{L}_2(\mathbf{x}_2)\mathbf{C}\mathbf{x}_2 &= \mathbf{f}_E, \\ \mathbf{C}\dot{\mathbf{x}}_2 - \mathbf{x}'_1 + \mathbf{E}^\top \mathbf{x}_1 - \mathcal{L}_1^\top(\mathbf{x}_1)\mathbf{C}\mathbf{x}_2 &= \mathbf{0}, \end{aligned} \tag{2.1}$$

where $\dot{\bullet}$ denotes derivative with respect to time while \bullet' denotes derivative with respect to length along the beam. $\mathbf{x}_1 = [\mathbf{v}^\top \ \mathbf{w}^\top]^\top$ and $\mathbf{x}_2 = [\mathbf{f}^\top \ \mathbf{m}^\top]^\top$ are the state variables, with $\mathbf{v} \in \mathbb{R}^3$ and $\mathbf{w} \in \mathbb{R}^3$ being the sectional linear and angular velocities, and $\mathbf{f} \in \mathbb{R}^3$ and $\mathbf{m} \in \mathbb{R}^3$ being the resultant sectional forces and moments,

respectively. These intrinsic variables are all defined in the local (deformed) reference frame at location $l \in [0, L_a]$ along the beam reference axis, where L_a is the total length of the beam structure. \mathbf{M} and \mathbf{C} are the mass matrix and compliance matrix of the material properties, respectively. The variable $\mathbf{f_E}$ denotes the force and moment applied externally, the matrix \mathbf{E} describes the initial beam curvature, and the operators \mathcal{L} are linear transformations defined to operate on vectors in [97].

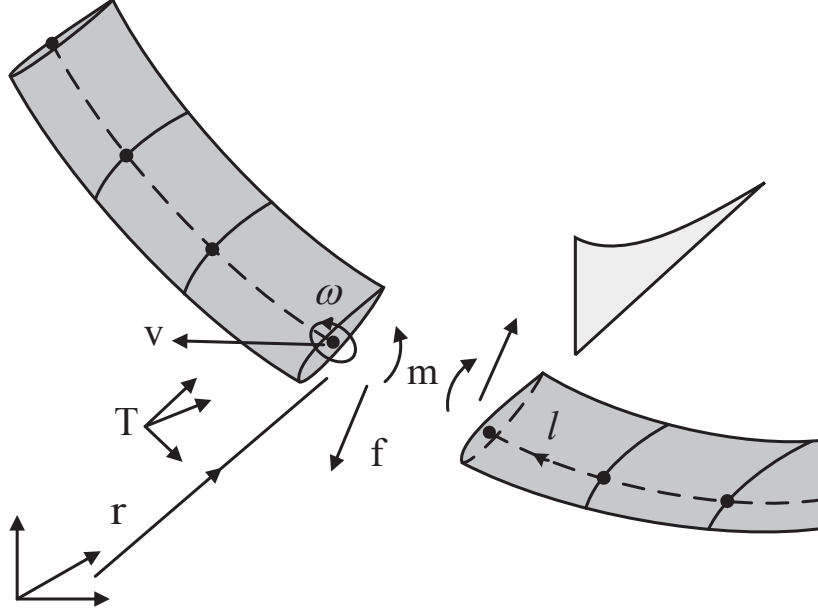


Figure 2.1: Illustration of the very flexible flying wing.

The aerodynamic force and moment $\mathbf{f_E}$ applied on the airframe are formulated using the two-dimensional (2-D) linear unsteady aerofoil theory in the aerodynamic model. The formulation starts from standard inviscid analysis on a flat 2-D aerofoil via the Theodorsen's solution, and then modifies the solution to fit actual parameters of the wing shape. The aerodynamic model is first described in the local aerodynamic reference frame at each point, but subsequently coupled into the intrinsic beam equations (2.1) expressed by the state variables $\mathbf{x_1}$ and $\mathbf{x_2}$ in the local structural reference frame at that point (please refer to **Appendix A** for the explicit formulations of $\mathbf{f_E}$), using the method described by Palacios et al. [98]. The effects of control surfaces are modelled by modifying the local aerodynamic coefficients of the lifting surfaces while the engine thrusts are modelled by point forces. Furthermore, the effect of gravity and external wind gusts are also considered in the flight dynamics model. The displacement $\mathbf{r} \in \mathbb{R}^3$ and rotation matrix $\mathbf{T} \in \mathbb{R}^{3 \times 3}$ at

location l along the beam structure are obtained by integrating the intrinsic velocity variables in time from a initial reference shape and are given by [74]

$$\dot{\mathbf{T}}(l, t) = \mathbf{T}(l, t)\tilde{\boldsymbol{\omega}}(l, t), \quad (2.2a)$$

$$\dot{\mathbf{r}}(l, t) = \mathbf{T}(l, t)\mathbf{v}(l, t), \quad (2.2b)$$

where the $\tilde{\bullet}$ symbol indicates the cross-product operator acting on three-element vectors, such that for vectors $\mathbf{a} \in \mathbb{R}^3$ and $\mathbf{b} \in \mathbb{R}^3$, $\tilde{\mathbf{a}}\mathbf{b} = \mathbf{a} \times \mathbf{b}$.

2.2 Modal Aeroservoelastic Description

This section describes the projection of the beam equations (2.1) onto a set of modal basis to obtain a modal formulation, which converts the nonlinear partial differential equations into ordinary differential equations that can be easily solved in time, and also largely simplifies the process of model order reduction [74]. In the structural model, Galerkin projection [99, 100] is used to express the intrinsic state variables as

$$\begin{aligned} \mathbf{x}_1 &= \sum_j \psi_{1j}(l)q_{1j}(t), \\ \mathbf{x}_2 &= \sum_j \psi_{2j}(l)q_{2j}(t), \end{aligned} \quad (2.3)$$

where the pairs $(\psi_{1j}, \psi_{2j}) : [0, L] \rightarrow \mathbb{R}^6$ are the structural normal modes used as basis functions, \mathbf{q}_1 and \mathbf{q}_2 are the modal amplitudes in the sectional linear/angular velocities and the force/moment resultants, respectively. By subsequently projecting the aerodynamic model and the flight dynamics model onto modal basis, the dynamic equations of the full modal aeroservoelastic system are

$$\begin{aligned} \dot{\mathbf{q}}_s &= \mathbf{A}_s \mathbf{q}_s + \mathbf{\Gamma}(\mathbf{q}_s) \mathbf{q}_s \\ &\quad + (\mathbf{H}_1(\mathbf{q}_s^*) + V_\infty \mathbf{H}_2(\mathbf{q}_a) + \mathbf{H}_{3,d}(\mathbf{q}_s^*) \delta_d) \mathbf{q}_s^* \\ &\quad + \mathbf{H}_g(\mathbf{q}_s) \mathbf{T}_0 + \mathbf{H}_T \mathbf{f}_T, \end{aligned} \quad (2.4a)$$

$$\dot{\mathbf{q}}_a = \mathbf{P}_1 \mathbf{q}_s^* - V_\infty \mathbf{P}_2 \mathbf{q}_a, \quad (2.4b)$$

$$\dot{\mathbf{T}}_0 = \mathbf{T}_0 \mathbf{N}_1(\mathbf{q}_s), \quad (2.4c)$$

$$\dot{\mathbf{r}}_0 = \mathbf{T}_0 \mathbf{N}_2(\mathbf{q}_s), \quad (2.4d)$$

where the full set of primary states consist of the structural states $\mathbf{q}_s = [\mathbf{q}_1, \mathbf{q}_2]^T$, the aerodynamic states \mathbf{q}_a , and the orientation \mathbf{T}_0 and displacement vector \mathbf{r}_0 of a chosen reference point along the beam in the inertial frame of reference. The orientation \mathbf{T}_0 and displacement \mathbf{r}_0 are derived from (2.2) and tracked as additional states to provide rigid-body displacement and rotation information.

In equation (2.4a), the structural dynamic response is described by the matrix \mathbf{A}_s and operator $\mathbf{\Gamma}$, corresponding to the linear and geometrically nonlinear terms, respectively. Linear operators \mathbf{H}_1 and \mathbf{H}_2 describe the influence of the instantaneous and time-dependent (lift history) aerodynamic forces on the structure respectively. The influence of aerodynamic forces caused by control surfaces is described by \mathbf{H}_3 with δ_d being the vector of control surface deflection angles. While the effect of thrust is described by \mathbf{H}_T with \mathbf{f}_T being the vector of engine thrust settings. \mathbf{H}_g describes the effect of gravity. Equation (2.4b) describes the lift history associated with each structural mode from a rational-function approximation to Theodorsen's theory. The aerodynamic states \mathbf{q}_a are introduced to track the unsteady lift history projected onto the modal basis and V_∞ is computed as the magnitude of the current free stream velocity at the reference point. Equations (2.4c) and (2.4d) describe the time-integration of the rotation matrix and displacement vector in modal forms by linear operators \mathbf{N}_1 and \mathbf{N}_2 . Since the aerodynamic model assumes the aerofoil moves through still air, the influence of external gust (defined as a spatial distribution of gust velocities in the global frame) are modelled as causing an additional downwash as local gust velocity, and thus can be translated into the model by modifying the velocity states used in the aerodynamic force computations as

$$\mathbf{q}_s^* = \mathbf{q}_s + \mathbf{q}_{sg}, \quad (2.5)$$

where \mathbf{q}_{sg} is the gust velocity distribution (a function of \mathbf{r} and \mathbf{T}) projected onto the velocity modal basis [19]. Note that the aeroservoelastic system (2.4) will be used as a basis for the numerical simulation of the dynamic responses of the very flexible flying wing.

2.3 Model Order Reduction

Even with a description on modal basis, the above aeroservoelastic formulation (2.4) requires a large number of states (of order 10^3) for convergence in time-domain simulations [19]. To obtain a model of appropriate size for the purpose of control design, the full-order description (2.4) is first linearised around a trim equilibrium and then reduced by applying balanced truncation methods. The trim equilibrium

is defined as the solution to (2.4) such that

$$\dot{\mathbf{q}}_s = \mathbf{0}, \quad \dot{\mathbf{q}}_a = \mathbf{0}, \quad \dot{\mathbf{T}}_0 = \mathbf{0}, \quad \dot{\mathbf{r}}_0|_{1,3} = 0, \quad (2.6)$$

given a specific operating point which in our case is determined by the expected airspeed and altitude. The equation (2.6) in fact defines a steady forward level flight, assuming y-axis as the direction of flight. The corresponding trim equilibrium states are denoted as \mathbf{q}_{se} , \mathbf{q}_{ae} , \mathbf{T}_{0e} and \mathbf{r}_{0e} , respectively. The orientation of the reference node \mathbf{T}_0 is then expressed by its relative rotation from the trim equilibrium orientation \mathbf{T}_{0e} in terms of Euler angles (ψ_z, ψ_y, ψ_x) as $\mathbf{T}_0 = \mathbf{T}_r(\psi_z, \psi_y, \psi_x)\mathbf{T}_{0e}$ with $\mathbf{T}_r = \mathbf{I}$ at trim.

For model order reduction, the system will be expanded around this trim equilibrium where we now define the new states $\mathbf{q}_n = [(\mathbf{q}_s - \mathbf{q}_{se})^\top, (\mathbf{q}_a - \mathbf{q}_{ae})^\top, \psi_y, \psi_x]^\top$ and the control input vector $\mathbf{u}_c = [\Delta\delta^\top, \Delta\mathbf{f}_T^\top]^\top$ which is the collection of flap deflection and thrust actions relative to trim. Expanding the aeroelastic system with respect to new state variables \mathbf{q}_n and \mathbf{u}_c around the trim equilibrium and retaining quadratic terms give rise to

$$\dot{\mathbf{q}}_n = (\mathbf{S}_A + \mathbf{Q}(\mathbf{q}_n))\mathbf{q}_n + \mathbf{S}_{B1}\mathbf{w}_d + \mathbf{S}_{B2}\mathbf{u}_c, \quad (2.7)$$

where \mathbf{S}_A is the linearised state dynamics, $\mathbf{Q}(\mathbf{q}_n)$ describes the quadratic nonlinearities, \mathbf{S}_{B1} and \mathbf{S}_{B2} denote the influence of gust strength \mathbf{w}_d and control actions \mathbf{u}_c , respectively. Additionally, sensor measurements can be defined as a linear combination of the state variables based on (2.3), which results in the measurement matrix \mathbf{S}_C and the output vector \mathbf{y} and

$$\mathbf{y} = \mathbf{S}_C\mathbf{q}_n. \quad (2.8)$$

Equations (2.7) and (2.8) together form the state space model of the aeroelastic system (2.4) with quadratic nonlinearities. If we rewrite $\mathbf{S}_B = [\mathbf{S}_{B1} \quad \mathbf{S}_{B2}]$ and $\mathbf{u} = [\mathbf{w}_d^\top \quad \mathbf{u}_c^\top]^\top$, we obtain

$$\begin{pmatrix} \dot{\mathbf{q}}_n \\ \mathbf{y} \end{pmatrix} = \begin{pmatrix} \mathbf{S}_A + \mathbf{Q}(\mathbf{q}_n) & \mathbf{S}_B \\ \mathbf{S}_C & \mathbf{0} \end{pmatrix} \begin{pmatrix} \mathbf{q}_n \\ \mathbf{u} \end{pmatrix}. \quad (2.9)$$

The state space system (2.9) is then reduced by applying balanced truncation [80,81] to retain the modes with the greatest contribution, based on the linear part of the system (the part without $\mathbf{Q}(\mathbf{q}_n)$). The resulting similarity transformation is

written as $\mathbf{x} = \mathbf{R}\mathbf{q}_n$, where $\mathbf{x} \in \mathbb{R}^{N_r}$ is the reduced state vector, with $\mathbf{q}_n \in \mathbb{R}^{N_q}$ and $N_r \ll N_q$. The projection matrix \mathbf{R} is obtained from balanced truncation, with an associated pseudo-inverse transformation \mathbf{R}^\dagger defined from the reduction such that $\mathbf{R}\mathbf{R}^\dagger = \mathbf{I}$ holds. This results in the reduced-order nonlinear system

$$\begin{aligned} \begin{pmatrix} \dot{\mathbf{x}} \\ \mathbf{y} \end{pmatrix} &= \begin{pmatrix} \mathbf{R}\mathbf{S}_A\mathbf{R}^\dagger + \mathbf{R}\mathbf{Q}(\mathbf{R}^\dagger\mathbf{x})\mathbf{R}^\dagger\mathbf{x} & \mathbf{R}\mathbf{S}_B \\ \mathbf{S}_C\mathbf{R}^\dagger & \mathbf{0} \end{pmatrix} \begin{pmatrix} \mathbf{x} \\ \mathbf{u} \end{pmatrix} \\ &= \begin{pmatrix} \mathbf{A} + \mathbf{Q}_r(\mathbf{x})\mathbf{x} & \mathbf{B} \\ \mathbf{C} & \mathbf{0} \end{pmatrix} \begin{pmatrix} \mathbf{x} \\ \mathbf{u} \end{pmatrix}, \end{aligned} \quad (2.10)$$

where $\mathbf{B} = [\mathbf{B}_w \ \mathbf{B}_u]$ conforms with the definition of \mathbf{S}_B . Setting the \mathbf{Q}_r terms to be zero results in the reduced-order linear system

$$\begin{pmatrix} \dot{\mathbf{x}} \\ \mathbf{y} \end{pmatrix} = \begin{pmatrix} \mathbf{A} & \mathbf{B} \\ \mathbf{C} & \mathbf{0} \end{pmatrix} \begin{pmatrix} \mathbf{x} \\ \mathbf{u} \end{pmatrix}. \quad (2.11)$$

which will be used as the basis for control synthesis in Chapter 3.

For a timestep Δt , the discrete-time equivalence of the reduced-order system (2.11) can be approximated as

$$\begin{aligned} \begin{pmatrix} \mathbf{x}(k+1) \\ \mathbf{y}(k) \end{pmatrix} &= \begin{pmatrix} e^{\mathbf{A}\Delta t} & \mathbf{A}^{-1}(e^{\mathbf{A}\Delta t} - \mathbf{I})\mathbf{B} \\ \mathbf{C} & \mathbf{0} \end{pmatrix} \begin{pmatrix} \mathbf{x}(k) \\ \mathbf{u}(k) \end{pmatrix} \\ &= \begin{pmatrix} \mathbf{A}_f & \mathbf{B}_f \\ \mathbf{C}_f & \mathbf{0} \end{pmatrix} \begin{pmatrix} \mathbf{x}(k) \\ \mathbf{u}(k) \end{pmatrix}, \end{aligned} \quad (2.12)$$

where $\mathbf{B}_f = [\mathbf{B}_{fw} \ \mathbf{B}_{fu}]$ conforms with the definition of \mathbf{B} . The discrete-time reduced-order description (2.12) will be used as the basis for control synthesis in Chapter 4.

2.4 Test Case

For the remainder of this thesis, we consider the 72m-span highly flexible flying wing model used in [16–19] as the numerical test case, of which the geometric configuration is depicted in Fig. 2.2 and the main properties can be found in [17]. The airframe has a flat, straight midsection and an outer-section with 10° dihedral. Three vertical fins are placed below the midsection with a varying payload between 0kg (0%) and 227kg (100%) at the central pod. Five propellers are mounted forward of the wing

providing thrust while flaps are mounted in the trailing edge of the wing. The rigid-body dynamics are approximated at the centre of the wing to control the rigid-body degrees of freedom. These information can be measured through the GPS and IMU sensors installed at the centre node. The root bending moment is utilized as feedback to control the first symmetric bending degree of freedom, which plays a significant role in shaping the elastic mode. We assume the root bending moment is directly available (from the model), without considering the optimisation of sensor types or locations to obtain such information. The measurement outputs are summarized in Table 2.1. A fairly conventional set of flap and thrust control actions are defined (see Fig. 2.2) to control the rigid-body degrees of freedom and the structural bending degrees of freedom, following the definition in [19]. We mention that the selection of these control inputs and sensor measurement outputs satisfies the controllability and observability requirements. The level flight trim condition is at sea level with the speed of $V_{trim} = 12.2m/s$, and the corresponding control input settings are $\delta_{1trim} = -0.19^\circ$, $T_{1trim} = 37N$ (all others are zero).

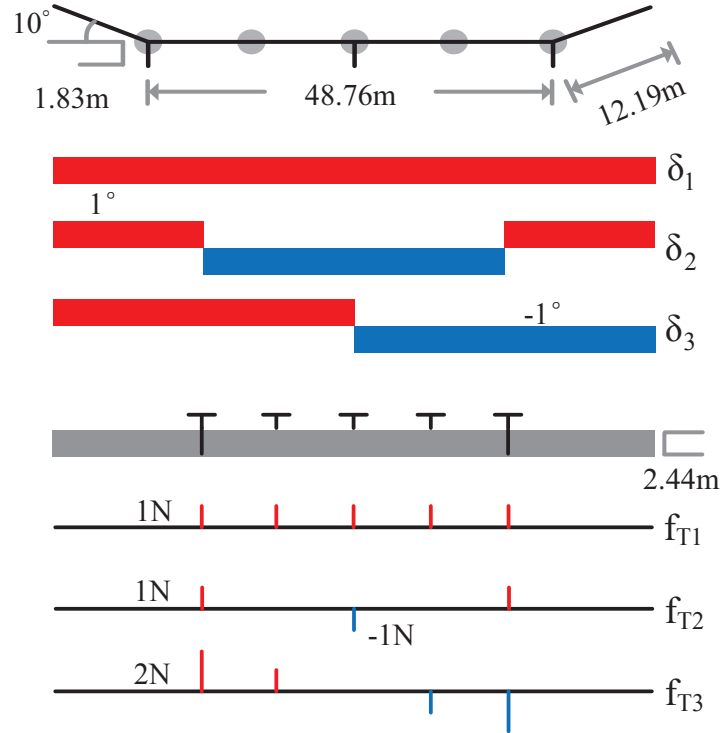


Figure 2.2: Geometric configuration and control surfaces on the aircraft: simultaneous flaps (δ_1), symmetric (δ_2) and antisymmetric (δ_3) differential flaps, simultaneous thrust (f_{T1}), and symmetric (f_{T2}) and antisymmetric (f_{T3}) differential thrust.

Table 2.1: Definition of measurement outputs

No.	Definition	Symbol
1	root bending moment	bm
2	longitudinal velocity	v_2
3	normal velocity	v_3
4	pitch rate	w_1
5	pitch angle	θ
6	twist moment	tw
7	lateral velocity	v_1
8	roll rate	w_2
9	yaw rate	w_3
10	roll angle	ϕ

Following the formulations in Section 2.2, the full-order modal aeroservoelastic system (2.4) contains 1962 states, which includes 6 rigid body velocity states, 588 structural velocity and force states, 600 aerodynamic states, and 768 rotation and displacement states (12 states for each of the 64 nodes along the wing span). The natural frequencies of the first several structural modes are summarized in Table 2.2. It is clear that the frequencies of these structural modes are close to that of the rigid-body modes, which indicates the coupled characteristics of the structural dynamics and the rigid-body dynamics of the aircraft. The wind disturbance and control inputs will excite these low-frequency modes and influence the aircraft's 3-dimensional dynamics, which are reflected via Equation (2.4).

Table 2.2: Natural frequencies of the first few structural modes. The number of the first structural mode starts from seven as modes 1~6 are the rigid-body ones.

Mode No.	Mode Type	Frequency (Hz)
7	1st sym. out-of-plane bending	0.187
8	1st asym. out-of-plane bending	0.615
9	1st sym. in-plane bending (Type 1)	0.843
10	1st asym. in-plane bending (Type 1)	0.886
11	2nd sym. out-of-plane bending	0.984
12	1st sym. in-plane bending (Type 2)	1.592
13	2nd asym. out-of-plane bending	1.861
14	3rd sym. out-of-plane bending	2.495
15	1st asym. in-plane bending (Type 2)	2.545

After model order reduction, as minimum as $N_r = 15$ states in the reduced-order nonlinear system (2.10) is found necessary to capture the key nonlinearities of the aeroservoelastic system (2.4). Please refer to [27] for details on the comparison between the obtained full-order and reduced-order systems.

2.5 Conclusions

In this chapter, we briefly introduced the aeroservoelastic modelling of the very flexible flying wing and its reduced-order descriptions. The model was derived from geometrically-nonlinear beam theory using intrinsic degrees of freedom and linear unsteady aerodynamics, which results in a coupled structural dynamics, aerodynamics and flight dynamics description. Nonlinear model reduction were applied on the full-order nonlinear aeroservoelastic system to obtain the corresponding reduced-order nonlinear and linear descriptions for the purpose of control synthesis.

Chapter 3

Aeroelastic and Trajectory Control

This chapter investigates the aeroelastic and trajectory control for the very flexible flying wing model developed in Chapter 2. The aeroelastic control of this very flexible flying wing has been previously studied in [19], we now further enhance its performance in conjunction with the design of trajectory control. The control system is designed based on the reduced-order linear model (2.11), employing a two-loop control scheme in both the longitudinal and lateral channels. In each channel, the outer loop acts as the trajectory control loop to track the desired flight path and generates attitude angle command to the inner loop, while the inner loop tracks this attitude angle command from the outer loop and simultaneously serves as the aeroelastic control loop for dynamic stabilization and disturbance rejection, by generating control inputs to the corresponding control surfaces (flaps and thrust). The particle swarm optimization (PSO) algorithm is employed to optimize the parameters of the inner-loop controllers to enhance control effectiveness and robustness, by taking account of the quadratic nonlinearity information in the reduced-order nonlinear model (2.10). Simulation tests are then conducted on the full-order nonlinear aeroservoelastic model (2.4) to demonstrate the performance of the designed aeroelastic and trajectory control system.

3.1 Introduction

The flight control of very flexible aircraft (VFA) mainly includes two aspects, i.e. the aeroelastic control and the trajectory control. Since the slender airframe is very sensitive to external disturbance, active aeroelastic control is typically required for

gust load alleviation and disturbance rejection. Most research on the flight control of VFA so far focuses on the aeroelastic control, we refer to Section 1.2.2 for a detailed review on this problem area. On the other hand, the trajectory motion of VFA is normally affected by the airframe deformations due to manoeuvre loads. This poses great challenges to the design of a flight control system which can not only achieve a desirable aeroelastic response, but is able to drive the aircraft to track desired flight path (trajectory control), especially in the presence of wind disturbance.

Currently, there has been limited research on trajectory control of VFA. In the few existing works, the trajectory tracking problem is usually addressed by using the time-scale separation principles between a fast inner stabilization loop and a slow outer position control loop. Shearer and Cesnik [66] studied the trajectory control of a very flexible wing-body configuration. They separated the control problem into two loops: a linear quadratic regulator (LQR) controller and a dynamic inversion controller were employed in the lateral and longitudinal channels, respectively, to track the linear and angular velocities in the inner loop; while a nonlinear transformation together with a PID controller were employed in the outer loop to control the flight path angle, roll angle and their corresponding rates to achieve trajectory tracking. Raghavan and Patil [101] employed a multi-step nonlinear dynamic inversion controller coupled with a nonlinear guidance law for path following, based on the reduced-order model of a 72m-span very flexible flying wing configuration. The proposed controller was able to provide acceptable performance after an abrupt change in payload mass. However, these works focused on trajectory tracking in calm wind conditions, without considering gust load alleviation or, more generally, disturbance rejection. To address this, Dillsaver et. al. [102] investigated the trajectory control of a 6m-span very flexible flying wing in gust disturbance using the dynamic inversion and LQR control in the longitudinal inner loop, as in [66]. A higher gain PID controller and a sliding mode controller were also tested respectively in the outer loop. The authors also designed an LQG controller with a constant pre-compensator in the lateral outer loop to track roll/yaw angle commands. Although gust disturbance were taken into account in their simulation tests, the dynamic inversion control relies on accurate modelling of the plant and generally lacks robustness. It is well known that LQG control is also lack of robustness in certain cases.

The contribution of this chapter is to investigate the aeroelastic and trajectory control of very flexible aircraft in the presence of wind disturbance, using robust control methods and parameter optimization scheme to enhance robustness and effectiveness. For numerical investigation, we consider the very flexible flying

wing developed in Chapter 2, in which the nonlinear aeroservoelastic model and its reduced-order nonlinear and linear versions were derived. The aeroelastic and trajectory control system is designed based on the reduced-order linear model (2.11), therefore, it is crucial to guarantee robustness with respect to modelling errors and wind disturbance in the control design. It is well acknowledged that robust control methods are very good candidates to meet these requirements. Hence, we propose a two-loop PI/LADRC (proportional-integral/linear active disturbance rejection control) and H_∞ control scheme in both the longitudinal and lateral channels. In each channel, the outer loop employs a PI/LADRC controller to track the desired flight path and generate attitude command to the inner loop, while the inner loop uses H_∞ control to track the attitude command generated from the outer loop and computes the control inputs to the corresponding control surfaces (flaps and thrust). It is necessary to mention that both H_∞ control and ADRC approach have shown superior robust performance in the aerospace area [103–110]. We employ the particle swarm optimization (PSO) algorithm for parameter optimization of the weighting matrices in the inner-loop H_∞ control design, which takes advantage of the quadratic nonlinearity information in the reduced-order nonlinear model (2.10) to enhance control effectiveness and robustness. The simulation tests conducted on the full-order nonlinear model (2.4) show that the aeroelastic and trajectory control system achieves good performance with respect to trajectory tracking and disturbance rejection.

The structure of this chapter is organized as follows: Section 3.2 develops the two-loop PI/LADRC and H_∞ controllers to achieve aeroelastic and trajectory control for the very flexible flying wing model. Section 3.3 conducts simulation tests to demonstrate the dynamic tracking performance and the disturbance rejection performance of the developed aeroelastic and trajectory control system. Section 3.4 finally concludes this chapter.

3.2 Control System Design

In this section, we design the aeroelastic and trajectory control system for the very flexible flying wing based on its reduced-order linear model (2.11). It is important, however, to note that simulation tests will be based on the full-order nonlinear model (2.4) and will be described in Section 3.3. For control design, the assumption of no coupling between the aircraft’s longitudinal and lateral dynamics is used hereinafter, which leads to a decoupled reduced-order linear model (2.11). Hence, the design of the control system can be divided into two channels, the longitudinal channel and the lateral channel. But note that the nonlinear models (2.4) and (2.10) are able

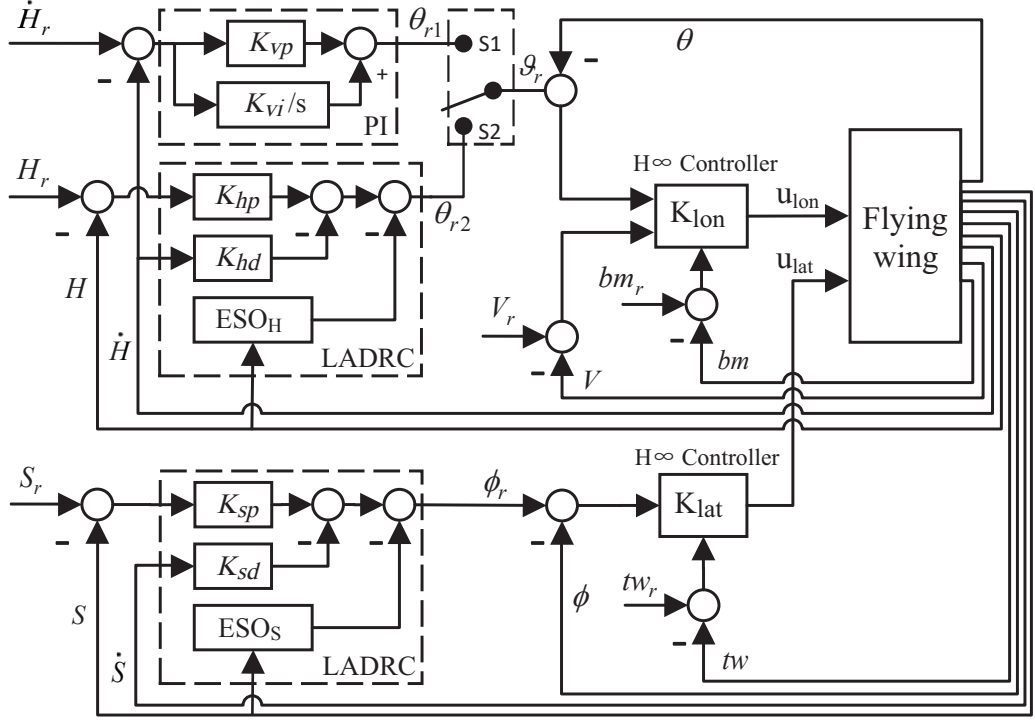


Figure 3.1: Control structure of the aeroelastic and trajectory control system. H , S , θ , V , ϕ , bm and tw denote the altitude, lateral displacement, pitch angle, forward velocity, roll angle, symmetric root bending measurement and anti-symmetric twist measurement respectively. The subscript r denotes the reference command, while $\dot{\bullet}$ denotes time derivative. K_{lon} and K_{lat} are the H_∞ controllers. ESO_H and ESO_S are the extended state observers (ESO) in LADRC. K_{hp} , K_{hd} , K_{sp} , K_{sd} , K_{vp} and K_{vi} are the controller parameters.

to capture the couplings between these two channels. As shown in the control structure in Fig. 3.1, a two-loop control scheme is proposed for each channel, which is explained below. Note that we choose the center of the aircraft as reference point to track the aircraft's flight dynamics, thus all the variables used in this section are defined at this reference point.

Because of the low speeds under consideration, tracking the desired position requires the flying wing to simultaneously maintain the forward velocity. This means that, in the longitudinal channel, both the altitude and forward velocity need to be controlled. This is achieved through pitch control and velocity control, respectively, by adjusting the corresponding longitudinal control flaps and thrust. In this channel, to handle an altitude tracking command, the outer-loop controller is first switched to S1 “climb/descend control” to drive the flying wing to climb/descend. After climbing/descending to a suitable altitude, the outer-loop controller is then switched

to S2 “altitude control” to activate the LADRC controller to precisely position and maintain the flying wing at the desired altitude. The “climb/descend control” generates a pitch angle command for the inner loop, which is regulated through a PI controller using the climb rate as feedback. The LADRC controller is also designed towards the same purpose, but using both the altitude and climb rate as feedback. An inner-loop H_∞ controller is employed to serve as the aeroelastic control loop (with the objective of dynamic stabilisation and gust load alleviation), while simultaneously tracking the pitch angle command from the outer loop and stabilizing velocity, by generating longitudinal control inputs (to the corresponding flaps and thrust) with symmetric root bending measurement, pitch angle and forward velocity as feedback. Note that the usage of root bending measurement as feedback helps to maintain the aircraft at the trimmed shape during manoeuvre. We mention that to reduce the impact of gains during switch in the longitudinal channel, a “soft switch” is employed to switch the reference command smoothly,

$$\vartheta_r = k_S \vartheta_{r1} + (1 - k_S) \vartheta_{r2}$$

$$k_S = \begin{cases} 1 - 0.5t & (t < 2s) \\ 0 & (t \geq 2s) \end{cases} ,$$

where ϑ_{r1} is the pitch angle command generated by “climb/descend control”, ϑ_{r2} is the pitch angle command generated by “altitude control”, ϑ_r is the final pitch angle command to the inner loop.

In the lateral channel, only lateral displacement needs to be controlled, which is achieved through roll control. In this channel, a second outer-loop LADRC controller is used to generate a roll angle command for the inner loop, using the lateral position and the lateral speed as feedback. And an inner-loop H_∞ controller is employed to generate lateral control inputs (to the corresponding flaps and thrust) to track the roll angle command from the outer loop, using the anti-symmetric twist measurement and the roll angle as feedback.

As shown in Fig. 3.1, the reference commands to the control system include the commands of altitude, climb rate, forward velocity, root bending moment, lateral displacement and twist moment. In the vertical plane, the forward velocity command V_r and the root bending moment command bm_r are set to be their trim value, respectively. The altitude command H_r and the climb rate command \dot{H}_r is specified as needed. In the horizontal plane, the twist moment command tw_r is also set to be its trim value while the lateral displacement command S_r is always set to be zero which aims to keep the aircraft aligned with the desired flight path.

3.2.1 Inner-Loop H_∞ Control Design

We first design the inner-loop H_∞ controller in the longitudinal channel. As described above, it serves as an aeroelastic control loop for dynamic stabilisation and gust load alleviation, and also acts to track the pitch angle command received from the outer loop for trajectory tracking. In this manner, the control design is treated as an H_∞ tracking problem.

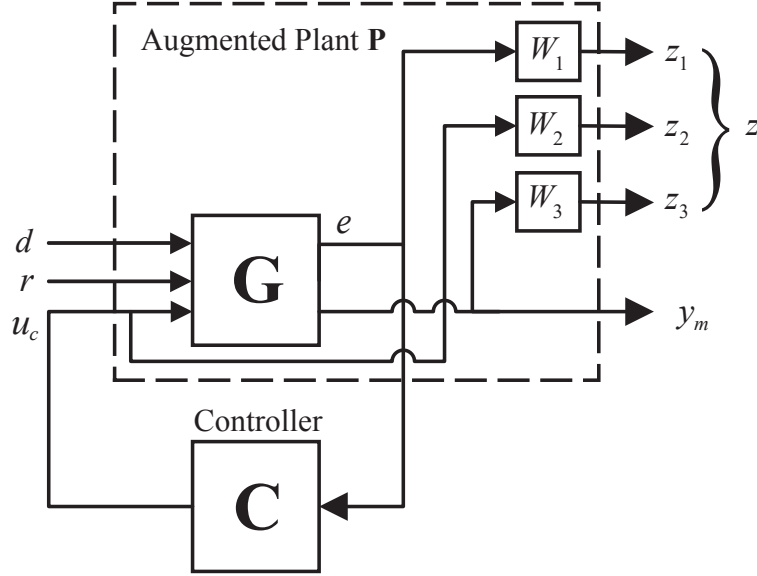


Figure 3.2: Standard H_∞ tracking problem. d , r , u_c , e , z denote the external disturbance, reference command, control input, error signal, and weighted output, respectively. y_m is the measurement output. \mathbf{G} and \mathbf{C} are the transfer functions of the plant and the H_∞ controller.

As shown in Fig. 3.2, the mixed sensitivity H_∞ synthesis method is employed, introducing weighting matrices to achieve both good disturbance rejection performance and tracking effectiveness. The objective is to find an optimal controller \mathbf{C} which minimizes the H_∞ -norm of the transfer function from the disturbance d and reference input r to the weighted performance output z . To pose the H_∞ synthesis problem, considering both reference tracking and disturbance rejection, we augment the original plant \mathbf{G} with weighting matrices W_1 , W_2 and W_3 which is given in the form of

$$W_i(s) = \alpha_{1i} \cdot \frac{\alpha_{2i}s + 1}{\alpha_{3i}s + 1},$$

where s is the Laplace variable and α_{ji} are non-zero scalars. The augmented plant

\mathbf{P} is then expressed in the state-space description

$$\begin{aligned} \dot{x}_{\text{ap}} &= A_{\text{ap}}x_{\text{ap}} + B_{\text{ap}}u_{\text{ap}}, \\ y_{\text{ap}} &= C_{\text{ap}}x_{\text{ap}} + D_{\text{ap}}u_{\text{ap}}. \end{aligned} \quad (3.1)$$

where $y_{\text{ap}} = [z^\top \ y_m^\top]^\top$ and $y_{\text{ap}} = [d^\top \ r^\top \ u_c^\top]^\top$. For simplicity, we rewrite (3.1) in a partitioned structure, which is denoted as

$$\mathbf{P} = \left[\begin{array}{c|c} A_{\text{ap}} & B_{\text{ap}} \\ \hline C_{\text{ap}} & D_{\text{ap}} \end{array} \right].$$

To be specific, we obtain the realization of the augmented plant

$$\mathbf{P} = \left[\begin{array}{cccc|cc} A_1 & 0 & 0 & -B_1C & 0 & B_1 & 0 \\ 0 & A_2 & 0 & 0 & 0 & 0 & B_2 \\ 0 & 0 & A_3 & B_3C & 0 & 0 & 0 \\ 0 & 0 & 0 & A & B_w & 0 & B_u \\ \hline C_1 & 0 & 0 & -D_1C & 0 & D_1 & 0 \\ 0 & C_2 & 0 & 0 & 0 & 0 & D_2 \\ 0 & 0 & C_3 & D_3C & 0 & 0 & 0 \\ \hline 0 & 0 & 0 & -C & 0 & I_r & 0 \end{array} \right],$$

where A , B_w , B_u and C are the linear state space matrices of the flying wing as defined in (2.11), (A_i, B_i, C_i, D_i) are the state space matrices of the weighting matrix $W_{i=1,2,3}$, I_r is an identity matrix with dimension equal to the dimension of the reference command. Normally, W_1 should be selected as low pass filter to achieve good reference tracking performance while W_2 and W_3 should be selected as high pass filter to achieve good robustness [111]. By selecting appropriate weighting parameters (a typical bandwidth range is set to be [0.01-100] rad/s), the command *hinfsyn* in Matlab[®] is used to compute the optimal H_∞ controller in the longitudinal channel, denoted by K_{lon} .

In order to enhance the robust performance and simultaneously achieve good tracking effectiveness, tuning the parameters of the weighting matrices is crucial.

However, in the longitudinal channel of our case, there are 24 parameters to tune, which includes 9 for W_1 (3 parameters for each of the 3 error signals), 6 for W_2 (the same 3 parameters for the two types of flap actions and the other same 3 parameters for the two types of thrust actions defined in Section 2.4) and another 9 for W_3 . Obviously, it is impractical to effectively tune these 24 parameters manually. Therefore, we employ the particle swarm optimization (PSO) algorithm [112, 113] to optimize the parameters of the weighting matrices based on simulations. Given an initial range, the parameters are optimized automatically to seek a minimum of the cost function which is defined to balance the trade-off between robustness and tracking effectiveness of the control system.

We define the cost function of the PSO algorithm as

$$J = \int_0^t k_1 |e(\tau)| d\tau + k_2 \gamma_{H\infty}, \quad (3.2)$$

where $k_{i=1,2}$ is the penalty factor, $e(t)$ is the error between the desired step response (pre-defined) and the actual step response, $\gamma_{H\infty}$ is the H_∞ norm of the controller. The first term is introduced to penalize the tracking error, which aims to ensure both dynamic and static performance of the reference tracking response. The second is introduced to penalize the robustness of the controller. A minimum cost value J_{min} (also called the fitness value) is sought through PSO algorithm, which gives the optimal parameters of the weighting matrices. Note that the iterative simulation-based parameter optimization is based on the reduced-order nonlinear model (2.10) taking advantage of the quadratic nonlinearity information Q_r , which improves the tracking effectiveness and robustness of the inner-loop H^∞ controller. The implementation of the PSO algorithm is briefly summarized as below.

Implementation of the PSO Algorithm

The implementation of the PSO algorithm [114] includes the following steps:

(1) Initialize the number of particles, the maximum number of iterations, the given fitness value ϵ_{ps0} , the learning factors c_{ps01} , c_{ps02} , and the weight factor w_{ps0} . Initialize each particle's position x_{ps0} (i.e. the value of the parameters of the weighting matrices) and velocity v_{ps0} (i.e. the change rate of the parameters during optimization).

(2) Run simulations based on the reduced-order nonlinear model (2.10) to obtain simulation data, using each particle's position value.

(3) Calculate the fitness value J for each particle, if the current fitness value is smaller than its history minimum (called the local minimum), set this value as

the new local minimum which represents the best solution of each particle.

(4) Choose the minimum value (called the global minimum) of all the local minimums in each iteration, if the current value is smaller than the history global minimum, set this value as the new global minimum which represents the best solution of all the particles.

(5) Update the position and velocity values of each particle for the next iteration according to the following equation

$$\begin{aligned}
v_{psoj}(i+1) = & \omega_{pso}(i)v_{psoj}(i) + c_{pso1}r_{pso1}(p_{psoj}^{local}(i) - x_{psoj}(i)) \\
& + c_{pso2}r_{pso2}(p_{psoj}^{global}(i) - x_{psoj}(i)), \\
x_{psoj}(i+1) = & x_{psoj}(i) + v_{psoj}(i+1),
\end{aligned} \tag{3.3}$$

where r_{pso1} and r_{pso2} are random numbers in $(0, 1]$, p_{psoj}^{local} is the position value corresponding to a particle's local minimum and p_{psoj}^{global} is the position value corresponding to the global minimum. i is the iteration number and j is the particle number.

(6) Go to step (2) until the global minimum is smaller than the given fitness value ϵ_{pso} or the maximum number of iterations is reached.

In this manner, by seeking a minimum fitness value J_{min} via the PSO algorithm, we obtain the corresponding optimal parameters of the weighting matrices and derive the longitudinal inner-loop H_∞ controller K_{lon} . Figure 3.3 illustrates an example of the convergence process of the PSO algorithm during optimization, in which the algorithm converges after about 25 iterations.

The design of the inner-loop H_∞ controller K_{lat} in the lateral channel (as shown in Fig. 3.1) is similar to the case in the longitudinal channel, thus it is omitted here.

3.2.2 Outer-Loop LADRC Control Design

As described earlier, the longitudinal outer loop of the control system is comprised of two parts, the PI climb rate controller and the LADRC position controller. The PI controller is simply given in the form of

$$G_{PI}(s) = K_{vp} + \frac{K_{vi}}{s}, \tag{3.4}$$

to achieve climb rate control, where s is the Laplace variable. The gain and integral parameters K_{vp} and K_{vi} can be simply obtained through tuning. The integral term is introduced to eliminate the steady error of the climb rate.

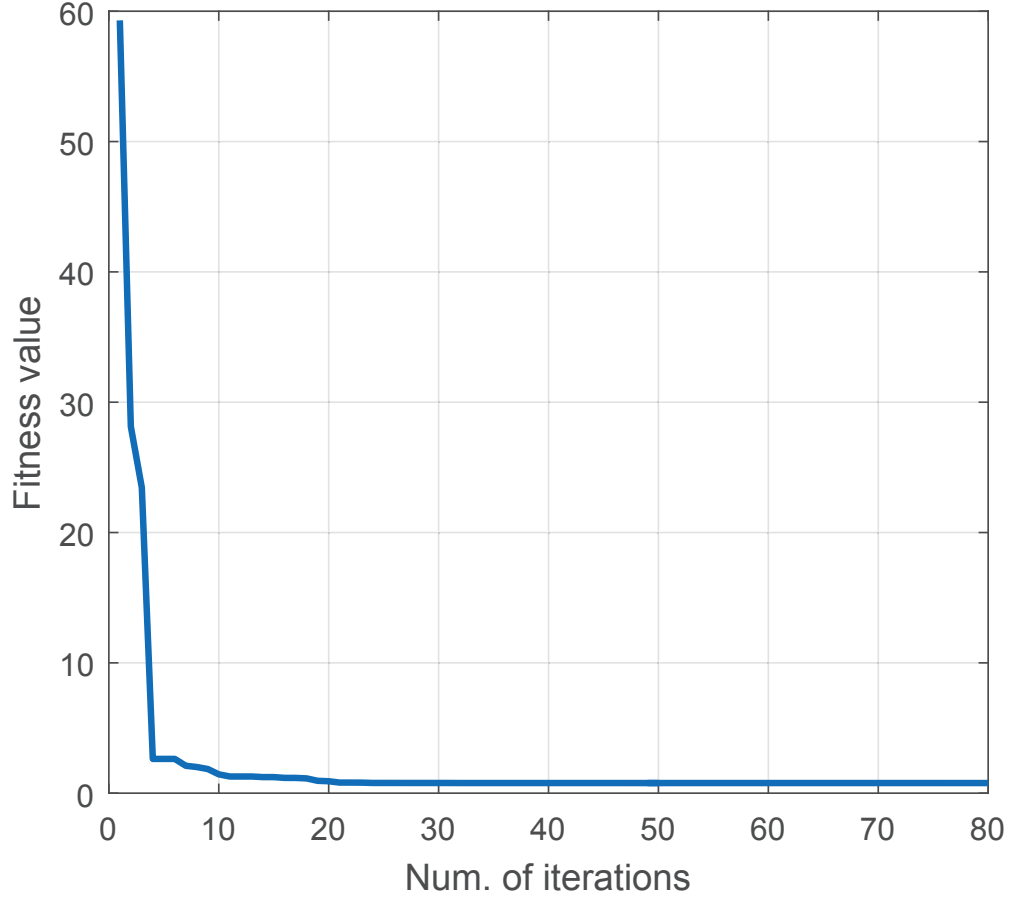


Figure 3.3: Convergence of the PSO algorithm. The algorithm converges after about 25 iterations in this case.

Regarding the LADRC position controller, a distinct feature of the ADRC theory is to estimate all the internal and external disturbance of the system plant using an extended state observer (ESO), and then take this estimated value as compensation for the original control inputs computed by corresponding nonlinear control law. Such estimation-compensation scheme can help to achieve better disturbance rejection performance. However, tuning too many control parameters makes the design of the nonlinear ADRC very difficult. Hence, the LADRC approach is proposed [115] which replaces the nonlinear control law with a linear one, as shown in Fig. 3.4. Note that the LADRC approach has much fewer parameters to tune compared to the nonlinear version. We next design the outer-loop LADRC controllers in the longitudinal and lateral channels.

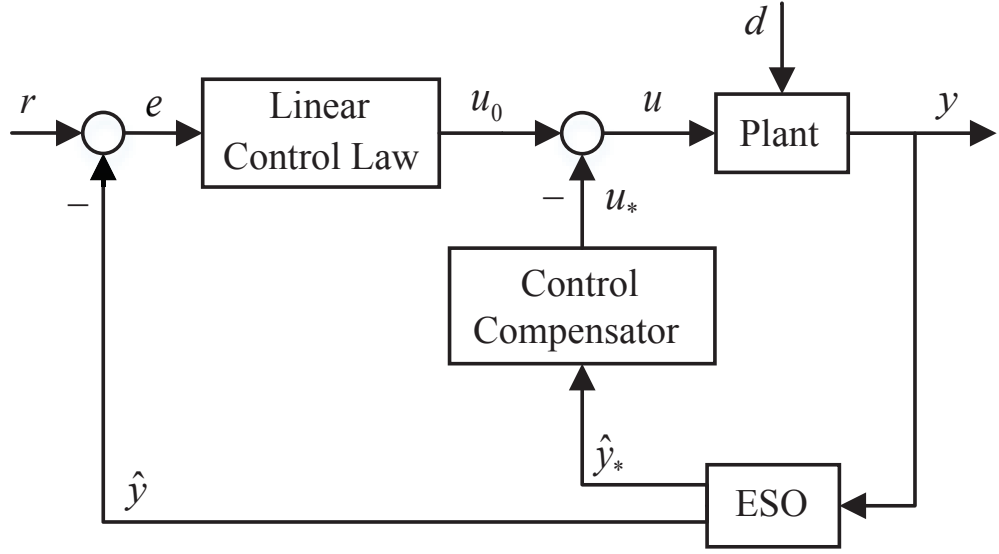


Figure 3.4: The structure of LADRC. The variables r , e , \hat{y} , \hat{y}_* , y , d denote the reference command, error signal, estimated state of the plant, extended estimated disturbance, output and disturbance applied to the plant, respectively. The variables u_0 , u_* , u denote the original control input computed by the linear control law, the compensated input computed by the control compensator and the actual control inputs to the plant, respectively.

LADRC Design in the Longitudinal Channel

In the longitudinal channel, the altitude motion of the flying wing is approximately modelled as a first-order differential equation with pitch angle θ as input and altitude H as output (assuming small flight path angle), i.e.

$$\dot{H} = V \sin(-\alpha + \theta) \approx -V\alpha + V\theta,$$

where the variable V is the forward velocity, while α is the angle of attack which is treated as a disturbance in the LADRC control design. The principle of the LADRC approach is to construct a second-order ESO with states p_{1h} and p_{2h} , where p_{1h} estimates the altitude H , and the extended state p_{2h} estimates all the possible disturbance that might affect H . With the extended state p_{2h} , the control compensator derives a compensation value u_{h*} to the control input u_{h0} . The actual control input θ_{r2} (i.e. the pitch angle command to the inner loop, see Fig. 3.1) is equal to the computed control input u_{h0} (by the linear control law) subtracted by u_{h*} . The dynamic equations of the longitudinal LADRC control system are

$$\left\{ \begin{array}{l} e_h = p_{1h} - H \\ \dot{p}_{1h} = p_{2h} - \beta_{1h}e_h + V\theta_{r2} \\ \dot{p}_{2h} = -\beta_{2h}e_h \\ u_{h*} = \frac{p_{2h}}{V} \\ \beta_{1h} = 2\omega_h \\ \beta_{2h} = \omega_h^2 \\ u_{h0} = K_{hp} \cdot (H_r - H) + K_{hd}\dot{H} \\ \theta_{r2} = u_{h0} - u_{h*}, \end{array} \right. \quad (3.5)$$

where the variable e_h is the error between the estimated altitude p_{1h} and the actual altitude H . The variables V , H_r and \dot{H} are the forward velocity, altitude command and climb rate, respectively. The parameters β_{1h} and β_{2h} are the coefficients of longitudinal ESO. K_{hp} and K_{hd} are the parameters of the linear control law. By tuning the parameters ω_h , K_{hp} and K_{hd} , good robustness and dynamic tracking performance in the longitudinal outer loop can be achieved.

LADRC Design in the Lateral Channel

In the lateral channel, as shown in Fig. 3.5, when the aircraft is making a coordinated bank turn with small heading angle η , we have

$$V\dot{\eta} \approx \frac{L}{m}\phi, \quad (3.6)$$

where L and m are the lift force and mass of the aircraft, respectively, while V and ϕ are its forward velocity and roll angle, respectively.

Under the assumption of level flight, we have $L = mg$, where g is the acceleration of gravity. Furthermore, since the time-scale of roll angle is much shorter than that of position, the dynamic characteristics of roll motion can be neglected, which leads to the equation

$$\ddot{S} = V\dot{\eta}. \quad (3.7)$$

Thus, by combining the equations (3.6) and (3.7), we have

$$\ddot{S} \approx g\phi, \quad (3.8)$$

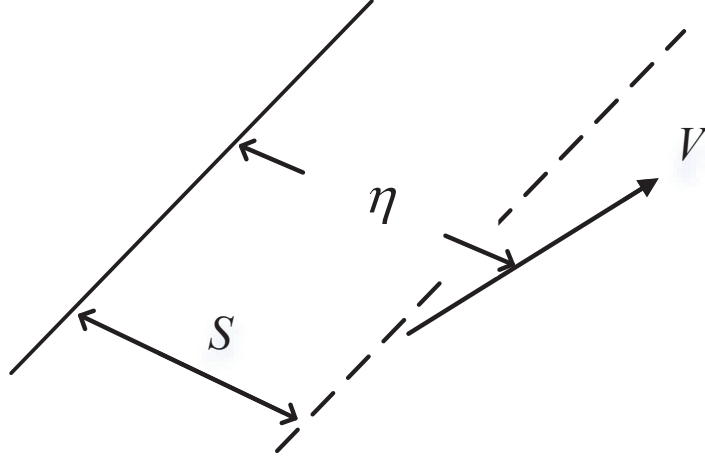


Figure 3.5: Simplified model of the lateral motion. The dashed line denotes the desired flight path and the solid line denotes the actual flight path. The lateral displacement is defined as the lateral deviation of the aircraft's current position to the desired flight path.

which indicates an approximately linear relation between the lateral displacement S and the roll angle ϕ . Then, following a similar synthesis as in the longitudinal channel, the dynamic equations of the lateral LADRC control system are obtained,

$$\left\{ \begin{array}{l} e_s = p_{1s} - S \\ \dot{p}_{1s} = p_{2s} - \beta_{1s}e_s \\ \dot{p}_{2s} = p_{3s} - \beta_{2s}e_s + g\phi_r \\ \dot{p}_{3s} = -\beta_{3s}e_s \\ u_{s*} = \frac{p_{3s}}{g} \\ \beta_{1s} = 3\omega_s \\ \beta_{2s} = 3\omega_s^2 \\ \beta_{3s} = \omega_s^3 \\ u_{s0} = K_{sp} \cdot (S_r - S) - K_{sd}\dot{S} \\ \phi_r = u_{s0} - u_{s*}, \end{array} \right. \quad (3.9)$$

where p_{1s} , p_{2s} , p_{3s} are the estimations of the lateral displacement, lateral speed,

and all the disturbance to the lateral displacement, respectively. The variable e_s is the error between the estimated lateral displacement p_{1s} and the actual lateral displacement S . g is the acceleration of gravity. S_r is the lateral displacement command. The variables u_{s0} , u_{s*} and ϕ_r are the original control input computed by linear control law, the compensation value and the roll angle command, respectively. The parameters β_{1s} , β_{2s} and β_{3s} are the coefficients of the lateral ESO. K_{sp} and K_{sd} are the parameters of the linear control law. By tuning the parameters ω_s , K_{sp} and K_{sd} , good robustness and dynamic tracking performance in the lateral outer loop can be achieved.

3.3 Simulation Study

Following the design procedure in Section 3.2, the inner-loop H_∞ controllers and the outer-loop PI/LADRC controllers in both the longitudinal and lateral channels are obtained. This section tests the performance of this aeroelastic and trajectory control system through stability analysis and numerical simulations. Note that the simulations are conducted based on the full-order nonlinear model (2.4) using the 4th-order Runge-Kutta solver *ode45* in Matlab®, and control inputs are updated at the frequency of 20Hz. All the control actuators are modelled as first-order lag systems with time constants of 0.3 seconds and the operating range of 0N~200N for thrust and $\pm 20^\circ$ for flap deflections. We refer to Section 2.4 for more details on the configurations of the very flexible flying wing model.

3.3.1 Stability Analysis

With the full-payload configuration, the open-loop system is unstable with two poles in the right half-plane, as shown in Fig. 3.6. After applying the designed inner-loop controller, the unstable poles are shifted to the left half-plane, indicating closed-loop stability. Based on the linear model, the open-loop bode diagrams of the altitude control system and the lateral displacement control system (each having an outer-loop controller and an inner-loop controller) are shown in Fig. 3.7. The gain margin and phase margin of the altitude control system are 15.1 dB and 78.9° respectively, while the corresponding stability margins of the lateral displacement control system are 12.6 dB and 65.3° , respectively. These stability margin figures show that good robustness is obtained in the closed-loop control system.

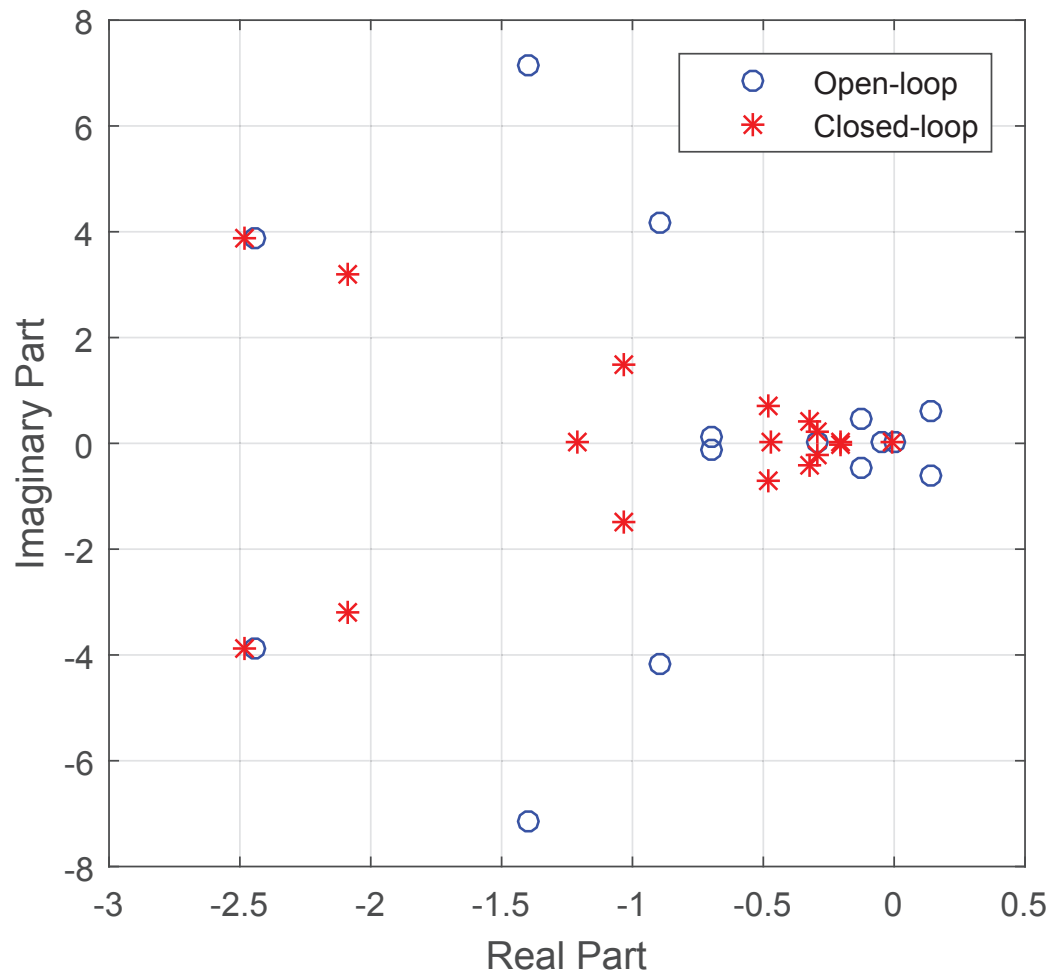


Figure 3.6: Low frequency poles in the test case. The poles are obtained based on the linear reduced-order model.

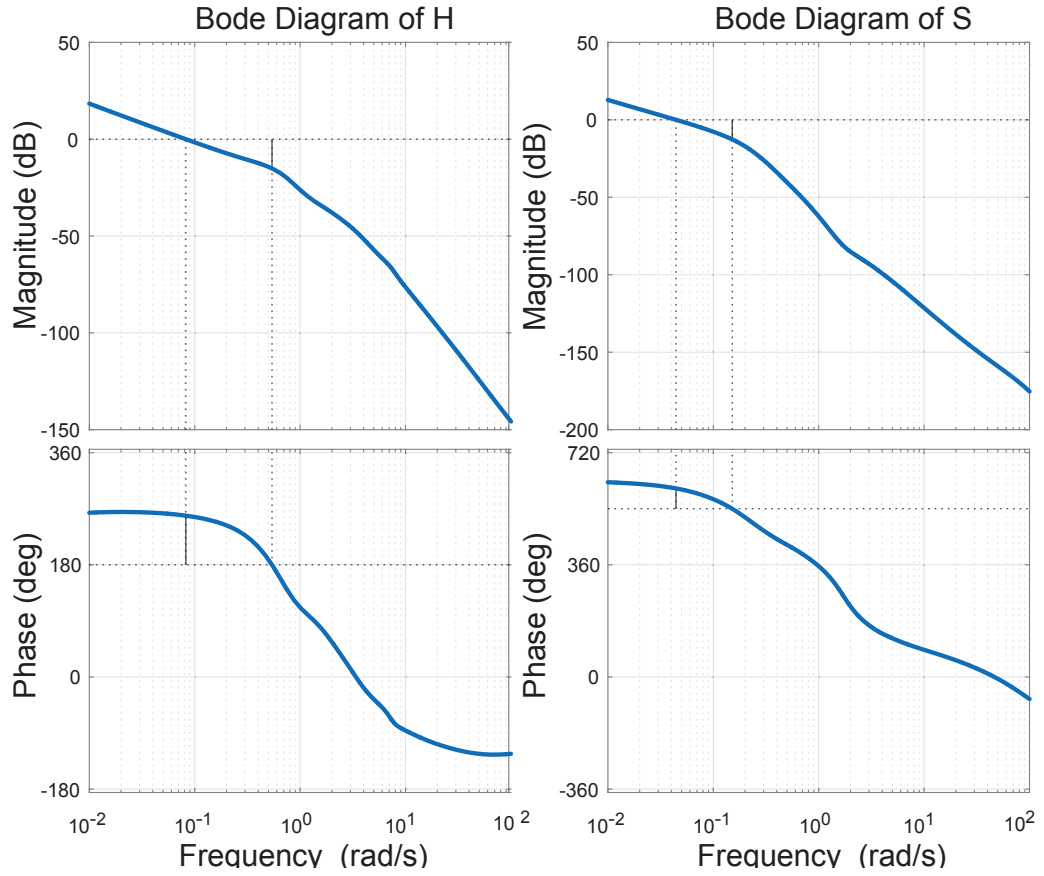


Figure 3.7: Bode diagram of the altitude control system and the lateral displacement control system. The left pair is the Bode diagram of altitude control system while the right pair is that of the lateral displacement control system.

3.3.2 Step Response

To demonstrate the dynamic tracking performance of the designed controllers, step responses of the altitude control system and the lateral displacement control system are shown in Fig. 3.8 and Fig. 3.9, respectively, along with the corresponding responses of other output measurements and control inputs. Fig. 3.8 shows that the rise time of the step response of the altitude control system is approximately 18 seconds and it has no steady error, indicating good dynamic tracking performance of the altitude control system. The pitch angle, forward velocity and root bending measurement are all maintained at their original values after the altitude reaches the desired value, respectively. The four control inputs are all in appropriate range. As shown in Fig. 3.9, similar good dynamic tracking performance is obtained by the lateral displacement control system.

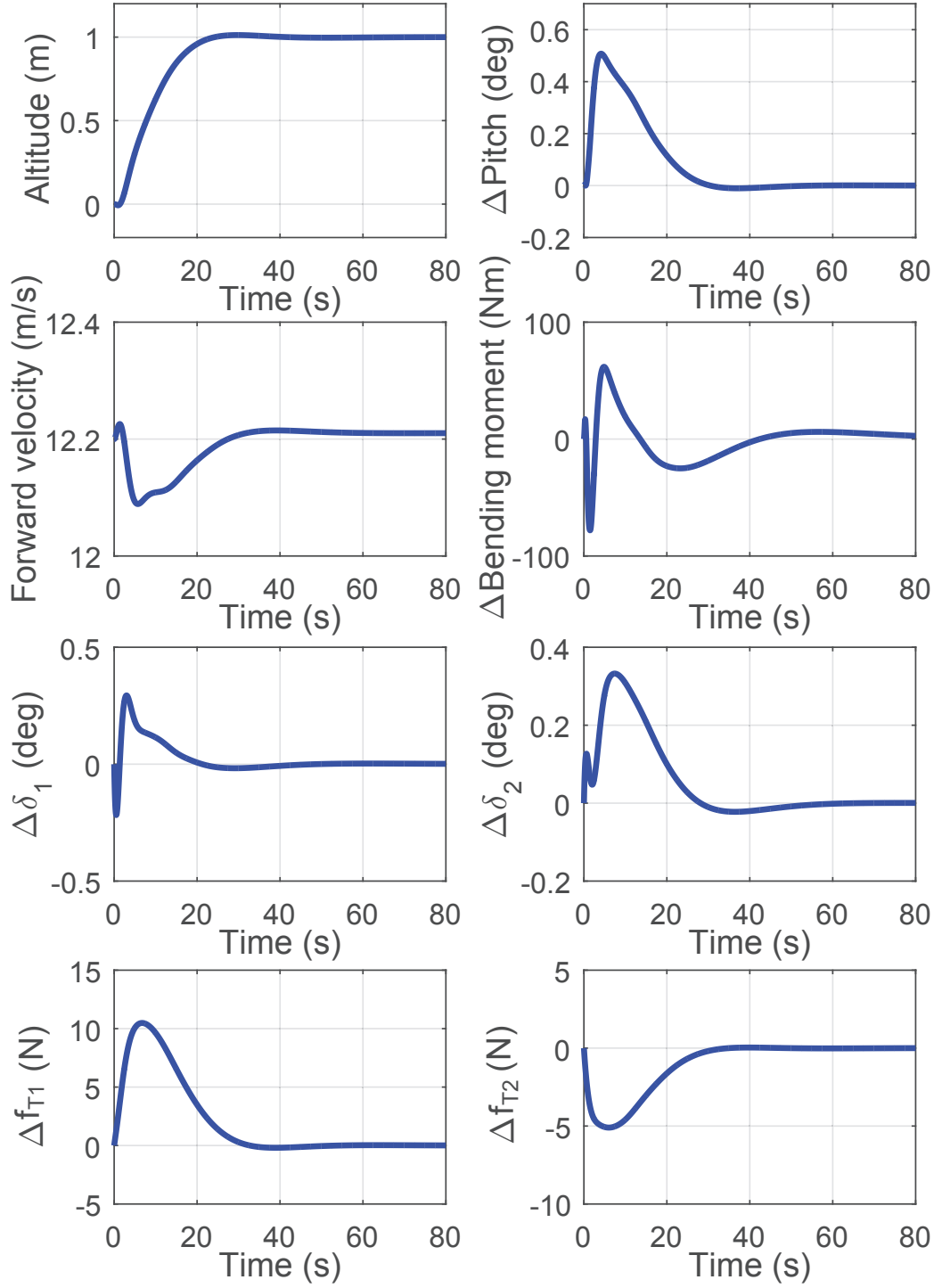


Figure 3.8: Step response of the altitude. δ_1 , δ_2 , f_{T1} , f_{T2} are the control actions of the simultaneous flap, symmetric differential flap, simultaneous thrust and symmetric differential thrust, respectively, as defined in Fig. 2.2.

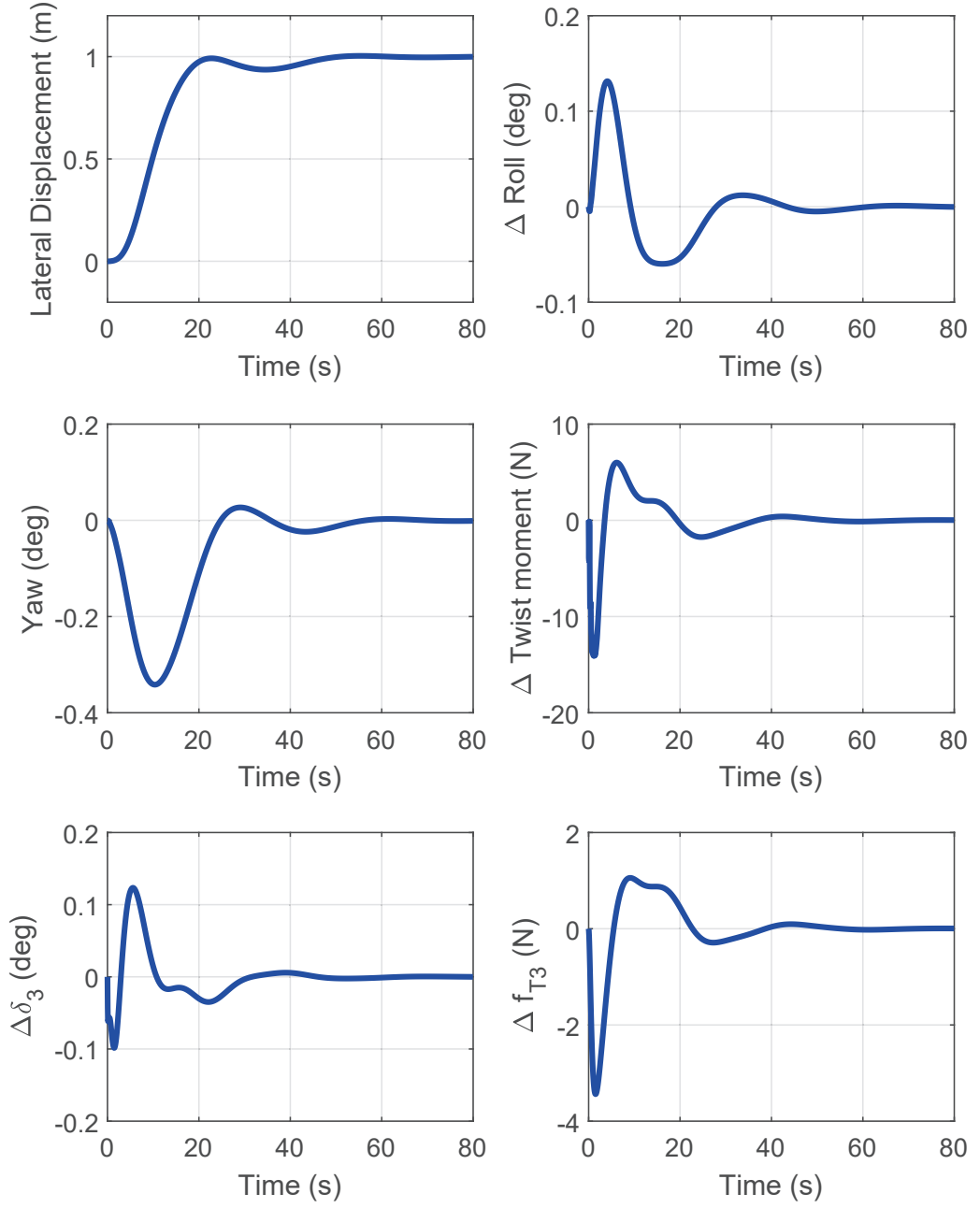


Figure 3.9: Step response of the lateral displacement. δ_3 and f_{T3} are the control actions of the antisymmetric differential flap and the antisymmetric differential thrust respectively, as defined in Fig. 2.2.

3.3.3 Trajectory Tracking Performance

We now demonstrate the trajectory tracking performance of the designed control system. Five waypoints A to E are defined by actual geographic positions (in longitude, latitude, and altitude) forming the desired flight path. The coordinates of each waypoint are summarized in Table 3.1. We use the waypoint tracking algorithm proposed in [116] (Please see **Appendix B** for more details) to guide the flying wing to track this desired flight path.

Table 3.1: Coordinates of the waypoints.

Watpoint	Longitude (West)	Latitude (North)	Altitude
A	1.54°	52.195°	0m
B	1.54°	52.235°	100m
C	1.60°	52.255°	100m
D	1.66°	52.235°	100m
E	1.72°	52.255°	200m

Fig. 3.10 shows the actual flight path of the flying wing compared with the desired one. Note that in the vertical plane (see the middle diagram in Fig. 3.10), during flying from A to B, the climb rate controller (3.4) is first switched on to control the aircraft climb up to 95% of the altitude command at a climb rate of $0.432m/s$ (the same as the one the Helios had in its mishap flight [13]), then the altitude controller (3.5) is switched on to precisely position and maintain the aircraft at the desired altitude. Same rule also applies when the aircraft flies from D to E. While in the horizontal plane (see the top diagram in Fig. 3.10), the aircraft succeeds to follow the straight line between the departure and destination waypoint. A three-dimensional view of the aircraft's actual trajectory is plotted in the bottom diagram in Fig. 3.10. It is clear that the aircraft is able to track well the desired flight path, which indicates good trajectory tracking performance of the designed control system.

3.3.4 Gust Response

This section investigates the robust performance of the control system against wind gusts. The trajectory control system aims to maintain the flying wing at $H_r = 0m$ and $S_r = 0m$ under an spanwise-varying DARPA discrete gust, which is defined as

$$u_g = \frac{U_{ref}}{2} \left(\frac{L_a}{2L_{tur}} \right)^{\frac{1}{3}} \cdot \frac{1}{2} (1 - \cos(2\pi t/t_g)) \cos(2\pi(l - l_{mid})/L_{tur}),$$

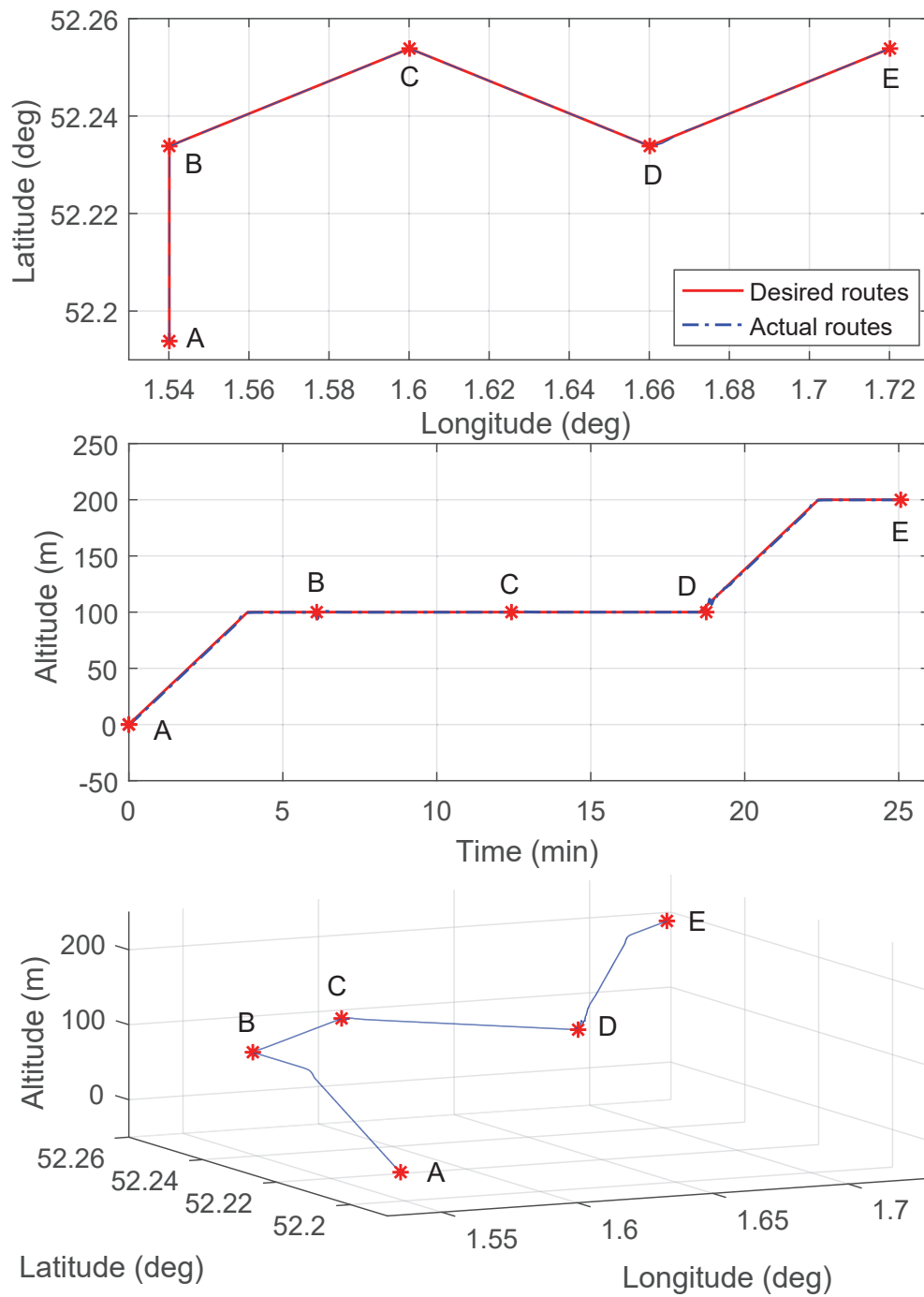


Figure 3.10: Trajectory tracking performance. The red solid line indicates the desired flight path, which are defined by the actual geographic longitude, latitude and altitudes, the blue dot-dashed line indicates the actual flight path. The red asterisks denote the defined multiple waypoints A to E.

where u_g is the strength of the discrete gust and t_g is the gust duration. The variable $U_{ref} = 5m/s$ is the reference gust amplitude, $L_a = 72m$ is the wing span, $L_{tur} = 762m$ is the turbulence scale length, l is the location along the airframe and l_{mid} is the reference location point defined as the wing's mid point. The profile of the applied wind gust is depicted in Fig. 3.11.

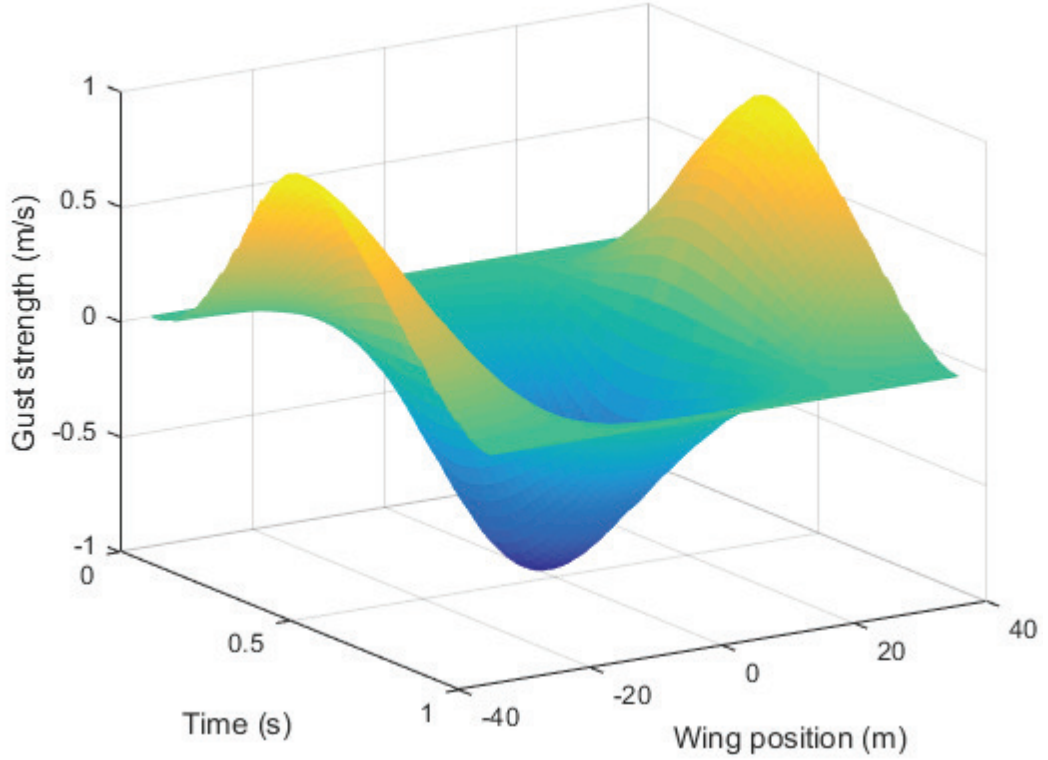


Figure 3.11: DARPA discrete gust velocity distribution with respect to position and time. The gust duration is $t_g = 1s$ in this figure.

The wind gust with different gust durations is first applied in the vertical direction, the corresponding responses of the flying wing are plotted in Fig. 3.12. It is clear that as the duration increases, the maximum deviation of the longitudinal variables becomes larger and the nonlinear effects become more significant. Correspondingly, the control system requires larger control actions to stabilize the aircraft. In all the three simulation cases, the altitude control system succeeds to maintain the flying wing at its desired altitude, indicating good disturbance rejection performance with respect to gust wind.

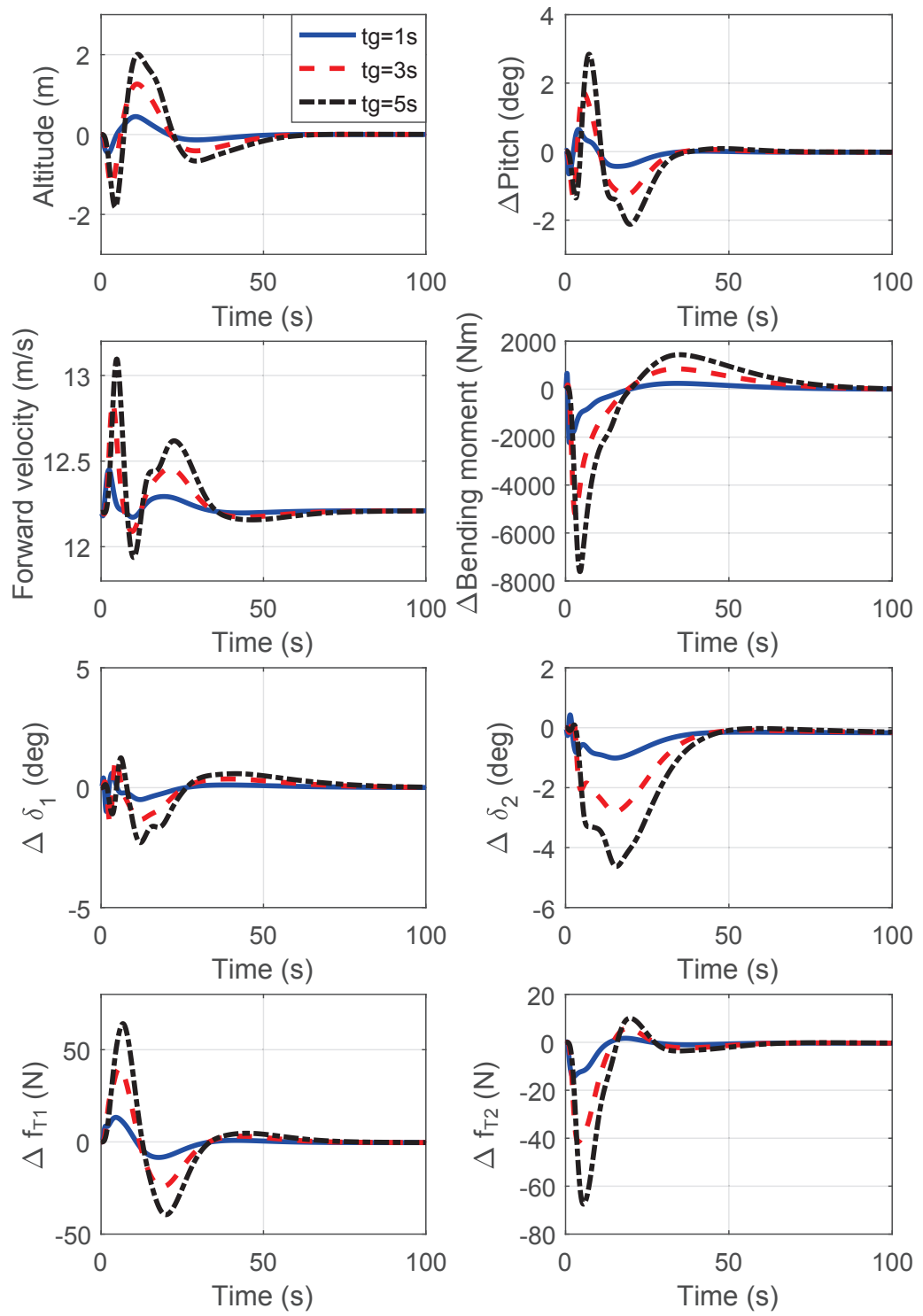


Figure 3.12: Gust wind response with gust applied in the vertical direction.

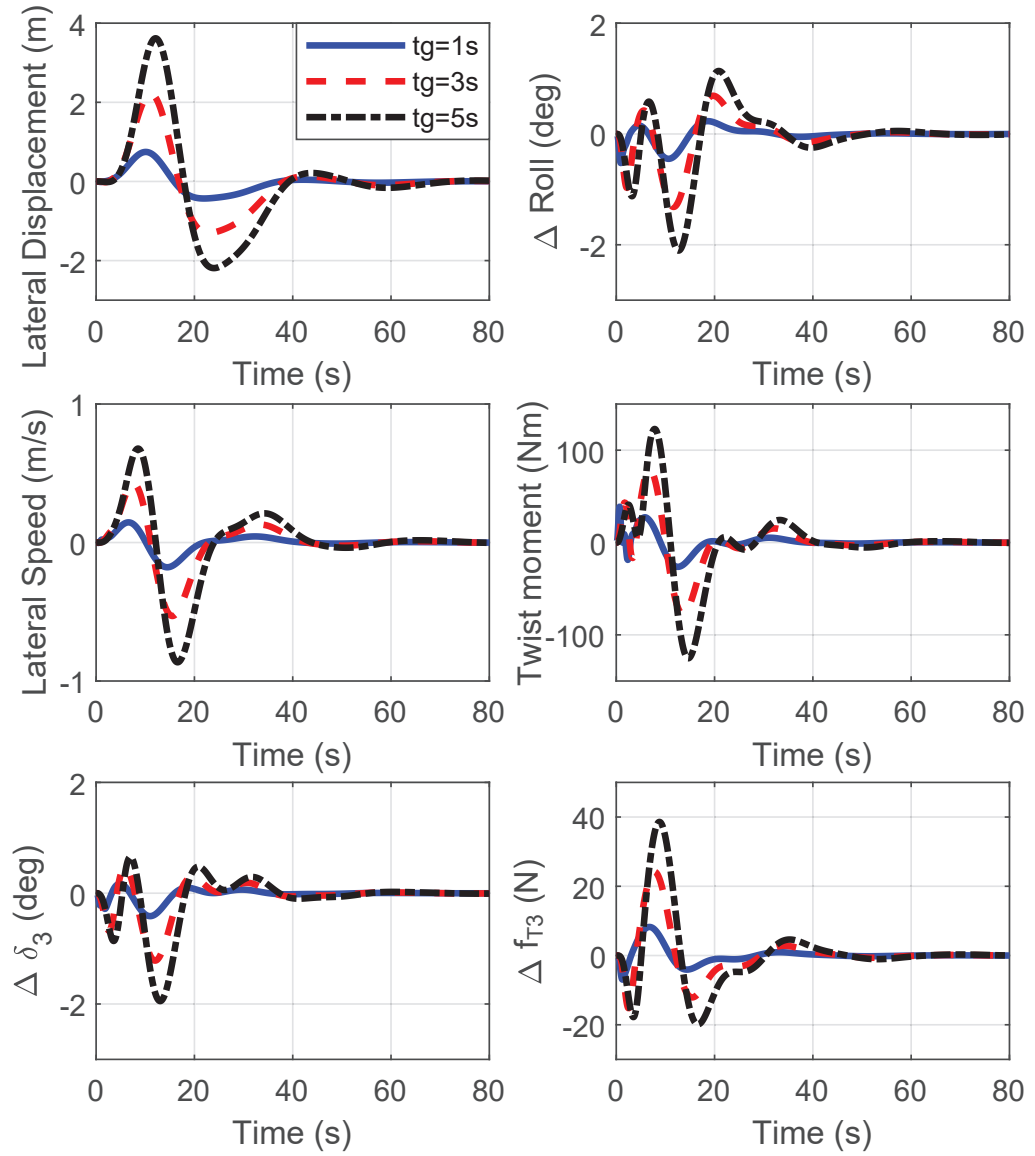


Figure 3.13: Gust wind response of lateral variables with gust applied in the lateral direction.

Gust responses of the aircraft with the same gust configurations as above but applied in the lateral direction are plotted in Fig. 3.13 and Fig. 3.14, respectively, in which similar behaviour can be observed. The lateral displacement control system succeeds to maintain the lateral deviations caused by the gust disturbance at zero. It is worth noting that due to the inherent couplings between the longitudinal channel and the lateral channel, the longitudinal variables are slightly disturbed when gust is applied in the lateral direction, as can be observed from Fig. 3.14.

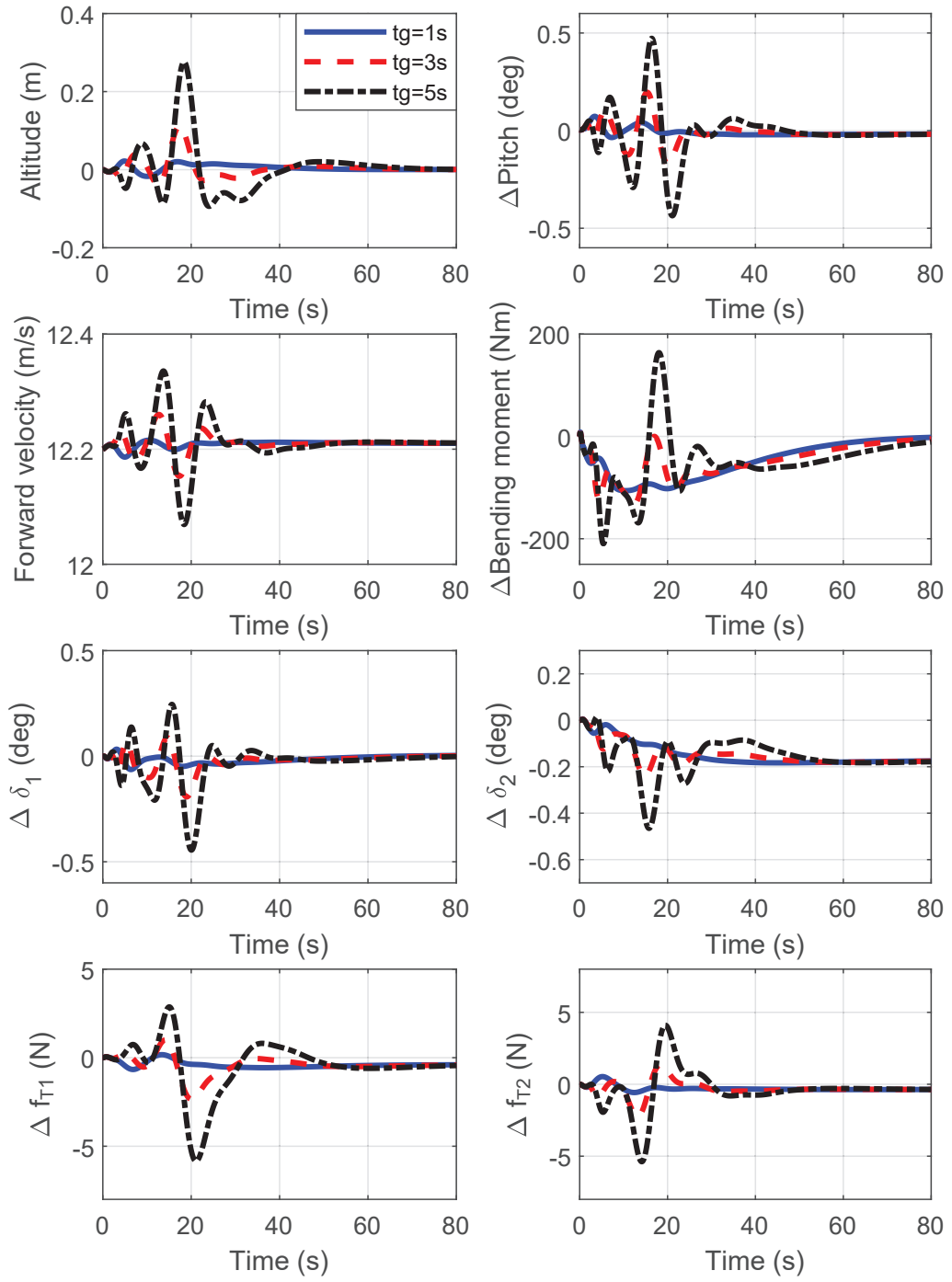


Figure 3.14: Gust wind response of longitudinal variables with gust applied in the lateral direction.

To demonstrate the advantages of the outer-loop LADRC approach, we now compare the performance of the LADRC controller with a PID controller. Taking altitude control in the longitudinal channel as an example, a PID controller is designed to serve the same purpose and tuned to have similar step response as the LADRC controller. The altitude responses of the aircraft to vertical gust wind ($t_g = 1s$, $U_{ref} = 5m/s$) with these two outer-loop controllers are shown in Fig. 3.15. While both controllers can eventually stabilize the aircraft at $H_r = 0m$, the LADRC controller (see the blue solid line) has smaller overshoot and much faster converge rate than the PID controller (see the red dashed line), indicating better disturbance rejection performance against gust wind.

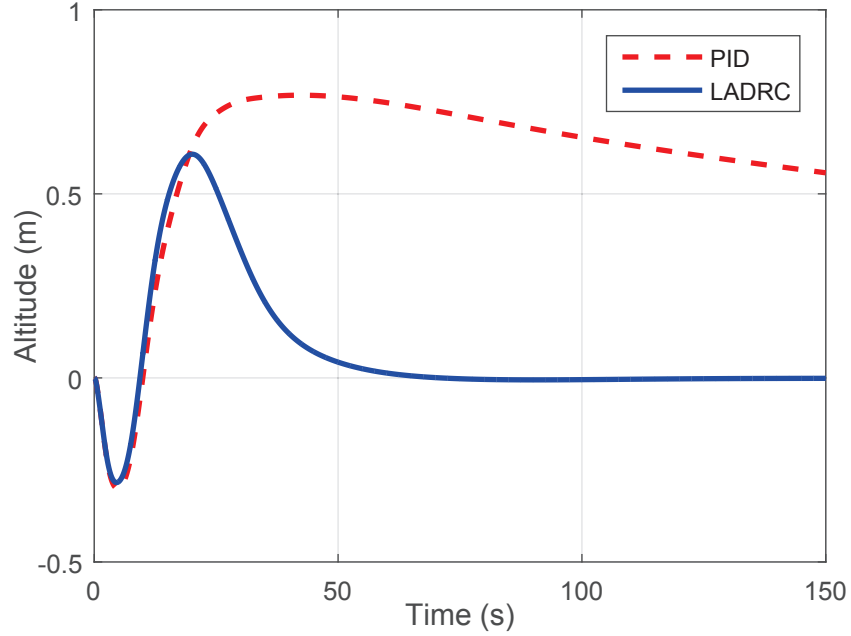


Figure 3.15: Altitude responses of a flying wing with two different types of controller (LADRC vs PID) in the longitudinal outer loop.

3.3.5 Continuous turbulence response

In this subsection, we investigate the robustness of the designed control system with respect to wind turbulence. We use the von Kármán turbulence model in Matlab[®] to generate the three-dimensional turbulence in the lateral, forward and vertical direction, respectively. The corresponding time history in each direction is shown in Fig. 3.16. Note that the Von Kármán turbulence is simply used here to provide a simulated turbulent environment and test the disturbance rejection performance of the designed control system. The three-dimensional turbulence velocity components

are applied to the model by modifying the corresponding local velocity component as explained in Chapter 2.

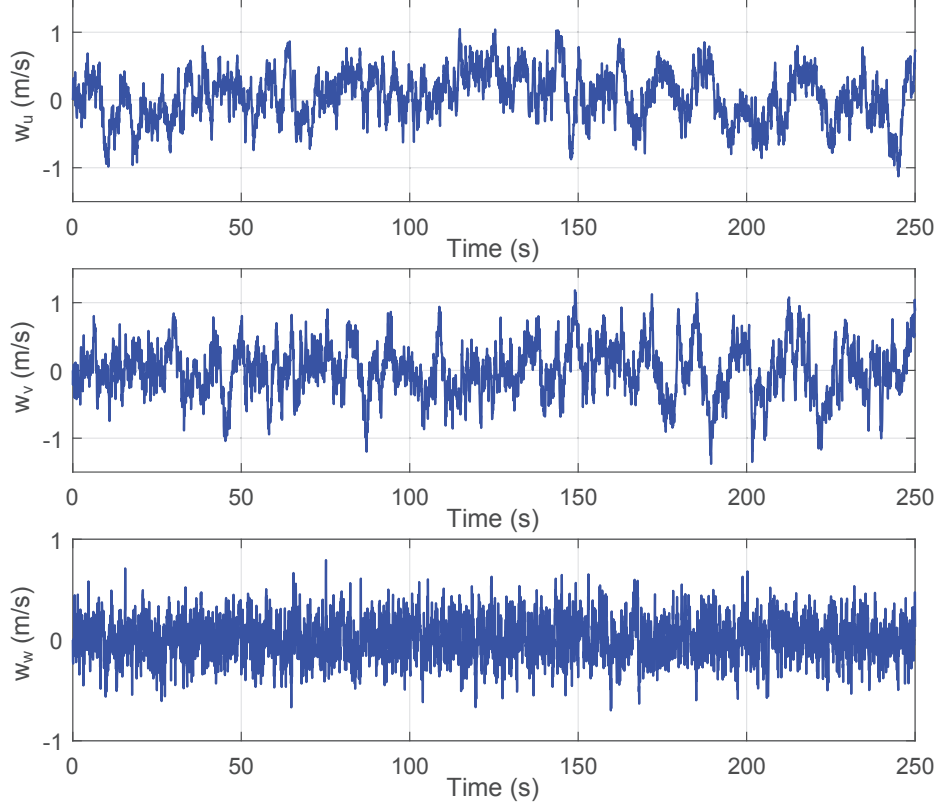


Figure 3.16: Time history of the wind turbulence used in simulations. From top to bottom are the lateral, forward and vertical components, respectively.

The flying wing has an initial $S = 10m$ lateral deviation and is given a $H_r = 20m$ altitude command. The responses of the flying wing are depicted in Fig. 3.17 and the corresponding control inputs are depicted in Fig. 3.18. Recall that we choose the center of the wing (cw) as reference point to approximate the rigid-body motions. To justify such approximation, the trajectory of the center of gravity (cg) of the aircraft is calculated and plotted together with those of cw. It is clear that the aeroelastic and trajectory control system is able to track the desired flight path in the presence of wind turbulence, while all other variables are within reasonable bounds. The trajectory of the center of gravity (cg) is consistent with that of the center of the wing (cw), as shown in the top two diagrams of Fig. 3.17, which indicates the external turbulence does not excite any vibration mode that would affect the reference point measurements. We mention that similar conclusions can be drawn in the gust wind cases in Section 3.3.4.

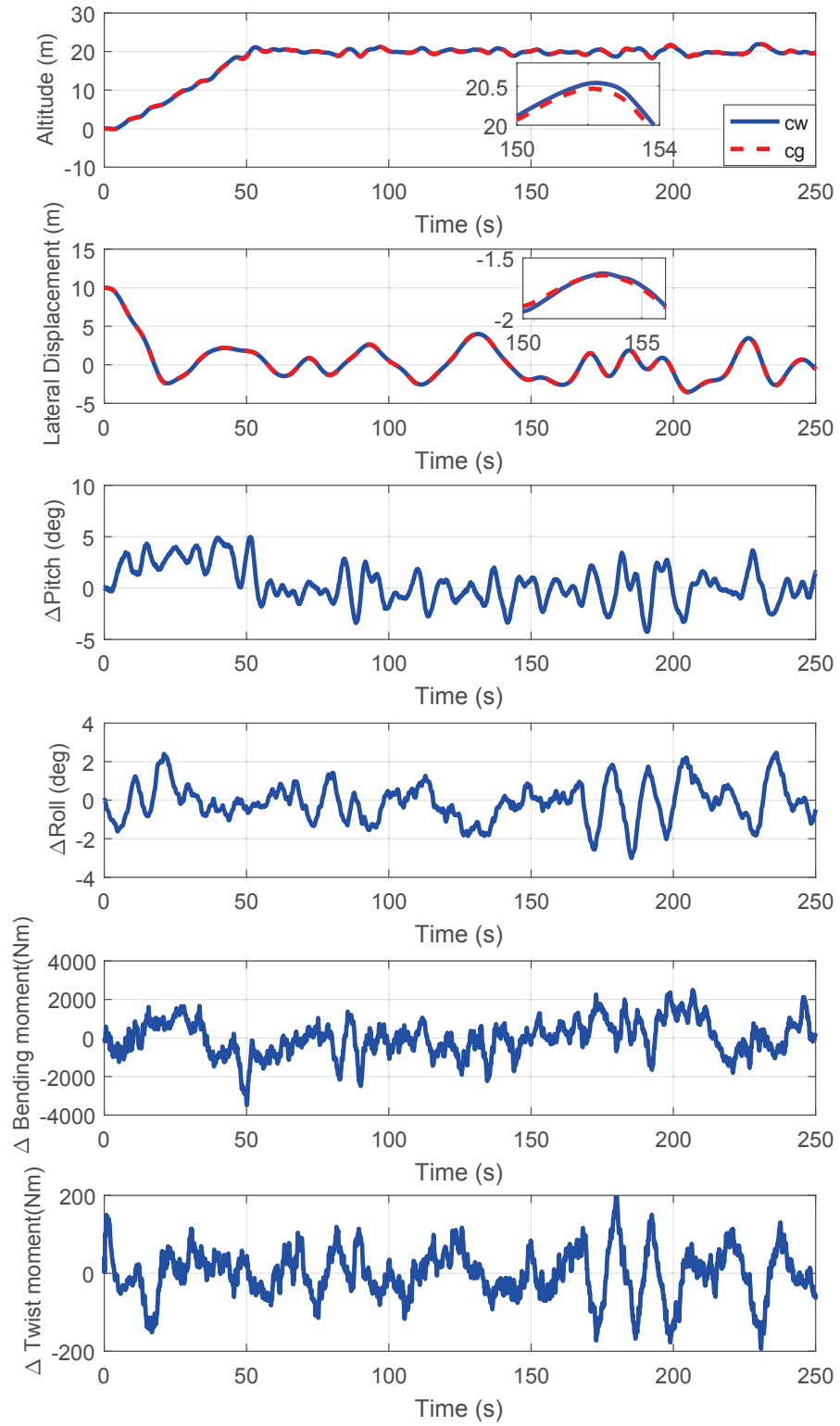


Figure 3.17: Responses with 3D turbulence applied. In the upper two subfigures, the trajectories of the center of gravity and the center of the flying wing are plotted.

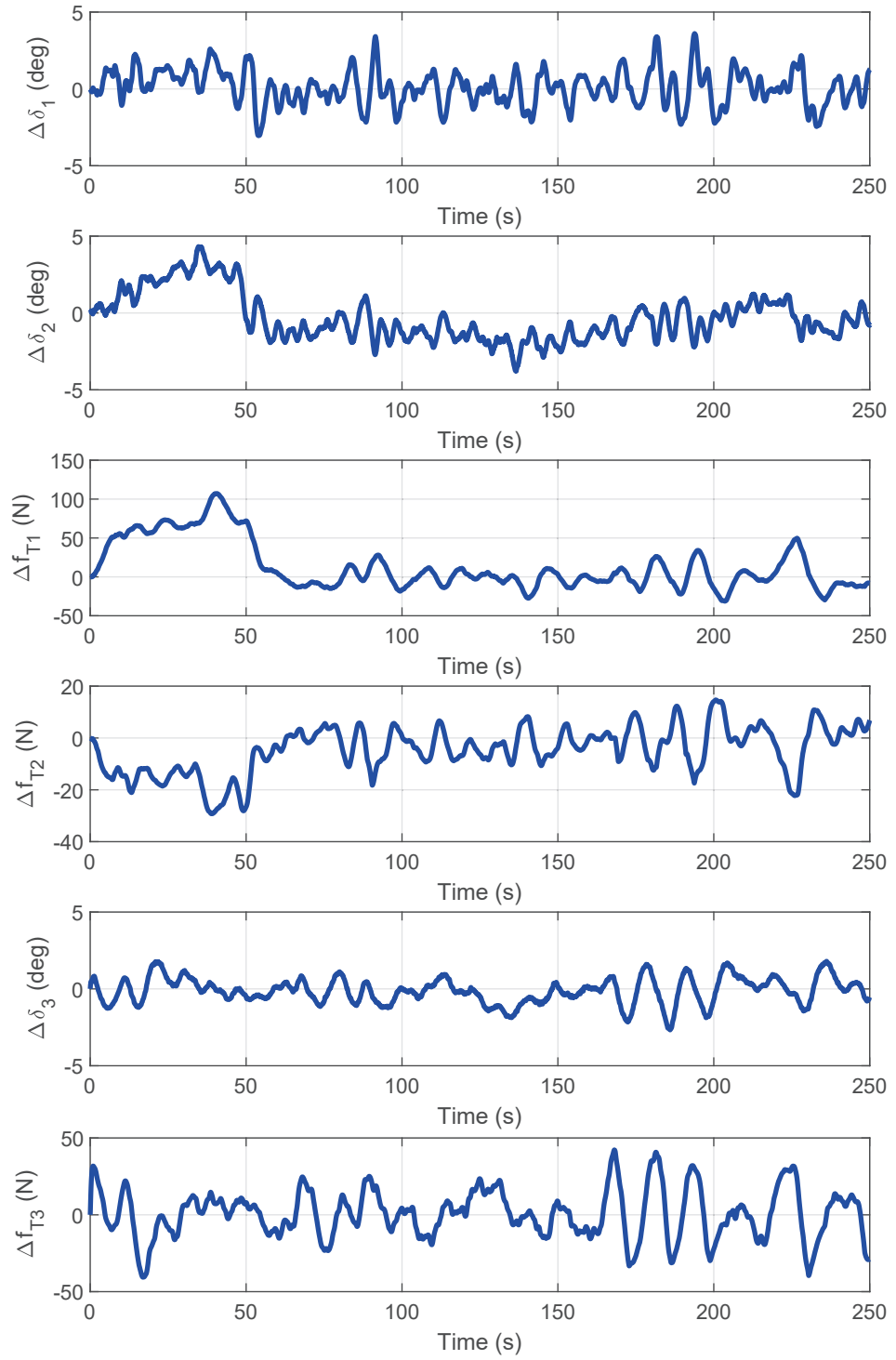


Figure 3.18: Control inputs of the responses with 3D turbulence applied.

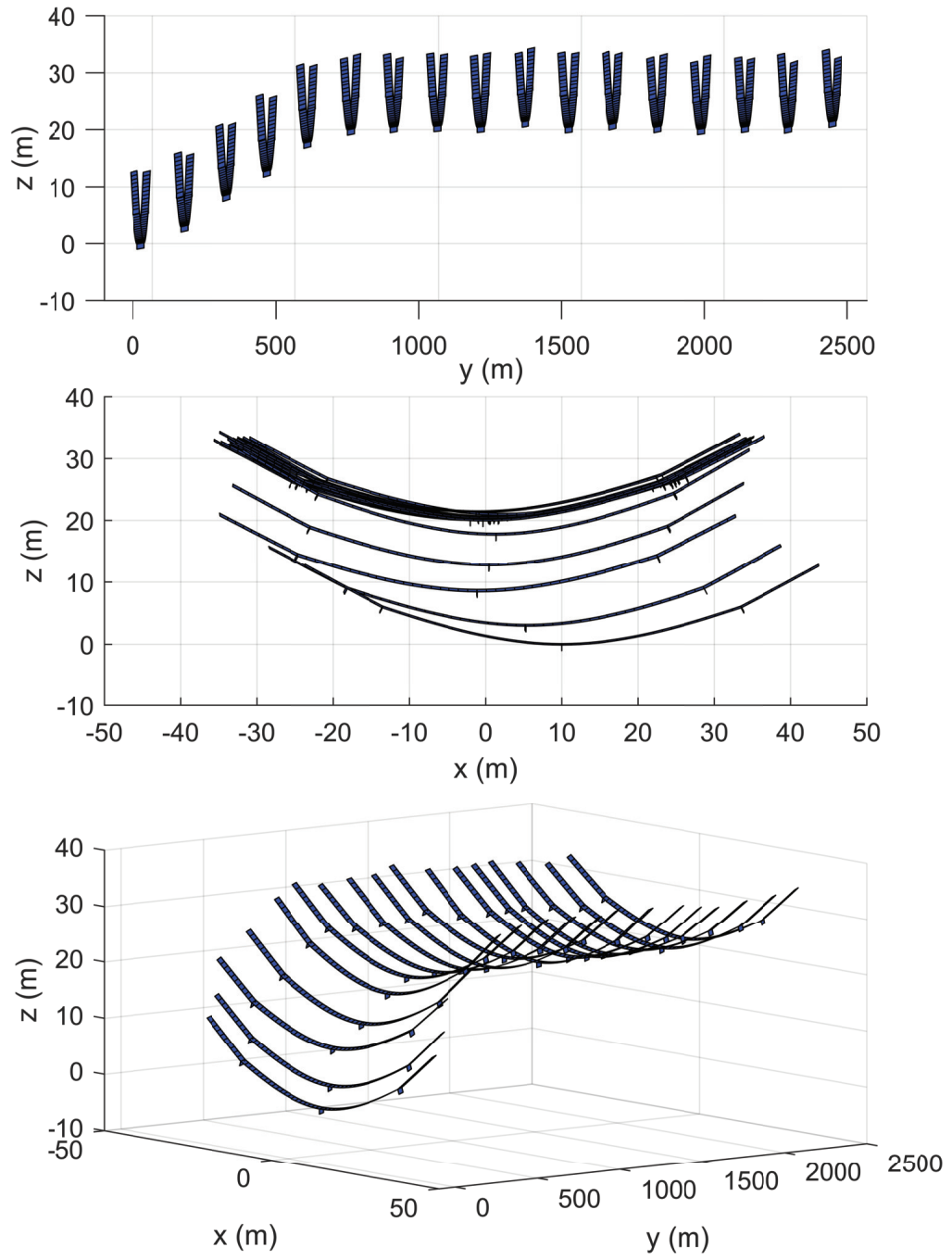


Figure 3.19: Instantaneous shape of the flying wing during flight in the presence of von Kármán turbulence. The upper, middle and lower subfigures are the side view, front view and 3D view, respectively.

Finally, we illustrate the actual shape of the flying wing in the above simulations (first 200 seconds) in Fig. 3.19. As introduced in Chapter 2, by performing a post-processing step on the modal state variables, we are able to retrieve the respective displacement and rotation orientation of each node along the airframe, which provides the geometrical information of the flying wing during flight. Fig. 3.19 shows consistent responses with those in Fig. 3.17, both indicating good robust and tracking performance of the developed aeroelastic and trajectory control system.

3.4 Conclusions

In this chapter, a two-loop control scheme based on PI/LADRC and H_∞ control technique for the aeroelastic and trajectory control of a very flexible flying wing model has been proposed. The control design was based on a reduced-order linear model (2.11) which was obtained from a full-order nonlinear model (2.4) using modal descriptions. The particle swarm optimization (PSO) algorithm was employed in the inner-loop H_∞ control design to enhance robustness and tracking effectiveness, which takes advantage of the quadratic nonlinearity information in the iterative simulation-based optimization on the reduced-order nonlinear model (2.10). Simulation tests were conducted under the full-order nonlinear aeroservoelastic model (2.4), which showed that the aeroelastic and trajectory control system achieved good performance in tracking effectiveness and robustness against disturbance rejection. Note that in these simulations, the root bending moment was assumed directly available to the control system, without considering sensor allocation to obtain such information. Therefore, it is necessary to investigate the optimisation of sensor configuration (e.g. type, number, location) in future studies to reconstruct the actual shape of the wing. Consideration of the actuator configuration for this particular flying wing model is also necessary, for example, to determine the number of flaps or thrust, the size and location of the flap surfaces, etc. Currently, the control system largely relies on normal operation of sensors/actuators, and will fail to stabilize the aircraft if loss of sensor/actuator happens. Upon considering the optimisation of sensor/actuator configurations, the fault tolerant control regarding the loss or malfunction of sensors/actuators is also necessary to investigate.

Chapter 4

Autonomous Landing Control using Lidar Preview

This chapter investigates the preview-based autonomous landing control for the very flexible flying wing model developed in Chapter 2, using short-range light detection and ranging (Lidar) wind measurements in the presence of wind turbulence. The preview-based landing control system follows the two-loop control structure as proposed in Section 3.2 and is designed based on the reduced-order linear model (2.12). The outer loop employs the same LADRC (linear active disturbance rejection control) and PI algorithms to track the reference landing trajectory and vertical speed, respectively. But the inner loop is extended to introduce Lidar wind measurements at a distance in front of the aircraft, employing H_∞ preview control to improve the disturbance rejection performance, which is crucial in the autonomous landing scenario for very flexible aircraft (VFA). Simulation tests are conducted based on the full-order nonlinear aeroservoelastic model (2.4) to demonstrate the landing effectiveness and disturbance rejection performance of the designed preview-based landing control system, compared to a baseline landing control system without preview. The control system's robustness to measurement errors in the Lidar system is also demonstrated.

4.1 Introduction

As a critical flight phase, landing determines whether an aircraft can be safely recovered. Statistics show that nearly half of the aircraft accidents occur during landing [117], and the autonomous landing in the presence of atmospheric disturbance (such as windshears, crosswinds, etc.) is still one of the current bottlenecks

in large UAV development. For example, the HALE UAV Aquila developed by Facebook was reported to be substantially damaged in a crash due to sudden wind gusts during landing [15]. These imply the demand to develop effective methods in aspect of autonomous landing control of VFA. Current research on autonomous landing control is mostly devoted to rigid-body aircraft [118–126] and has rarely touched flexible ones. Hoseini et al. [127] developed a landing control system for a simple flexible aircraft based on LQR/integral/feedforward control. They employed LQR control to track the landing commands with an integrator to eliminate the steady-state error and a feedforward controller to reduce the effects of disturbance (which were assumed to be measurable). The control system could steer the aircraft through the landing path successfully in the presence of constant crosswinds. However, the controller required full state feedback and did not consider turbulent wind situations. Their nonlinear aircraft model was also relatively stiff.

The contribution of this chapter is to investigate the autonomous landing control of VFA using Lidar preview to improve control performance in the presence of wind turbulence. Lidar can be used to measure the line-of-sight (LOS) component of the approaching wind disturbance at a distance ahead of the aircraft by detecting the Doppler shift in atmospheric backscatter [128–130]. With specific scanning pattern, one is able to retrieve the three-dimensional velocity components [131], which can be provided to the control system as preview knowledge. In this manner, the preview controller has access to the time-advanced measurement of wind disturbance in addition to the feedback signals on the aircraft state [132]. This enables the preview control system to act before the wind disturbances actually affect the aircraft, therefore improves the control performance, which can largely benefit the autonomous landing control of VFA. Preview control with Lidar wind measurements have been widely used in wind turbine control [133–137]. For their applications in flight control, Rabadan et al. [138] developed and flight-tested an airborne forward-looking Lidar system on an Airbus A340-300 testbed. Flight test measurements showed that the designed Lidar system was potential for future implementation in a real-time feedforward flight control system. The work of [139–141] investigated the gust load alleviation problem using Lidar preview measurements of the incoming gust, based on model predictive control, gain-scheduled linear parameter-varying control and adaptive feedforward control, respectively. Their simulation results showed that the wing root bending moments or average vertical acceleration were largely reduced, indicating better load alleviation performance and disturbance rejection performance by the aid of preview control scheme. In addition to Lidar wind measurements, Hesse and Palacios [72] investigated the gust load alleviation problem for flexible

aircraft in wake vortex encounters, where the gust is assumed to be measured at the aircraft nose via a 5-hole probe and used as prior information. Simulation results showed that the combined feedforward/feedback H_∞ controller and the use of direct lift control surfaces obtained significant load reductions.

As mentioned earlier, we aim to investigate the autonomous landing control using Lidar preview for the very flexible flying wing model developed in Chapter 2. Its aeroelastic and trajectory control (without preview) was previously studied in Chapter 3, which employed a two-loop control structure in each of the longitudinal and lateral channels to realize efficient trajectory tracking. The outer loop employed PI/LADRC algorithms to track the desired trajectory and generate attitude angle command to the inner loop, based on which the inner loop used H_∞ control to compute the control inputs to the corresponding control actuators. To achieve preview-based landing control, we use the same outer-loop controllers but extend the inner-loop H_∞ control structure developed in Section 3.2 by introducing Lidar preview wind measurements as prior information. We design a Lidar simulator to measure the incoming wind disturbance in the wind field, and then augment the plant model with this preview measurement through a discrete-time delay chain. We obtain the preview controllers through discrete-time mixed sensitivity H_∞ synthesis [142] with the augmented plant model. A landing trajectory generator (guidance system) is also developed to generate real-time reference commands for the landing control system. The control design is again based on a reduced-order linear model (2.12) (thus robustness of the controller is very important) while simulation tests are conducted based on the full-order nonlinear model (2.4). Simulation results show that the preview-based landing control system has achieved better landing effectiveness and disturbance rejection performance compared to a baseline landing control system (without preview) which is adapted from the aeroelastic and trajectory control system designed in Chapter 3, indicating more efficient and safer autonomous landing. The control system's robustness against measurement noise in Lidar wind measurements is also demonstrated.

The structure of this chapter is organized as follows: Section 4.2 develops the landing trajectory generator to generate real-time reference commands for the landing control system. Section 4.3 develops the Lidar simulator to measure the three-dimensional velocity components of the incoming wind disturbance in the wind field. Section 4.4 designs the preview-based landing control system based on a two-loop PI/LADRC and H_∞ preview control scheme for the very flexible flying wing and Section 4.5 conducts simulation studies to test the performance of the control system. Section 4.6 concludes this chapter.

4.2 Landing Trajectory Design

This work assumes the wheeled landing recovery method. This means that the aircraft tracks a pre-defined descent trajectory precisely and touches down near the desired touchdown point with appropriate vertical speed and attitude angle. Normally, the landing process consists of three main phases, the final approach phase, the flare phase and the taxi phase. As illustrated in Fig. 4.1, when the aircraft descends to a pre-defined altitude H_0 and is commanded to land, it enters the final approach phase where it glides down quickly in uniform linear motion at constant flight path angle γ_L . Then as the aircraft further glides down to the pre-defined altitude H_1 , it enters the flare phase where it descends slowly at a gradual trajectory and simultaneously adjusts its vertical speed and attitude angle to guarantee safe touchdown at point O . The aircraft enters the taxi phase from point O , where it keeps slowing down and taxiing on the runway till stopping.

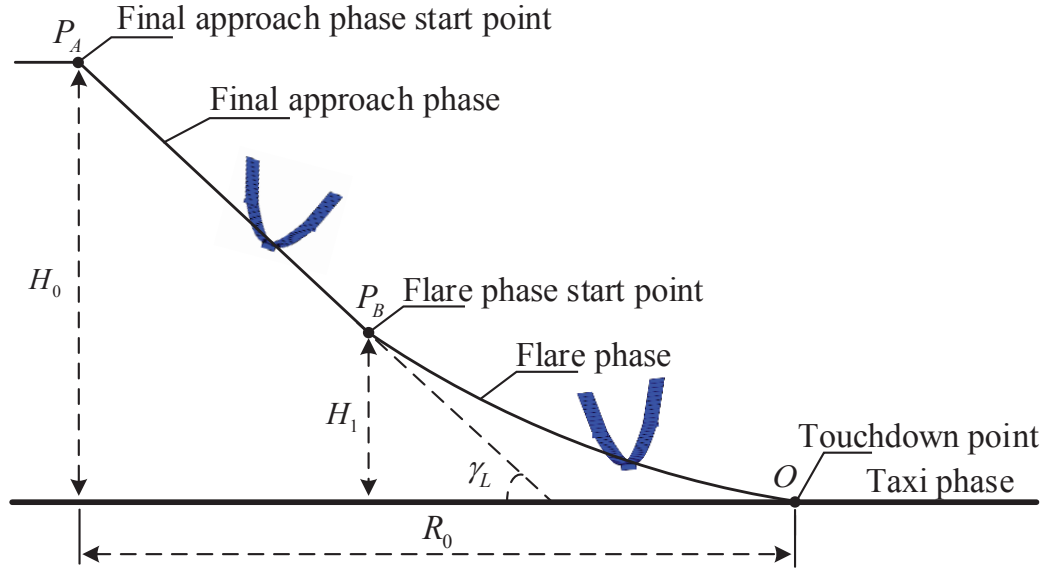


Figure 4.1: Illustration of the landing process. R_0 is the projected distance from the final approach phase start point P_A to the desired touchdown point O . P_B is the flare phase start point and O is the desired touchdown point. γ_L is the descent flight path angle in the final approach phase.

The aircraft is expected to effectively follow this landing trajectory during landing. Poor tracking effectiveness of the desired descent path during the final approach phase may result in the aircraft entering the flare phase with large deviations of the flare phase start point, which may subsequently cause large deviations of the touchdown point O , eventually leading to a possible failed landing. Therefore, an

efficient and robust autonomous landing control system is required. In this work, we only focus on the in-air final approach and flare phases which are of crucial importance in autonomous landing. Note that the midpoint of the flying wing is selected as reference point to track the altitude H and the flight path angle γ_L of the aircraft.

In the longitudinal channel of the final approach phase, the landing trajectory of the aircraft is a straight line whose slope is determined by the descent flight path angle γ_L . The flying wing is desired to track this straight line, we thus define the altitude command for the final approach phase as

$$H_r(R) = H_0 + (R_0 - R) \tan \gamma_L + H_\Delta. \quad (4.1)$$

where R is the projected travelling distance since entering the final approach phase, $H_\Delta = k\gamma_L + b$ is a pre-compensator (depending on the flight path angle γ_L only) introduced to compensate the slow altitude response of the control system when tracking a time-dependent altitude command, such that the flying wing can follow the desired descent trajectory effectively in the final approach phase. The parameters k and b can be obtained via simple tuning with a designed longitudinal control system.

While in the longitudinal channel of the flare phase, the altitude is expected to be reduced exponentially. As employing altitude tracking in this phase may cause large pitch angle motion when approaching the touchdown point in the presence of wind disturbance which increase the risk of structural impair, we employ vertical speed control instead of altitude tracking to ensure the aircraft achieves appropriate touch down speed and pitch angle for safe landing. Although this may result in the loss of touch down effectiveness in disturbance, the situation can be improved by the preview-based landing control system which will be demonstrated later in Section 4.5.3. Therefore, we define the vertical speed command for the flare phase as

$$\dot{H}_r(R) = v_{zr} + \frac{(v_{z0} - v_{zr})}{H_1} H, \quad (4.2)$$

where v_{z0} is the instantaneous vertical speed at the flare phase starting point and v_{zr} is the desired vertical speed at the touchdown point. Furthermore, the forward velocity is required to maintain at its trim value (i.e. $V_r = V_{trim}$) in both phases.

In the lateral channel, the trajectory of the flying wing is expected to align with the center of runway in both the final approach and flare phases. Hence, the reference command for the lateral displacement (defined as the lateral deviation from current position to the center of runway) is simply given as $S_r = 0$. Combining

all the reference commands above, a landing trajectory generator is designed to generate the corresponding real-time reference commands for the landing control system, as shown in Fig. 4.2. The first three of the four commands are fed into the landing control system in the final approach phase while the last three of the four commands are utilised in the flare phase.

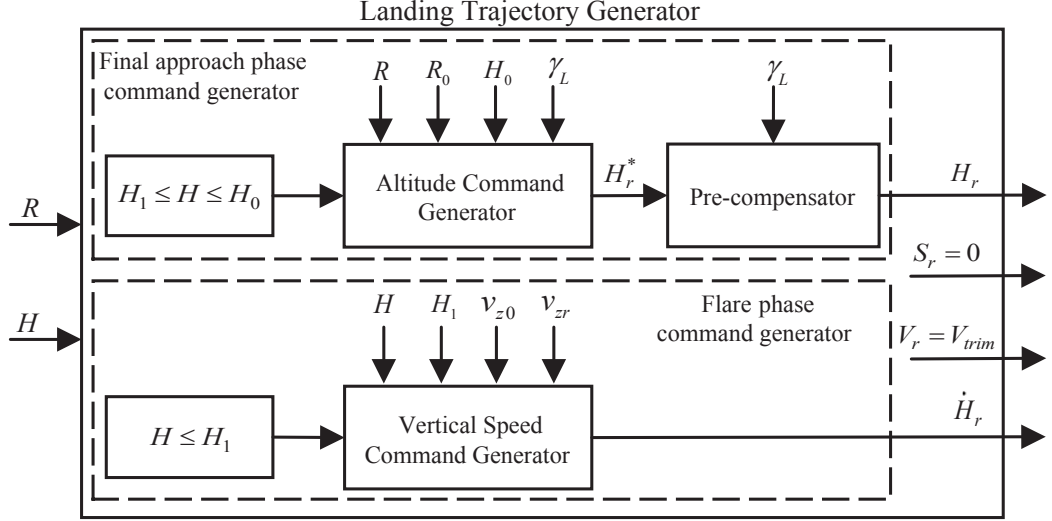


Figure 4.2: Structure of the landing trajectory generator. Pre-defined parameters include the projected travelling distance since entering the final approach phase (R), the projected distance from the final approach phase starting point to the desired touchdown point (R_0), altitude of the final approach phase starting point (H_0) and the flare phase starting point (H_1), the descent flight path angle (γ_L) and the desired vertical speed at the touchdown point (v_{zr}). H is the aircraft's current altitude.

4.3 Lidar Simulator Design

In this section, we design the Lidar simulator to measure the wind disturbance at a distance in front of the aircraft, which will be used as prior knowledge for preview control design. We extend the Lidar simulator based on the work of [143, 144] to measure the three-dimensional velocity components of the wind disturbance using Velocity Azimuth Display (VAD) technique [131].

4.3.1 Line-of-Sight Wind Measurement

Assuming that in the inertial reference frame, the coordinates of the Lidar system which is fixed at the center of the flying wing are $[x_a, y_a, z_a]^\top$ and the coordinates of the measurement point i at a distance r_i in front of the Lidar system are $[x_i, y_i, z_i]^\top$.

Given the actual wind velocity $[u_i, v_i, w_i]^\top$ at point i , we calculate its line-of-sight (LOS) component of the wind as

$$v_{los,i} = \int_{-\infty}^{\infty} (x_{n,i}(u_i - \dot{x}_a) + y_{n,i}(v_i - \dot{y}_a) + z_{n,i}(w_i - \dot{z}_a)) f_{rw}(a) da, \quad (4.3)$$

where $[x_{n,i}, y_{n,i}, z_{n,i}]^\top$ is the normalized laser beam vector from the Lidar system to the measurement point i (i.e. the focus of the laser beam), and $[\dot{x}_a, \dot{y}_a, \dot{z}_a]^\top$ is the velocity of the Lidar system. f_{rw} is a normalized spatial weighting function to consider the fact that Lidar measures within the probe volume the beam intersects, as shown in Fig. 4.3. Essentially, the lidar wind measurement is not simply a point measurement but a weighted average of wind speeds in a certain volume of air.

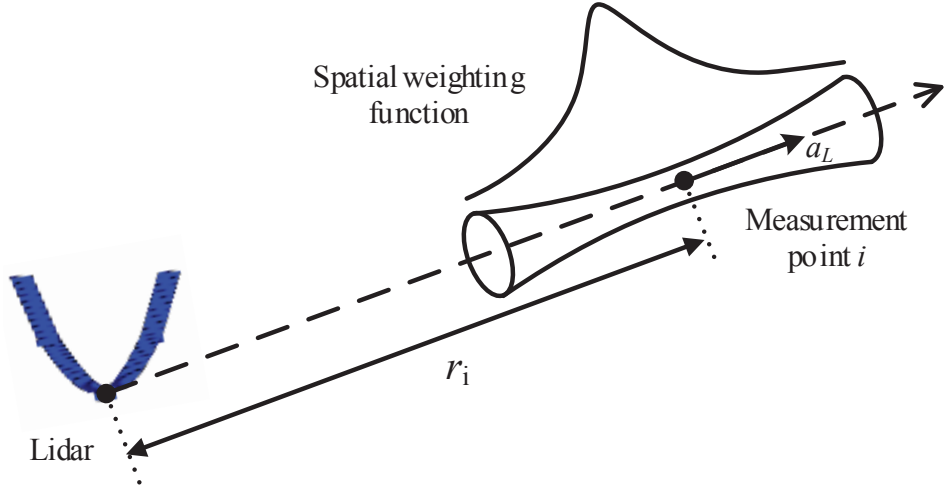


Figure 4.3: Illustration of the line-of-sight measurement.

The spatial weighing function is given in the form of [143]

$$\begin{cases} f_{rw}(a_L) = \frac{1}{\eta_L \sqrt{2\pi}} \exp\left(-\frac{a_L^2}{2\eta_L^2}\right), \\ \eta_L = \frac{W_L}{2\sqrt{2 \ln 2}}, \end{cases} \quad (4.4)$$

where a_L is the distance from focus point along the laser beam and W_L is the size of sampling volume. The spatial weighting function effectively acts as a low-pass filter to the wind disturbance measurements. We assume $W_L = 10m$ and $r_i = 24.4m$, which corresponds to a two-second preview time with respect to the aircraft's speed $12.2m/s$.

4.3.2 Three-dimensional Wind Measurement

We now employ the Velocity Azimuth Display (VAD) technique [131] to retrieve the three-dimensional velocity components of the wind disturbance, assuming the spatial velocity fluctuations of wind turbulence along the airframe is small. The Lidar system is designed to scan conically towards the forward direction at a fixed elevation angle φ_L , measuring the LOS wind velocity at a certain number of points with different azimuth angle λ_{Li} , as depicted in Fig. 4.4. In this manner, we obtain a set of LOS wind measurements.

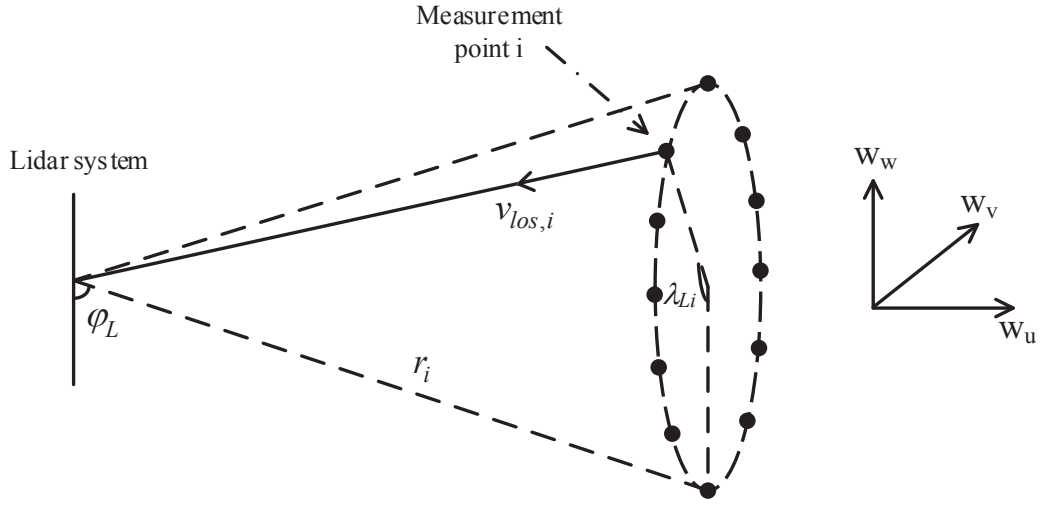


Figure 4.4: Illustration of the Lidar scanning pattern. w_u, w_v, w_w are the respective mean value of the three-dimensional velocity components of the wind disturbance in the measurement plane. The number of measurement points is assumed to be 12 in this work.

It is obvious that the wind velocity of these LOS measurement data can fit into a sinusoidal or cosine function with respect to azimuth angle, for which we have

$$v_{fit}(\lambda_L) = m_L + n_L \cos(\lambda_L - \lambda_{L_{\max}}). \quad (4.5)$$

where $\lambda_{L_{\max}}$ is the azimuth angle which corresponds to the peak of the fitted wave, m_L is the mean value and n_L is the peak deviation to the mean value, respectively. Please see Fig. 4.5 for illustration of these variables.

On the other hand, the actual velocity of the LOS wind measurements at different azimuth angle λ_L is derived as

$$v_{actual}(\lambda_L) = u_l \sin \varphi_L + v_l \cos \varphi_L \sin \lambda_L - w_l \cos \varphi_L \cos \lambda_L, \quad (4.6)$$

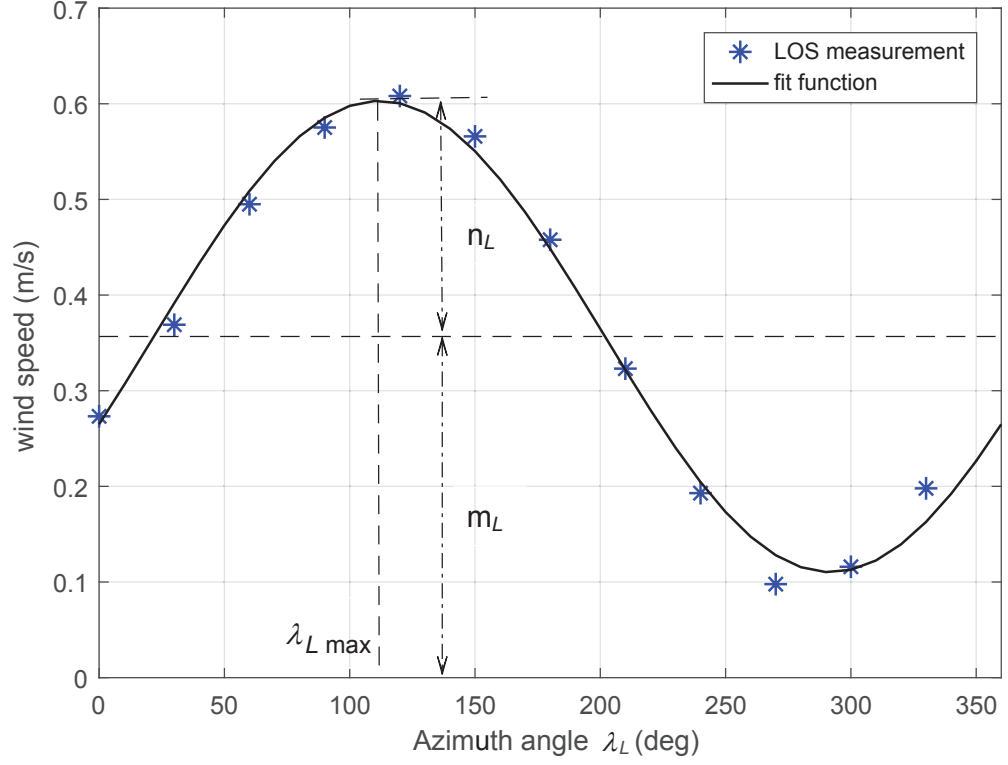


Figure 4.5: Illustration of the measurement data fitting. The asterisks denote the set of LOS measurement data during a scanning cycle, the solid line is the fitted function.

where $[u_l, v_l, w_l]^\top$ is the resultant velocity of the average wind velocity and the aircraft velocity. By setting $v_{actual}(\lambda_L) = v_{fit}(\lambda_L)$, we get the respective mean value of the three-dimensional components of this resultant velocity as

$$\left\{ \begin{array}{l} u_l = \frac{m_L}{\sin \varphi_L}, \\ v_l = \frac{n_L \sin \lambda_{L \max}}{\cos \varphi_L}, \\ w_l = \frac{-n_L \cos \lambda_{L \max}}{\cos \varphi_L}. \end{array} \right. \quad (4.7)$$

Assuming the wind disturbance travel with mean speed from the measurement location to the aircraft using the Taylor's Hypothesis of Frozen Turbulence [145], we obtain the mean value of the velocity of wind disturbance as

$$\begin{cases} \tilde{w}_u = u_l - \dot{x}_a, \\ \tilde{w}_v = v_l - \dot{y}_a, \\ \tilde{w}_w = w_l - \dot{z}_a, \end{cases} \quad (4.8)$$

where $[\dot{x}_a, \dot{y}_a, \dot{z}_a]^\top$ is the velocity of the Lidar system, i.e. the velocity of the aircraft which can be measured by airborne sensors. The Lidar wind measurements $\tilde{d} = [\tilde{w}_u, \tilde{w}_v, \tilde{w}_w]^\top$ will be used in the preview control design in the following chapter.

4.4 Control Design

In this section, we design the preview-based landing control system for the very flexible flying wing. As mentioned earlier, the aeroelastic and trajectory control system has been designed in Chapter 3 for this model to achieve efficient trajectory tracking in the presence of turbulence. We now adapt the control system to realize autonomous landing. The control structure of the landing control system is illustrated in Fig. 4.6, which follows the two-loop control scheme as proposed in Section 3.2 but the inner-loop control design is extended to include the Lidar preview wind measurements to benefit the landing scenario. The introduction of such preview knowledge enables the control system to act before the wind disturbance impact the aircraft, thus improves landing effectiveness and disturbance rejection performance. Here, we mention again that we choose the midpoint of the flying wing as reference point to track the aircraft flight dynamics, thus all the variables in the following context are defined/measured at this point.

In the longitudinal channel during landing, when the flying wing descends to the altitude of the final approach phase starting point H_0 (see Fig. 4.1), the outer-loop controller is connected to SG “glide control” (see Fig. 4.6), driving the aircraft to glide down in uniform linear motion at constant flight path angle, which is achieved by LADRC altitude control to track the desired altitude command. Once the flying wing descends to the altitude of the flare phase starting point H_1 , the outer-loop controller is then switched to SF “flare control”, driving the aircraft to gradually adjust its vertical speed and pitch angle to the desired range to guarantee safe touchdown, which is achieved by PI vertical speed control. The outer-loop LADRC controller (using altitude and vertical speed as feedback) and PI controller (using vertical speed as feedback) generate pitch angle command to the inner loop. We mention that to reduce the impact of gains during switch, the pitch angle command θ_{r2} at switch is used as the initial value of the integral term in the PI con-

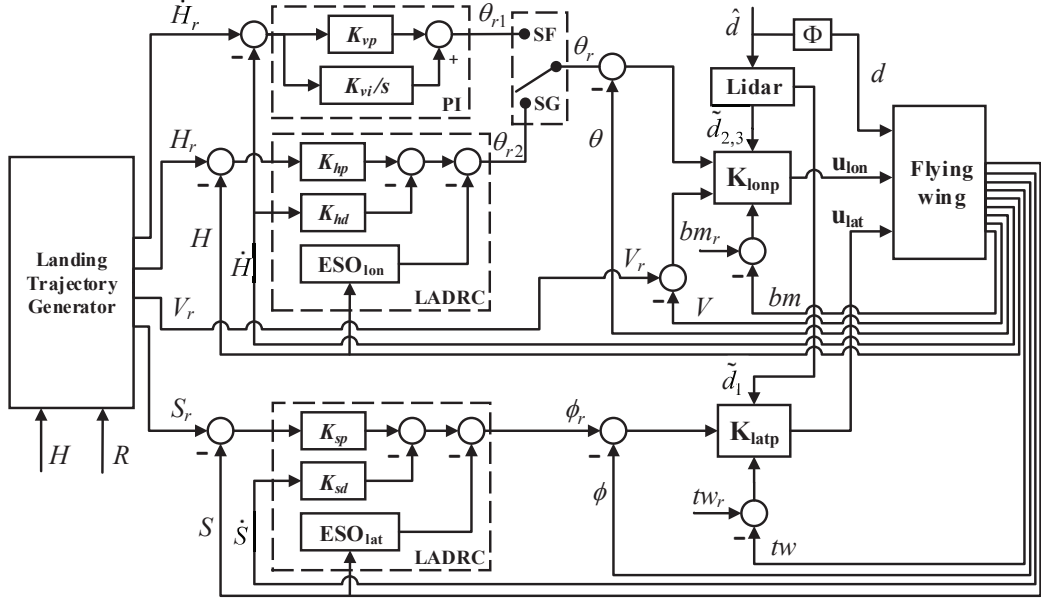


Figure 4.6: Structure of the preview-based landing control system: the upper part is for the longitudinal channel while the lower part is for the lateral channel. Output feedback signals are altitude H , lateral displacement S , forward velocity V , pitch angle θ , roll angle ϕ , root bending moment bm and twist moment tw . R is the travelling distance since entering the final approach phase. ESO_{lon} and ESO_{lat} are the extended state observers (ESO) in the outer-loop LADRC controller. \hat{d} is the actual wind disturbance at a distance in front of the aircraft, \tilde{d}_i is the Lidar wind measurements with the subscript $i = 1, 2, 3$ denotes the lateral, forward and vertical component, respectively. d is the wind disturbance that actually impact the aircraft, and Φ is the delay chain. K_{lonp} and K_{latp} are the H_∞ preview controllers in the longitudinal and lateral channel, respectively. The subscript symbol r denotes the reference command, while the \bullet symbol denotes time derivative. K_{hp} , K_{hd} , K_{sp} , K_{sd} , K_{vp} and K_{vi} are the corresponding controller parameters.

troller. The H_∞ preview controller is designed in the inner loop to generate control inputs (to the corresponding longitudinal flaps and thrust) to track this pitch angle command and maintain the forward velocity at its trim value simultaneously, using pitch angle, forward velocity and root bending moment as feedback. In addition, the forward and vertical components of the Lidar wind measurements are used by the H_∞ preview controller as prior knowledge to improve control performance in the longitudinal channel.

In the lateral channel, we need to control the flying wing to align with the center of the runway in both the final approach and flare phases, this is accomplished by zero lateral displacement control. Similarly, an outer-loop LADRC controller is used to generate roll angle command for the inner loop, using lateral displacement

and lateral speed as feedback. And an inner-loop H_∞ preview controller is employed to generate control inputs (to the corresponding lateral flaps and thrust) with roll angle and twist moment as feedback. Similarly, the lateral component of the Lidar wind measurements is used by the H_∞ preview controller as prior knowledge to improve control performance in the lateral channel.

4.4.1 Inner-Loop H_∞ Preview Control Design

We now design the inner-loop H_∞ preview controller. Different from conventional H_∞ control design, the preview control design requires augmenting the system plant with the preview information, which is the Lidar wind measurement in this work. We use a N -step delay chain to describe the time delay between the measurement of wind and its action on the aircraft. As the wind disturbance is assumed to travel with mean speed [145] from the measurement location to the aircraft, the N -step delay chain Φ for the three-dimensional wind disturbance is modelled as pure delay in the discrete-time state space description,

$$\begin{aligned} \mathbf{x}_d(k+1) &= \mathbf{A}_d \mathbf{x}_d(k) + \mathbf{B}_d \hat{\mathbf{d}}(k), \\ d(k) &= \mathbf{C}_d \mathbf{x}_d(k), \end{aligned} \tag{4.9}$$

where

$$\begin{aligned} \mathbf{A}_d &= \begin{bmatrix} 0 & \mathbf{I}_{l_d} & \cdots & 0 \\ \vdots & \vdots & \vdots & \vdots \\ 0 & 0 & \cdots & \mathbf{I}_{l_d} \\ 0 & 0 & \cdots & 0 \end{bmatrix}_{Nl_d \times Nl_d}, \quad \mathbf{B}_d = \begin{bmatrix} 0 \\ \mathbf{I}_{l_d} \end{bmatrix}, \\ \mathbf{C}_d &= \begin{bmatrix} \mathbf{I}_{l_d} & 0 \end{bmatrix}. \end{aligned}$$

Here $\hat{\mathbf{d}}$ is the wind disturbance at the measurement location while d is the wind disturbance that actually act on the aircraft. \mathbf{I}_{l_d} is an identity matrix with dimension l_d that of the previewable disturbance, and N is the preview length. We choose $N = 40$ in this paper, as a result of the two-second preview time with the controller sample rate of 0.05 seconds.

We then augment the discrete-time flying wing model (2.12) with the delay chain model (4.9) to incorporate the time delay between measurement of wind and

its action, which is expressed as

$$\begin{aligned} \begin{bmatrix} x(k+1) \\ x_d(k+1) \end{bmatrix} &= A_a \begin{bmatrix} x(k) \\ x_d(k) \end{bmatrix} + B_a \begin{bmatrix} \hat{d}(k) \\ u_c(k) \end{bmatrix}, \\ \begin{bmatrix} y(k) \\ \hat{d}(k) \end{bmatrix} &= C_a \begin{bmatrix} x(k) \\ x_d(k) \end{bmatrix} + D_a \begin{bmatrix} \hat{d}(k) \\ u_c(k) \end{bmatrix}, \end{aligned} \quad (4.10)$$

where

$$\begin{aligned} A_a &= \begin{bmatrix} A_f & B_{fw}C_d \\ 0 & A_d \end{bmatrix}, B_a = \begin{bmatrix} 0 & B_{fu} \\ B_d & 0 \end{bmatrix}, \\ C_a &= \begin{bmatrix} C_f & 0 \\ 0 & 0 \end{bmatrix}, D_a = \begin{bmatrix} 0 & 0 \\ I_{ld} & 0 \end{bmatrix}. \end{aligned}$$

Here A_f , B_{fu} , B_{fw} and C_f are the discrete-time linear state space matrices of the flying wing model as stated in Chapter 2. Note that the wind disturbance $\hat{d}(k)$ now can be regarded as an additional "system output" and be fed into the controller as preview (feedforward) information, which is essentially treated the same as other feedback signals in the H_∞ preview control design process.

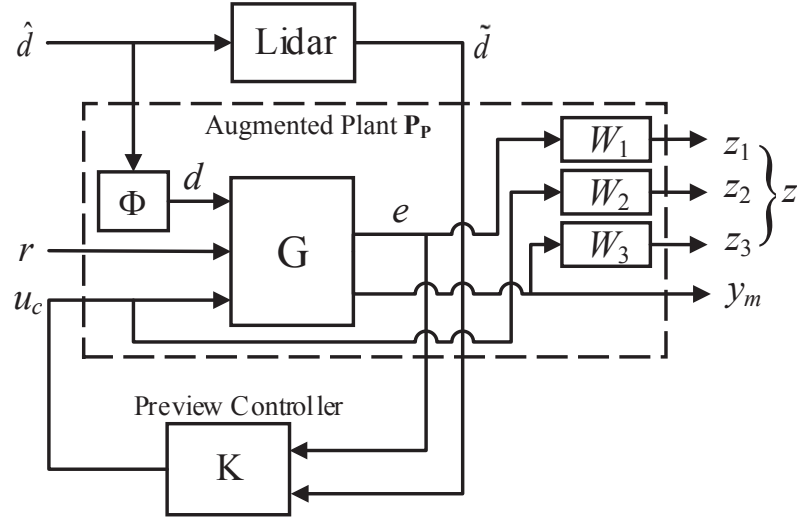


Figure 4.7: H_∞ tracking problem with Lidar preview. \hat{d} , \tilde{d} , d , r , u_c denote the wind disturbance in front of the aircraft, wind measurements from Lidar, the wind disturbance actually impact the aircraft, reference commands and control inputs, respectively. $z_{i=1,2,3}$ are the performance outputs, y_m is the measurement output. Φ is the N -step delay chain. G and K are the transfer functions of the plant and the preview controller.

As discussed in Section 3.2.1, the inner loop serves as an aeroelastic control loop for dynamic stabilization and gust load alleviation, and also acts to track the attitude angle command received from the outer loop. Thus, the control design is treated as an H_∞ tracking problem. The mixed sensitivity H_∞ synthesis method is employed, which introduces weighting functions to achieve both good disturbance rejection performance and tracking effectiveness, as shown in Fig. 4.7. The objective is to obtain a controller K which minimizes the H_∞ -norm of the transfer function from the future wind disturbance \hat{d} and inner-loop reference commands r to the weighted performance outputs z . Therefore, by augmenting system (4.10) with weighting functions (re-written in discrete-time state space description) for H_∞ preview control synthesis, we obtain the realization

$$\mathbf{P}_p = \left[\begin{array}{ccccc|ccc} A_{w1} & 0 & 0 & -B_{w1}C_f & 0 & 0 & B_{w1} & 0 \\ 0 & A_{w2} & 0 & 0 & 0 & 0 & 0 & B_{w2} \\ 0 & 0 & A_{w3} & B_{w3}C_f & 0 & 0 & 0 & 0 \\ 0 & 0 & 0 & A_f & B_{fw}C_d & 0 & 0 & B_{fu} \\ 0 & 0 & 0 & 0 & A_d & B_d & 0 & 0 \\ \hline C_{w1} & 0 & 0 & -D_{w1}C_f & 0 & 0 & D_{w1} & 0 \\ 0 & C_{w2} & 0 & 0 & 0 & 0 & 0 & D_{w2} \\ 0 & 0 & C_{w3} & D_{w3}C_f & 0 & 0 & 0 & 0 \\ \hline 0 & 0 & 0 & -C_f & 0 & 0 & I_r & 0 \\ \hline 0 & 0 & 0 & 0 & 0 & I_{l_d} & 0 & 0 \end{array} \right], \quad (4.11)$$

where $(A_{wi}, B_{wi}, C_{wi}, D_{wi})$ are the discrete-time state space matrices of the weighting functions $W_{i=1,2,3}$, I_r is an identity matrix with dimension that of the reference commands. The realization \mathbf{P}_p is then used as the basis to synthesize the inner-loop H_∞ preview controller.

Discrete-time H_∞ Synthesis

As described above, the preview-based mixed sensitivity H_∞ tracking problem is formulated as in (4.11) in the discrete-time domain. To synthesize the H_∞ preview controller, a brutal method is to convert the discrete-time formulation into the continuous domain and use the *hinfsyn* command provided in Matlab[®] to solve the continuous-time controller, which will then be converted back to the discrete-time

domain to eventually obtain the discrete-time H_∞ preview controller. However, it is worth noting that the N -step delay chain is a pure time delay which can only be approximated via certain approximation methods (for example, the Padé approximation formulas [146]) to deal with time delays in the continuous domain, resulting in a non-optimal solution. Hence, to avoid such issues, we solve the preview controller based on the discrete-time H_∞ synthesis theory proposed in [142] which provides the accurate solution. Two discrete-time algebraic Riccati equations (DARE) regarding the Full Information (FI) control problem and Output Feedback (OF) control problem for system $\mathbf{P_P}$ are solved to derive the H_∞ preview controller.

The FI control problem is formulated as

$$P_{FI} = \left[\begin{array}{c|c|c} A_p & B_{p1} & B_{p2} \\ \hline C_{p1} & D_{p11} & D_{p12} \\ \hline I_r & 0 & 0 \\ \hline 0 & I_{ld} & 0 \end{array} \right], \quad (4.12)$$

in which $A_p, B_{p1}, B_{p2}, C_{p1}, D_{p11}$ and D_{p12} conform with the partitions in (4.11). We derive the non-negative, stabilizing, feasible solution X_{FI} to the FI discrete-time algebraic Riccati equation

$$X_{FI} = A_p^\top X_{FI} A_p + Q_{FI} - L_{FI}^\top (R_{FI} + B_p^\top X_{FI} B_p)^{-1} L_{FI},$$

such that the objective H_∞ norm for the FI control problem is less than a given value γ with the stabilising controller derived by $K_{FI} = -\bar{R}_3^{-1}[\bar{L}_2 \ \bar{R}_2]$. Here, $Q_{FI} = C_{p1}^\top C_{p1}$, $B_p = [B_{p1} \ B_{p2}]$, $L_{FI} = [D_{p11} \ D_{p12}]^\top C_{p1} + B_p^\top X_{FI} A_p \triangleq \begin{bmatrix} \bar{L}_1 \\ \bar{L}_2 \end{bmatrix}$ and

$$R_{FI} = \begin{bmatrix} D_{p11}^\top D_{p11} - \gamma^2 I & D_{p11}^\top D_{p12} \\ D_{p12}^\top D_{p11} & D_{p12}^\top D_{p12} \end{bmatrix} \triangleq \begin{bmatrix} \bar{R}_1 & \bar{R}_2^\top \\ \bar{R}_2 & \bar{R}_3 \end{bmatrix}.$$

Furthermore, the OF control problem is formulated as

$$P_{OF} = \left[\begin{array}{c|c|c} A_p & B_{p1} & B_{p2} \\ \hline C_{p1} & D_{p11} & D_{p12} \\ \hline C_{p2} & D_{p21} & 0 \end{array} \right], \quad (4.13)$$

in which C_{p2} and D_{p21} conform with the partitions including both the feedback and preview channels in (4.11). Similarly, we derive the non-negative, stabilizing, feasible solution Y_{OF} to the OF discrete-time algebraic Riccati equation

$$Y_{OF} = A_p Y_{OF} A_p^\top + Q_{OF} - L_{OF} (R_{OF} + C_p Y_{OF} C_p^\top)^{-1} L_{OF}^\top,$$

such that the corresponding H_∞ norm for the H_∞ control problem is less than γ and $\rho(X_{FI} Y_{OF}) < \gamma^2$ where $\rho(\cdot)$ denotes the spectral radius. Here, $Q_{OF} = B_{p1} B_{p1}^\top$, $C_p = [C_{p1}^\top \ C_{p2}^\top]^\top$, $L_{OF} = B_{p1} [D_{p11}^\top \ D_{p21}^\top] + A_p Y_{OF} C_p^\top$ and $R_{OF} = \begin{bmatrix} D_{p11} D_{p11}^\top - \gamma^2 I & D_{p11} D_{p21}^\top \\ D_{p21} D_{p11}^\top & D_{p21} D_{p21}^\top \end{bmatrix}$.

The discrete-time H_∞ preview controller is derived as a function of the two DARE solutions and the plant realization, which is $K = f(\mathbf{P}_P, X_{FI}, Y_{OF})$. We refer to [142] for more detailed formulations and discussions. The dimension of the derived discrete-time H_∞ preview controller is equal to the dimension of the augmented plant (4.11). Thus, although it is not the case in this work, it is important to mention that when the preview length N is very large, using the above standard synthesis method is time-consuming and may even fail to obtain a solution. Instead, an efficient algorithm was proposed by Hazell and Limebeer in [147] which provides a better solution to synthesize the discrete-time H_∞ preview control problem with large preview dimension.

Note that the wind measurements \tilde{d} from the Lidar system instead of the ideal wind disturbance \hat{d} are actually provided to the preview controller as input to make it more realistic, as shown in Fig. 4.7. It is also necessary to mention that, as stated in [132, 148], the preview controller is essentially the combination of a feedforward controller and a feedback controller, which means

$$K = K_{fb}e + K_{ff}\tilde{d}, \quad (4.14)$$

but both parts are designed simultaneously with guaranteed robustness (by minimising the H_∞ -norm of the transfer function from the future disturbance and the reference command to the performance output). In (4.14), \tilde{d} is the vector of Lidar wind measurements at each preview step, K_{fb} and K_{ff} denote the feedback loop controller and the feedforward loop controller, respectively. As a feedforward loop, the preview action does not affect the stability of the closed-loop system, while the closed-loop stability is ensured by H_∞ control synthesis. In this work, although the Lidar system is used to provide such preview information, it can be essentially

regarded as a low-pass filter embedded in the feedforward loop, the closed-loop stability is still guaranteed since the feedback loop is independent of the Lidar system.

In order to enhance the robust performance and simultaneously achieve good tracking effectiveness, the simulation-based PSO (Particle Swarm Optimization) algorithm is again employed to optimize the parameters of the corresponding weighting functions, based on the discrete-time equivalence of the reduced-order nonlinear model (2.10). We refer to Section 3.2.1 for more details. Similarly, since the linear model (2.12) is decoupled in the longitudinal channel and lateral channel, the H_∞ preview controller can be synthesized separately, which are denoted by K_{lonp} and K_{latp} , respectively, as shown in Fig. 4.6.

4.4.2 Outer-loop Control Design

As discussed earlier, the outer loop is designed to generate attitude angle commands for the inner loop. Here, we use the same outer-loop controllers (3.4), (3.5) and (3.9) that are developed in Section 3.2.2. In the longitudinal channel, the LADRC altitude controller (3.5) is used to control the aircraft to glide down at constant flight path angle in the final approach phase, while the PI vertical speed controller (3.4) is used to control the aircraft to gradually adjust its vertical speed and pitch angle to the desired range in the flare phase to guarantee safe touchdown. In the lateral channel, the LADRC lateral displacement controller (3.9) is used to control the aircraft to align with the center of the runway in both the final approach and flare phases. Please refer to Section 3.2.2 for more details on the design of these outer-loop controllers.

4.5 Simulation Results

In this section, we conduct simulation tests based on the full-order nonlinear aeroelastic model (2.4) to check the performance of the designed preview-based landing control system. As in Chapter 3, the 4th-order Runge-Kutta solver *ode45* in Matlab[®] is used in the nonlinear simulations, and the control inputs are updated at the frequency of 20Hz. All the control actuators are modelled as first-order lag systems with time constants of 0.3 seconds and the operating range of -100N~200N for thrust and $\pm 20^\circ$ for flap deflections (negative thrust are assumed to be available to act as air brakes to increase drag and reduce speed). Details on the configurations of the very flexible flying wing model can be found in Section 2.4.

4.5.1 Robustness against Modeling Uncertainties

This subsection demonstrates the robust performance of the inner-loop H_∞ preview controller with respect to modelling uncertainties. Taking the longitudinal inner-loop as an example, we conduct simulations on the full-order nonlinear models (2.4) with varying bending stiffness EI_2 , namely the "more" ($0.9EI_2$), "regular" ($1.0EI_2$) and "less" ($1.1EI_2$) flexible wings. The same H_∞ preview controller K_{lonp} designed based on the "regular" very flexible configuration is used in these three simulation cases. We mention that the difficulty of the control design to stabilize the aircraft is largely dependent on its airframe flexibility. The "regular" flexible configuration already represents a highly flexible wing which is very difficult to stabilize, while the "more" flexible configuration represents a much more difficult case and the "less" flexible configuration represents a less difficult one.

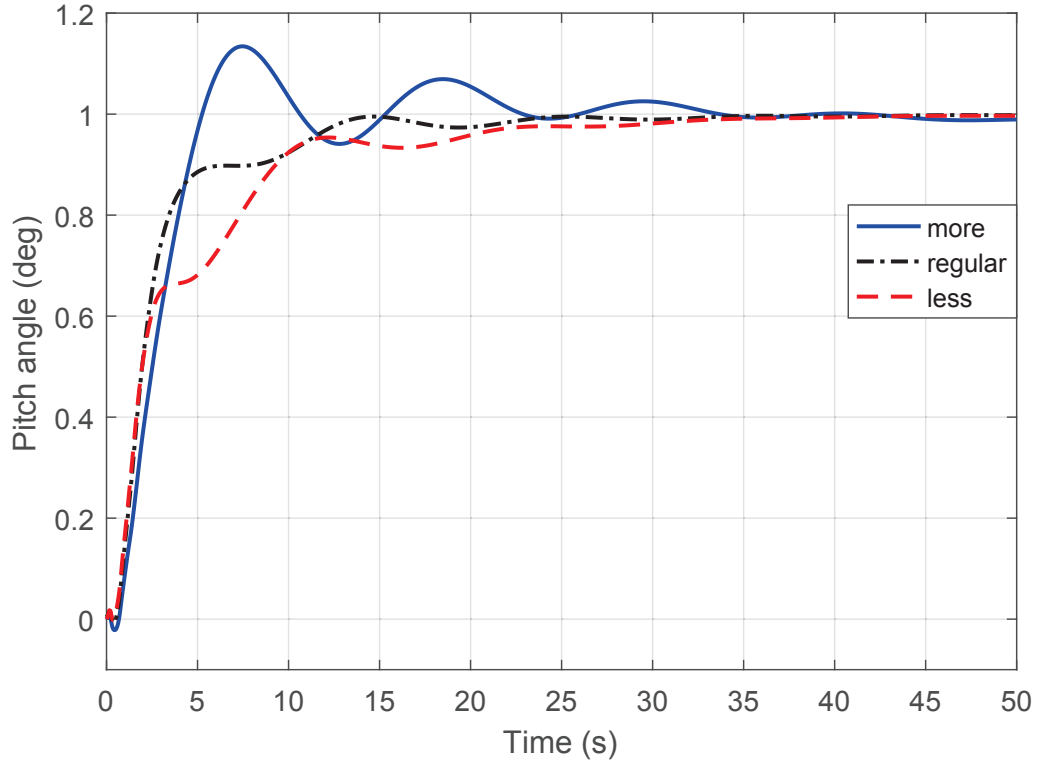


Figure 4.8: Pitch responses of the preview control system based on three types of very flexible configurations with varying bending stiffness.

The corresponding step responses of the pitch angle are shown in Fig. 4.8, where one can see that the control system succeeds to track the pitch angle command with satisfactory performance in all three cases. Overshoot is observed in the "more" flexible configuration due to increased flexibility, while a slower response

is observed in the "less" flexible configuration due to increased stiffness, compared to the response of the "regular" configuration. Considering the baseline stiffness ($1.0EI_2$) is notably small, the differences between the three responses in Fig. 4.8 are essentially small, which indicates the good robustness of the designed inner-loop H_∞ preview controller against modelling uncertainties.

4.5.2 Lidar Wind Measurement

This subsection shows the simulation results of the three-dimensional wind measurements using the Lidar simulator developed in Section 4.3. We generate the continuous three-dimensional turbulent wind field using windSim simulator [149] in Matlab[®] (based on von Kármán velocity spectra). The turbulence scale length and intensity at low altitudes are defined as [150],

$$\begin{cases} L_w = h_{ref}, \\ L_u = L_v = \frac{h_{ref}}{(0.177 + 0.000823h)^{1.2}}, \\ \sigma_w = 0.1w_{20}, \\ \sigma_u = \sigma_v = \frac{\sigma_w}{(0.177 + 0.000823h)^{0.4}}, \end{cases}$$

where $L_{u,v,w}$ are the scale lengths and $\sigma_{u,v,w}$ are the turbulence intensities in the lateral, forward and vertical direction, respectively. h_{ref} is altitude (in feet) and w_{20} is the wind speed at 6 meters. We mention that there are better turbulence models at low altitudes, but the von Kármán model is good enough for test purpose.

Fig. 4.9 shows the sample series of the synthetic turbulence and the corresponding Lidar wind measurements. The turbulence length and intensity are set to be $L_w = 5m, L_u = L_v = 38.85m$ and $\sigma_w = 0.5m/s, \sigma_u = \sigma_v = 1m/s$, respectively. The blue solid line indicates the synthetic wind turbulence while the red dashed line indicates the Lidar measurements. The Lidar wind measurements are time-shifted by two seconds (which is consistent with preview length) to align with the synthetic wind turbulence. It is clear that the Lidar measurements well capture the low frequency components of the wind turbulences, which is due to the low-pass filtering property of the spatial weighting in line-of-sight measurement. Note that in the following simulations, the actual (synthetic) wind turbulence will be applied to the aircraft while the Lidar wind measurements will be provided to the control system as preview information.

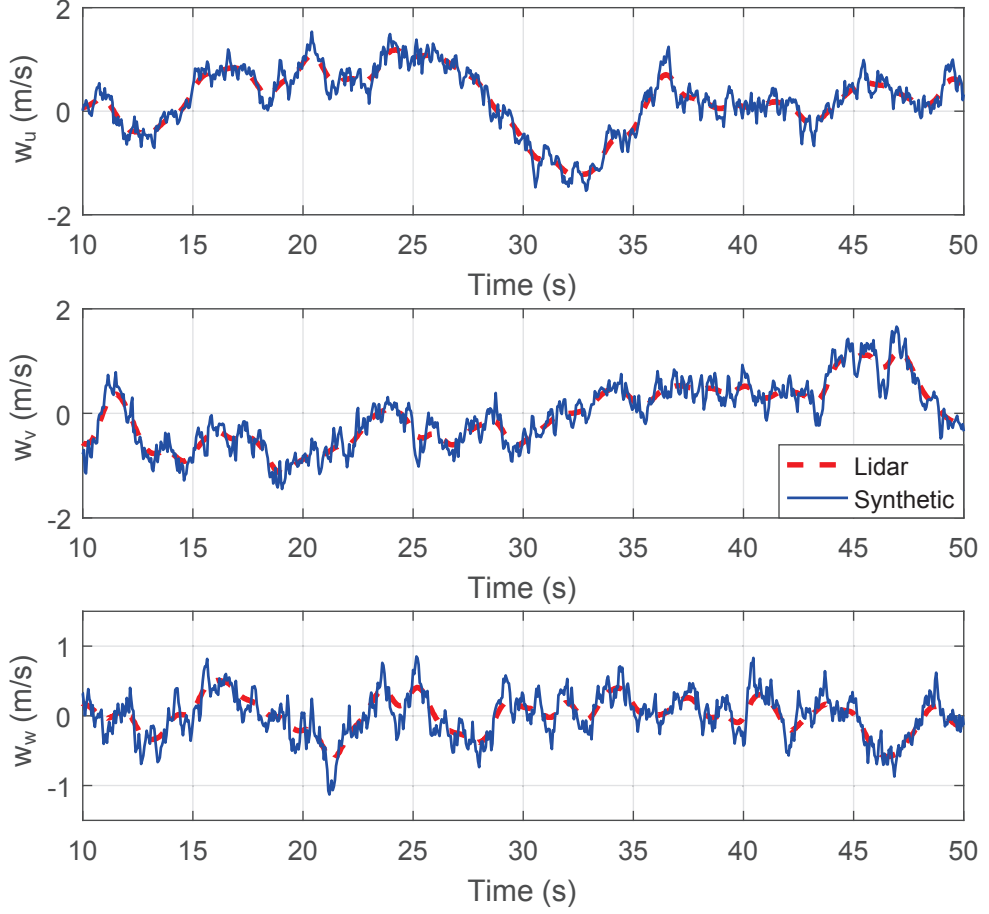


Figure 4.9: Sample series of the three-dimensional synthetic turbulence at $h = 5m$ with $w_{20} = 5m/s$ and the corresponding Lidar wind measurements. w_u, w_v, w_w denote the lateral, forward and vertical component of the wind disturbance, respectively.

4.5.3 Wind Turbulence Response

We assume that the altitudes of the final approach phase starting point and flare phase starting point are $H_0 = 40m$ and $H_1 = 15m$ (see Fig. 4.1), respectively. The desired vertical speed at touchdown point is $v_{zr} = -0.1m/s$ and the flying wing is assumed to have an initial lateral deviation of $2m$. In the final approach phase, the descent flight path angle (glide ratio) is determined by the lift-to-drag (L/D) ratio. In our case, the lift-to-drag ratio is about 56 for the very flexible flying wing model (2.4). Therefore, the desired descent flight path angle $\gamma_L = -atan(D/L) \approx -1^\circ$ is obtained.

Now we test the performance of the preview-based landing control system in the presence of wind turbulence. The excitation used here is the three-dimensional

synthetic von Kármán turbulence generated in Section 4.5.2, of which the lateral component is also added with a constant lateral wind of 1m/s . The turbulence is applied all the way to the touchdown. The responses of the flying wing with the preview-based landing control system are shown in Fig. 4.10 - Fig. 4.12, compared to those of the baseline non-preview landing control system (which is adapted from the aeroelastic and trajectory control system developed in Chapter 3). It is clear from Fig. 4.10 that both landing control systems could drive the flying wing to align with the center of the runway and land successfully.

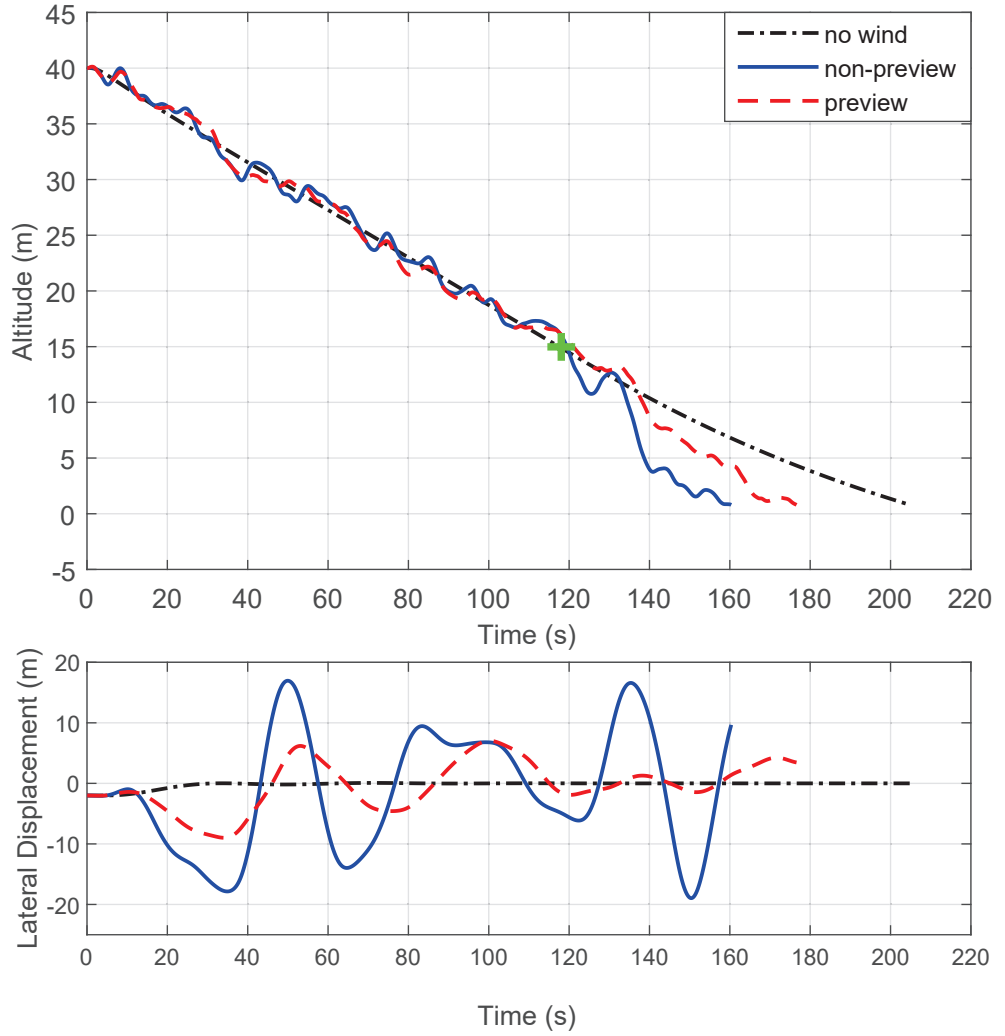


Figure 4.10: Time histories of the landing trajectories with the preview-based and non-preview landing control systems in the presence of three-dimensional turbulence. The green cross symbol denotes the flare phase starting point. The altitude response without wind turbulence is also plotted in the top diagram.

In the top diagram of Fig. 4.10, the black dash-dotted line represents the reference landing trajectory without wind disturbance, while the blue solid line and the red dashed line represents the actual landing trajectory with the baseline control system (without preview) and the preview control system in the presence of wind disturbance, respectively. In the final approach phase (0~118 seconds), both control systems succeed to direct the aircraft to follow the descent path via tracking the desired altitude command. In the flare phase, since vertical speed control instead of altitude control is employed to ensure the aircraft achieves appropriate touch down speed and pitch angle at the loss of touch down effectiveness (please refer to Section 4.2), there exist deviations of the touchdown point in the presence of wind turbulence, compared to the case without turbulence. However, the deviation of the touchdown point and lateral displacement with the preview control system are smaller than the case without preview, which demonstrates the benefit of using Lidar wind measurements as preview information to improve control performance.

From Fig. 4.10 and Fig. 4.11, we can also see that oscillations in both the longitudinal and lateral variables are all reduced by the preview-based landing control system. The deviations in the lateral displacement, vertical speed, pitch angle, roll angle and yaw angle are significantly reduced by 58%, 28%, 45%, 68% and 71% in the root-mean-square (RMS) metrics, respectively, compared to those of the baseline non-preview controller. The bottom two diagrams in Fig. 4.11 depict the corresponding wing tip displacements relative to the center of the aircraft, which indicate smaller wing deformations with the preview control system. All these results show that the preview-based landing control system has achieved better landing effectiveness and disturbance rejection performance, which is able to realize more efficient and safer autonomous landing in the presence of wind turbulence. The corresponding control actions are plotted in Fig. 4.12, where one can see that the control actions of the preview control system are smaller than those of the baseline non-preview controller. This is because by using Lidar wind measurements as prior knowledge, the preview control system can act before the wind disturbance actually affect the aircraft, thus requiring less control efforts to adjust itself to a proper state in advance to reduce the impact of the incoming disturbance on flight dynamics. Note that the negative thrust required in the simultaneous thrust indicates that airbrakes are needed to actively increase drag during landing (but not considered here).

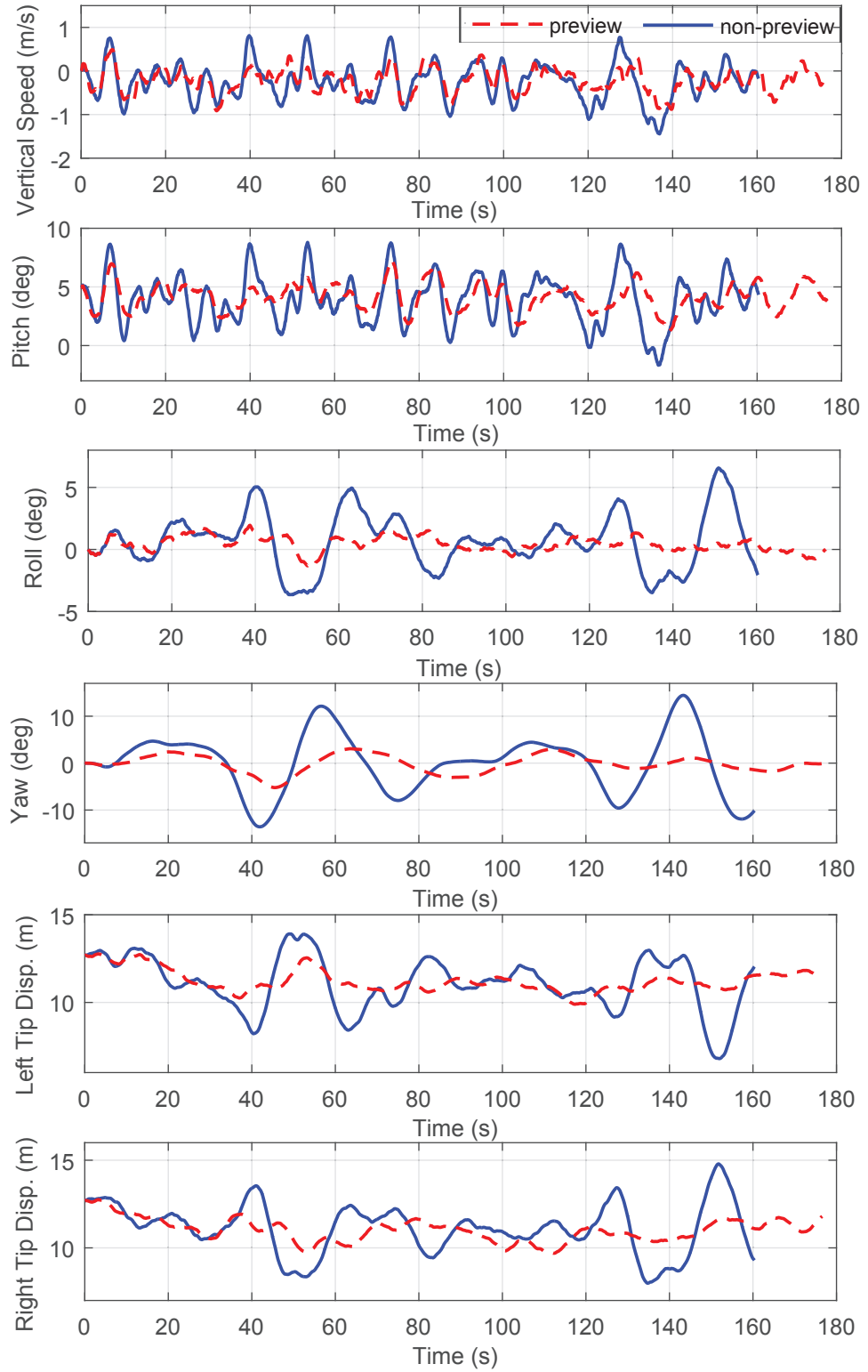


Figure 4.11: Time histories of the aircraft responses by the preview-based control system with measurement noise in the Lidar system.

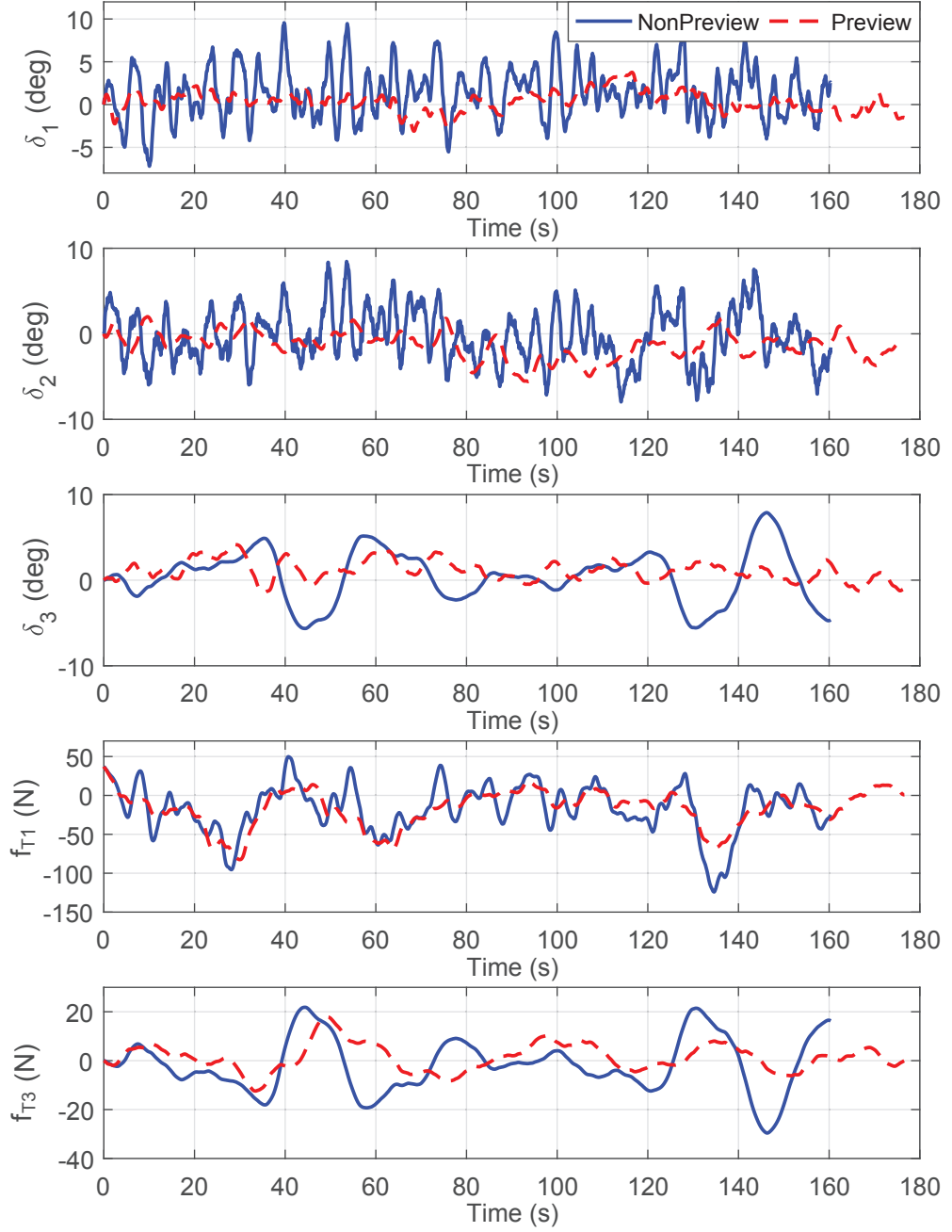


Figure 4.12: Time histories of the control actions by the preview-based control system with measurement noise in the Lidar system.

Furthermore, we illustrate the consistent trajectory of the center of gravity (cg) and those of the center of the wing (cw) in Fig. 4.13, which indicates that the disturbance does not excite any vibration mode that would affect the approximation of the rigid-body motions.

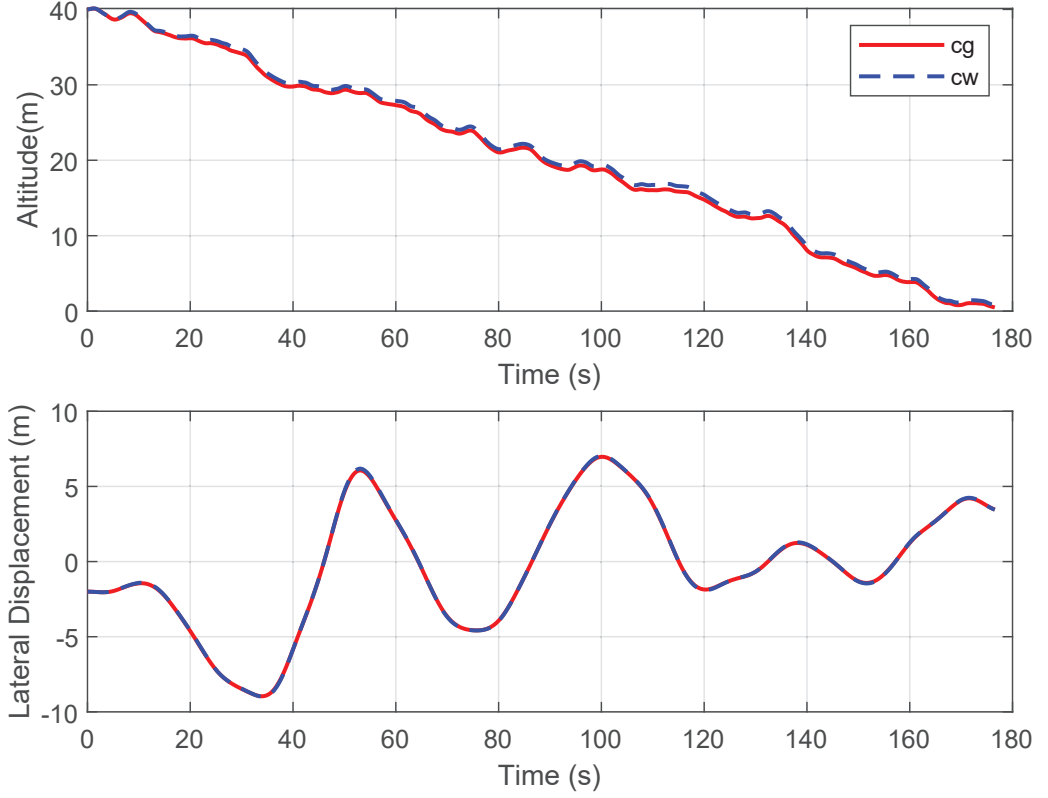


Figure 4.13: Trajectories of the center of gravity (cg) and the center of the flying wing (cw) during landing.

4.5.4 Modal Analysis

A major advantage of the aeroelastic formulation (2.4) is that the modal contributions are used as primary variables and can be easily analysed. In this subsection, we identify the contributions of the dominant modes to the observed dynamics in the above simulations, which are summarized in Table 4.1. Results with and without preview are both included. In Table 4.1, the third and fourth column show the modal energy ($\frac{1}{2}q_{ij}^2$, with $i=1$ for kinetic energy and $i=2$ for strain energy of mode j) relative to the trim condition of the dominant modes, while the last two column

show the degrees of reduction level in modal energy by the preview control approach with respect to the baseline non-preview case. Table 4.1 reveals that the RMS deviations of the modal amplitudes of the rigid-body modes and the dominant flexible modes were all reduced (except Mode 13) at different degrees by preview control. In addition, an example of the modal amplitudes of the first symmetric out-of-plane bending mode (q_{17}) is shown in Fig. 4.14 to illustrate the improvements by preview control.

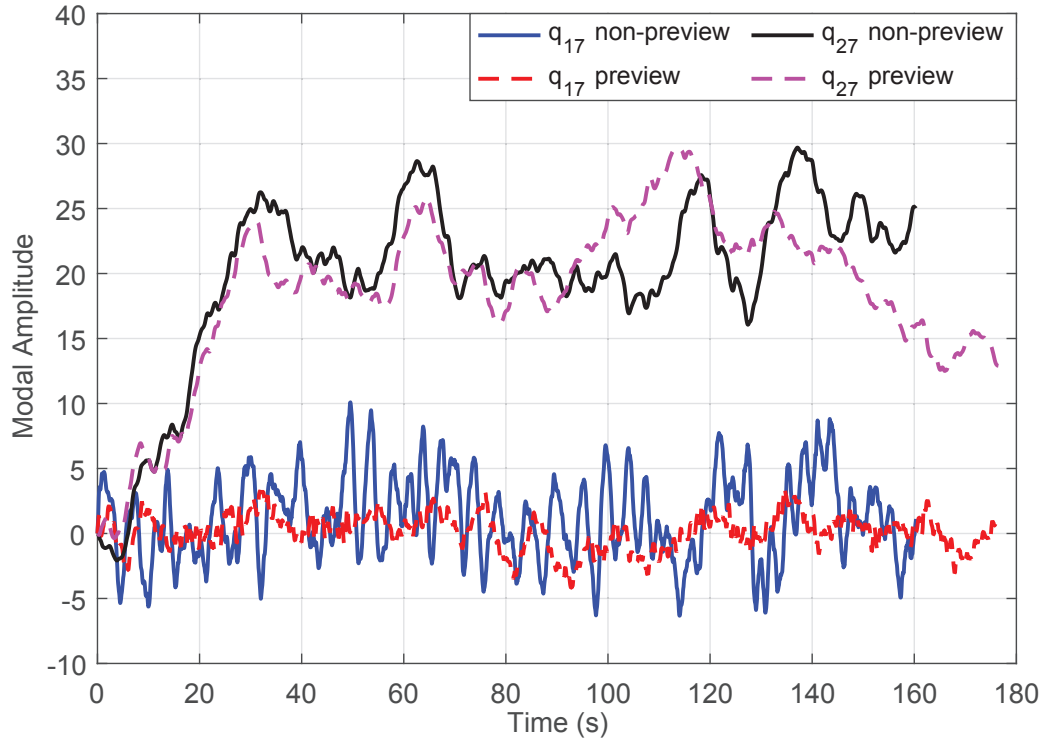


Figure 4.14: Modal amplitudes of the first symmetric out-of-plane bending mode with and without preview-based landing control systems in the landing simulations.

Table 4.1: Modal energy contributions and degrees of performance improvements by preview control.

Mode No.	Mode Type	q_{1j} no-preview	q_{2j} no-preview	q_{1j} preview	q_{2j} preview
1	Lateral translation	5.5×10^5	-	75%	-
2	Forward translation	4.9×10^5	-	38%	-
3	Vertical translation	2.3×10^4	-	11%	-
4	Pitch rotation	7.2×10^3	-	49%	-
5	roll rotation	3.3×10^4	-	65%	-
6	yaw rotation	2.3×10^5	-	77%	-
7	1st sym. out-of-plane bending	1.9×10^4	7.1×10^5	58%	15%
8	1st asym. out-of-plane bending	1.0×10^3	6.1×10^4	21%	4%
9	1st sym. in-plane bending (Type 1)	5.9×10^3	1.9×10^3	52%	57%
10	1st asym. in-plane bending (Type 1)	1.7×10^2	5.8×10^3	53%	60%
11	2nd sym. out-of-plane bending	9.7×10^2	3.3×10^3	22%	11%
12	1st sym. in-plane bending (Type 2)	2.5×10^2	7.7×10^3	40%	60%
13	2nd asym. out-of-plane bending	1.2×10^2	9.7×10^3	0%	0%
14	3rd sym. out-of-plane bending	3.1×10^2	1.4×10^3	26%	7%
15	1st asym. in-plane bending (Type 2)	2.5×10^1	1.5×10^3	49%	40%
16	1st sym. in-plane bending (Type 3)	2.5×10^1	2.9×10^3	38%	64%
17	3rd asym. out-of-plane bending	1.7×10^1	1.0×10^3	6%	4%

4.5.5 Measurement Noise Analysis

In the above simulations, accurate measurements of the wind velocities are assumed. Now we test the performance of the preview-based landing control system with measurement noise in the Lidar system. The setting up of the simulation case in Section 4.5.3 is considered here with two setups of Gaussian white noise added to the Lidar measurement outputs (see the top subfigure in Fig. 4.15) which have the signal-to-noise ratios (SNR) of 15dB and 5dB, respectively. The two sets of noisy measurement outputs are then provided to the preview controller as prior information, respectively. The responses of the flying wing are depicted in Fig. 4.15 and Fig. 4.16, compared to those using ideal Lidar wind measurement (i.e. no noise in the output measurement), while the corresponding control inputs are depicted in Fig. 4.17.

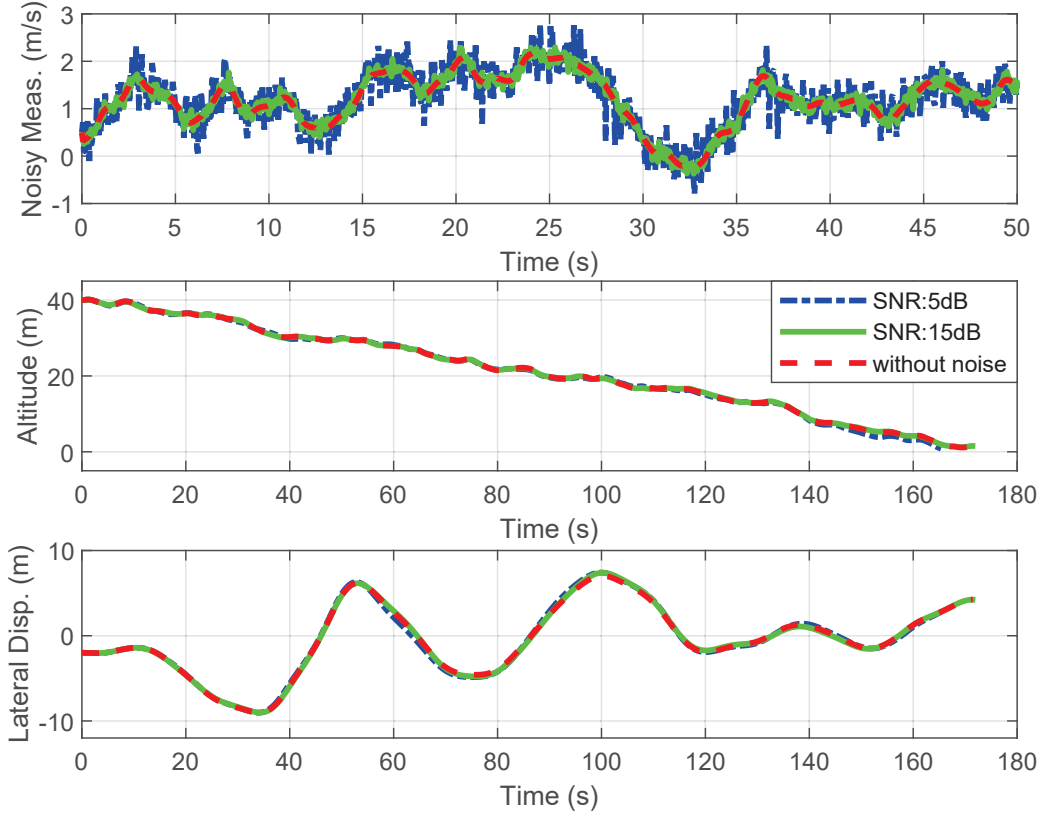


Figure 4.15: Time histories of the aircraft responses using noisy Lidar wind measurements as prior information to the preview control system. In the top diagram, only the first 50 seconds of the Lidar wind measurements of the non-stationary crosswind are plotted for better view of the measurement noises.

We can see that the responses of the aircraft in the case of $\text{SNR} = 15\text{dB}$

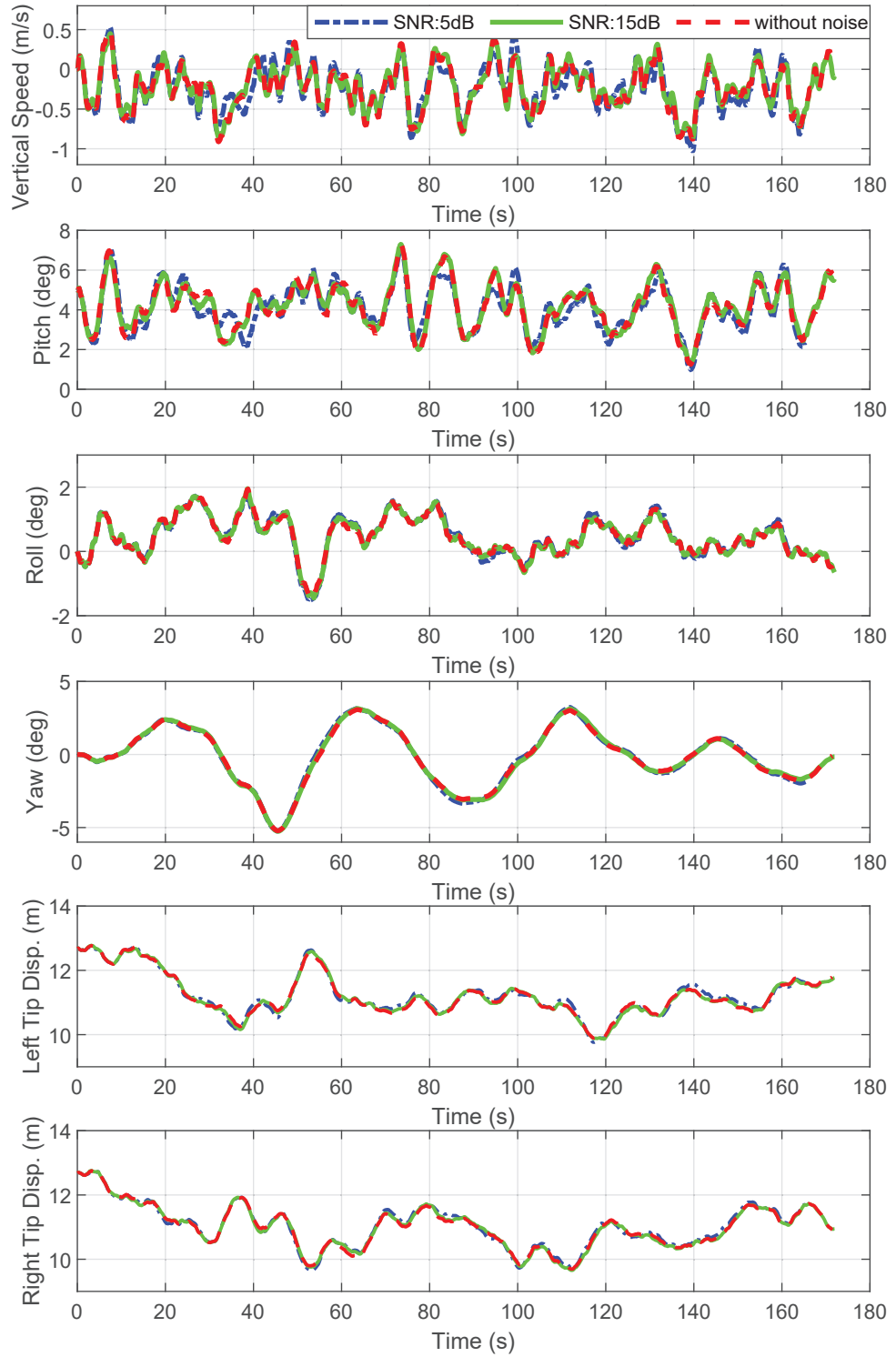


Figure 4.16: Time histories of the aircraft responses with the preview-based and non-preview landing control systems in the presence of wind turbulence.

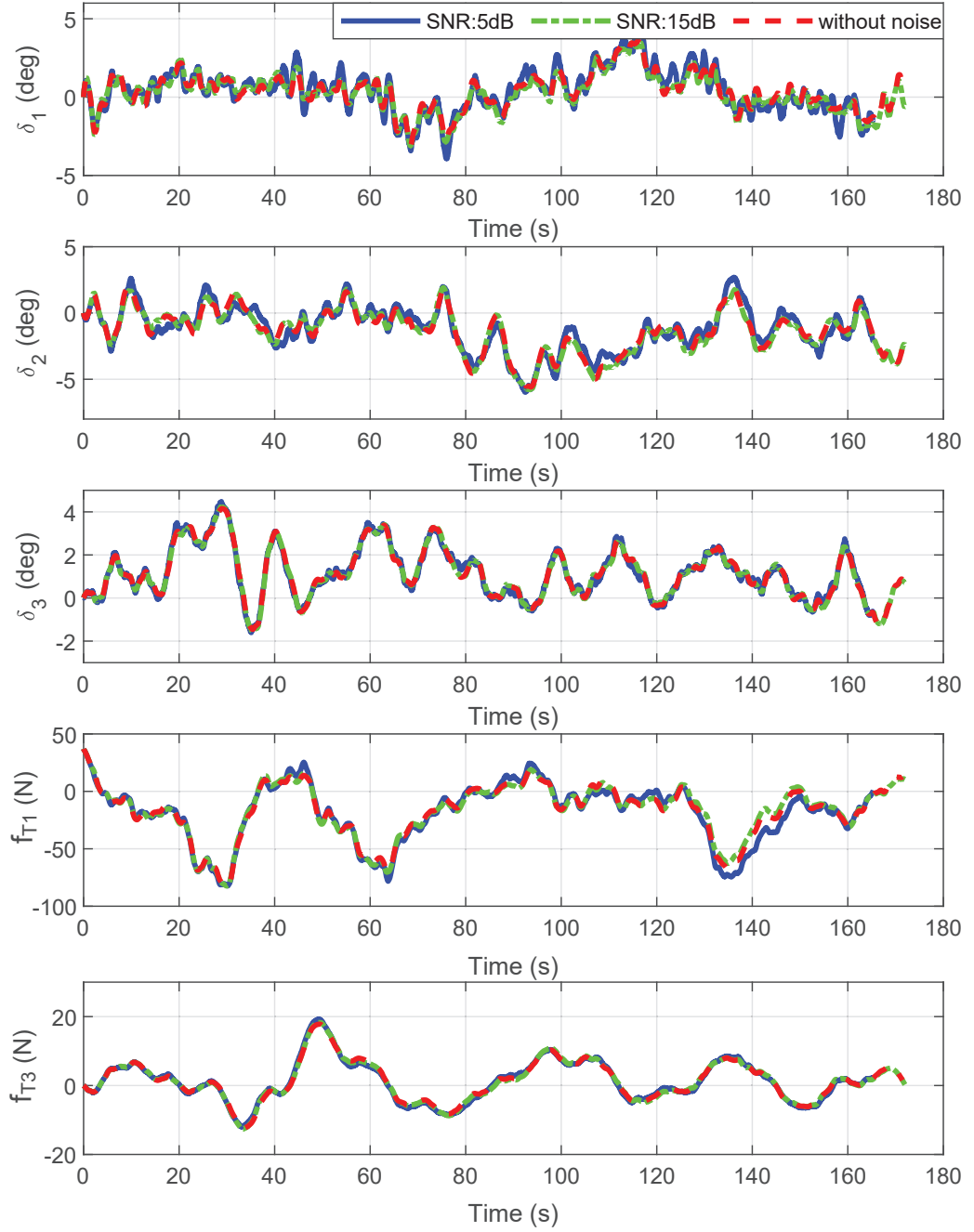


Figure 4.17: Time histories of the control actions with the preview-based and non-preview landing control systems in the presence of wind turbulence.

remain almost the same comparing to those using ideal measurements, while very small deviations are observed in the case of $\text{SNR} = 5\text{dB}$. The overall performance of the preview control system barely degrades by the noisy measurements, which indicate good robustness of the preview control system with respect to preview measurement errors.

4.6 Conclusions

A preview-based autonomous landing control system using a two-loop PI/LADRC and H_∞ preview control scheme has been proposed for a very flexible flying wing model. A Lidar (light detection and ranging) simulator was developed to measure the wind disturbance at a distance in front of the aircraft, which were provided to the H_∞ preview controller as prior knowledge to improve control performance. Simulation tests conducted based on the full-order nonlinear model (2.4) showed that the preview-based landing control system was able to land the aircraft safely, and also achieved better landing effectiveness and disturbance rejection performance than the baseline landing control system (without preview). It was shown that the preview control system also achieved good robustness with respect to measurement errors of the preview information. These results have demonstrated the potential of using short range Lidar wind measurements to benefit the autonomous landing of very flexible aircraft in the presence of wind turbulence. It should be noted that this work basically intended to investigate the applicability of preview control scheme to improving landing performance for very flexible aircraft, without considering the practical implementations of the Lidar system. Moreover, the spatial velocity fluctuations of wind turbulence was assumed to be small along the airframe, it is also necessary to investigate the applicability of the proposed method under wind turbulence with large spatial velocity fluctuations in future studies. The proposed method is not confined to the landing scenario but can be extended to benefit trajectory tracking problems.

Chapter 5

Data-driven Flight Control

In the previous two chapters, the flight control systems are both designed using conventional model-based H_∞ control methods, for which a significant amount of efforts have to be first devoted to obtaining an appropriate mathematical model of the very flexible flying wing. However, the issues of modelling uncertainties and unmodeled dynamics are inevitable due to the complex system dynamics of the very flexible aircraft (VFA), and the model order reduction to obtain a reduced-order design model further introduces modelling uncertainties. The controllers designed based on an inaccurate model may result in performance degrade and robustness issues when connected to the practical system. In this chapter, we investigate the data-driven flight control for the very flexible flying wing, by directly using the system input/output (I/O) data for control synthesis to reduce its dependence on explicit system modelling and thus avoid the issues of modelling uncertainties and unmodeled dynamics. The data-driven Model-Free Adaptive Control (MFAC) scheme is employed for this purpose. A cascaded proportional-derivative Model-Free Adaptive Control (PD-MFAC) approach is proposed to accommodate the MFAC scheme in a flight control problem, which shows better control performance over the original MFAC algorithm. Based on the PD-MFAC approach, the data-driven flight control system is developed to achieve gust load alleviation and path-following in three dimensions, with a guidance system designed to generate the corresponding path-following commands to track both the straight-line and curved paths. Simulations are conducted on the nonlinear aeroservoelastic model (2.4) to demonstrate the performance of the data-driven flight control system, compared to a baseline H_∞ flight control system adapted from Chapter 3.

5.1 Introduction

As discussed previously, the flight control of VFA mainly includes the aeroelastic control for gust load alleviation and the trajectory control for path following [21, 68, 79, 95]. By far, almost all the flight control systems are designed using various types of linear or nonlinear model-based control methods [27, 66, 68, 72, 79, 101, 102, 127, 151, 152], such as H_∞ control, linear quadratic control, dynamic inversion control, model predictive control, etc. For conventional model-based control methods, the control design is typically based on a mathematical model of the plant, which is obtained by either first-principles modeling or system identification techniques, with the faith that it represents the practical system. However, the obtained mathematical model is only an approximation of the practical system, modelling uncertainties and unmodeled dynamics always exist in the modelling process. Thus, the performance and reliability of the control system designed based on an inaccurate model may be largely affected [153]. This situation is especially serious for VFA. Despite the fact that the existing modelling frameworks for VFA are able to capture their dominant characteristics, the issues of modelling uncertainties and unmodeled dynamics are inevitable and undoubtedly more severe due to their highly complex system dynamics. Moreover, the mathematical model of VFA usually contains a large number of states [19] to describe the nonlinear aeroelastic effects, which makes it unsuitable for direct control synthesis. Therefore, one needs to reduce the model order first and design the control system based on the obtained reduced-order model, which further introduces modelling errors and uncertainties in the control design. All these factors will lead to possible performance degrade or even unstable response of the closed-loop system when employing conventional model-based control methods for flight control of VFA in practice. Hence, it is of great significance to design a flight control system which can overcome these disadvantages. In this regard, the data-driven control approach may provide better solutions.

As defined in [154], data-driven control includes “control theories and methods in which the controller is designed by directly using on-line or off-line input/output (I/O) data of the controlled system or knowledge from the data processing but not any explicit information of the mathematical model of the controlled process”. The contribution of this chapter is to investigate the flight control for VFA using data-driven control methods to overcome the aforementioned issues of conventional model-based control methods. Among the existing data-driven control schemes [154], the Model-Free Adaptive Control (MFAC) approach proposed by Hou [155] has developed into a systematic framework and shown rather satisfactory

control performance in dealing with nonlinear systems without the need of establishing a mathematical model of the system plant. The MFAC methods therefore have been successfully applied in many industrial fields [156]. The essential idea of the MFAC approach is to build an online data model of the nonlinear system based on the dynamic linearisation technique with a novel concept called pseudo partial derivative (PPD), which is estimated and updated online at each time step using only the history I/O data of the controlled plant. The adaptive control law is then derived from a weighted one-step-ahead prediction error cost function. In this fashion, the dependence of control design on explicit system modelling is significantly reduced in the MFAC approach, which avoids the inherent issues of conventional model-based control methods concerning unmodelled dynamics and modelling uncertainties, thereby improving the controller’s effectiveness and robustness. It is important to mention that the dynamic linearisation data model in MFAC theory is control-design-oriented, which simply describes the time-varying dynamic relationships between the change of system output at the next time instant and the changes of the control inputs within a moving time window. It is proposed only for control synthesis and is not suitable for system analysis or long-term prediction of the system output, therefore not any explicit information of the mathematical model of the controlled system is needed, which distinguishes the MFAC methods from conventional model-based control methods and avoids the issues of modelling uncertainties and unmodeled dynamics. Furthermore, the control-design-oriented dynamic linearisation data model has a simple structure, a moderate amount of adjustable parameters, and is much easier to be integrated with control algorithm design. Nevertheless, it might be arguable to classify the MFAC theory as “model-free” control methods since essentially a time series input-output data model is used for control synthesis. Hence, to avoid ambiguity, we use the notion of “conventional model-based control” to represent model-based control methods which require mathematical modeling (built by either first-principle modelling or system identification), while use the notion of “data-driven control” to represent the MFAC methods in this work. Based on the type of dynamic linearisation technique employed (compact-form dynamic linearisation (CFDL), partial-form dynamic linearisation (PFDL) and full-form dynamic linearisation (FFDL)), three different MFAC approaches were developed respectively. The stability analysis and robustness issue (against measurement noise and data dropout) of the PFDL-MFAC and CFDL-MFAC (a special case of PFDL-MFAC) methods have been studied with [157–161]. But the stability analysis of the FFDL-MFAC approach is still an open problem, which hinders its applicability. Thus we do not consider this algorithm in this work,

and by MFAC approach we mean the PFDL-MFAC approach hereinafter.

In this chapter, we design the flight control system for a very flexible flying wing developed in Chapter 2 using the MFAC scheme. Instead of devoting efforts to building a mathematical model with appropriate accuracy and system order for control synthesis, the characteristics of the aeroservoelastic system, such as the geometrical nonlinearities, time-varying parameters, etc., are estimated and integrated into the PPD of the online dynamic linearisation data model, based on which the adaptive control law is designed uniformly. However, the condition of applicability of MFAC approach requires that the sign of PPD remains unchanged, implying the system output needs to change monotonically with the control input. Such condition is not satisfied in the desired control bandwidth of a flight control problem, thus the MFAC algorithm cannot be directly applied, and extra damping effect is required to adjust the dynamics of the closed-loop system to meet this condition. Therefore, we propose a cascaded proportional-derivative MFAC (PD-MFAC) scheme to introduce damping effect for adjustment of the closed-loop dynamics, which accommodates the MFAC scheme in a flight control problem and improves the performance of the original MFAC algorithm. We thereby design the aeroelastic and trajectory control system based on the proposed PD-MFAC approach, to achieve desirable gust load alleviation and efficient path-following in three dimensions. A guidance system which can track both straight-line and curved paths is developed to generate the corresponding path-following commands. Simulation results based on the nonlinear aeroservoelastic model (2.4) show that the proposed data-driven flight control system is able to properly regulate all the rigid-body and flexible modes, and also achieves better effectiveness and robustness (against disturbance rejection and modelling uncertainties) than the baseline H_∞ control system, which is adapted from the flight control system developed in Chapter 3. These indicate the advantages of the data-driven MFAC scheme in addressing the flight control problem for VFA whose control design model usually has very high dimensions and/or big modelling errors when employing conventional model-based control design.

The structure of this chapter is organized as follows: Section 5.2 designs the guidance system to generate the path-following commands. Section 5.3 presents some background of the MFAC approach and designs the data-driven flight control system. Section 5.4 conducts simulation studies to test the performance of the control system and Section 5.5 concludes this chapter.

5.2 Guidance System

Recall that in Section 3.3.3, we used a waypoint tracking mechanism to direct the aircraft to track straight-line trajectory. We now extend the guidance system to track both straight-line and curved paths using the nonlinear guidance algorithm developed in [162].

Fig. 5.1 gives an illustration of the guidance system projected in the horizontal and vertical planes, respectively. A virtual target point (VTP) P_T is designated along the desired route at a constant distance L_T ahead of the current aircraft position. The guidance system then commands the vehicle to chase the VTP and asymptotically follow the path.

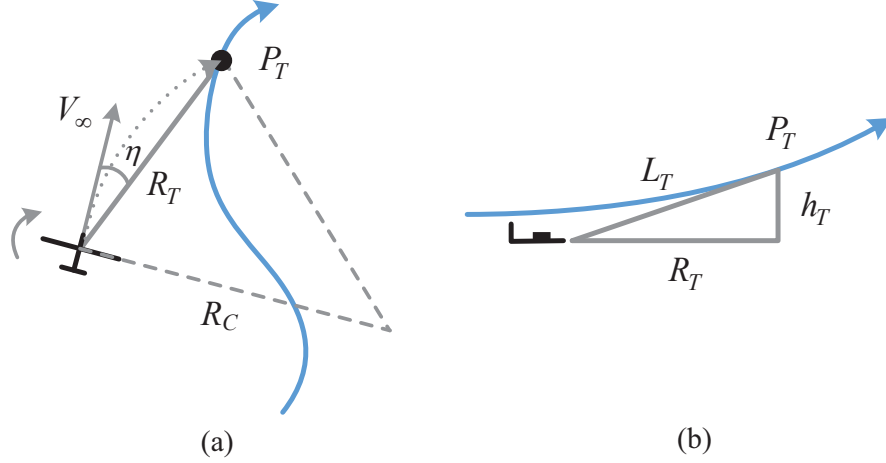


Figure 5.1: Illustration of the guidance system. The blue solid line denotes the predefined route.

Assuming the aircraft travels at constant speed, the horizontal subsystem (see Fig. 5.1(a)) prescribes a circular arc path which is tangential to the current heading of the vehicle and passes through the VTP. In this manner, we obtain the centripetal acceleration command as

$$a_{lc} = V_{\infty}^2 / R_C = 2V_{\infty}^2 \sin \eta / R_T,$$

where V_{∞} is the aircraft velocity, R_C is the desired turning radius, R_T is the projected distance of L_T in the horizontal plane and η is the heading error. To facilitate the implementation of this command with the control system in the lateral channel, by further assuming the aircraft maintains level flight, i.e. $L \cos \phi = mg$ and $L \sin \phi = ma_l$ where L is the lift force and ϕ is the roll angle, we derive the roll angle

command ϕ_r as

$$\phi_r = \text{atan}(a_{lc}/g) = \text{atan}(2V_\infty^2 \sin \eta / (gR_T)), \quad (5.1)$$

where g is the acceleration of gravity. On the other hand, the vertical subsystem (see Fig. 5.1(b)) prescribes a climb rate command to realize altitude tracking in the vertical plane, which is

$$\dot{H}_r = V_\infty h_T / L_T, \quad (5.2)$$

where h_T is the altitude difference between the VTP and the current position of the aircraft.

The roll angle command (5.1) and the climb rate command (5.2) are eventually used to command the control system to direct the aircraft toward the predefined route in three dimensions.

5.3 Control System

In this section, we design the data-driven flight control system for the very flexible flying wing based on the MFAC scheme. Following a conventional control structure, the control design is divided into the longitudinal channel and the lateral channel, as shown in Fig. 5.2.

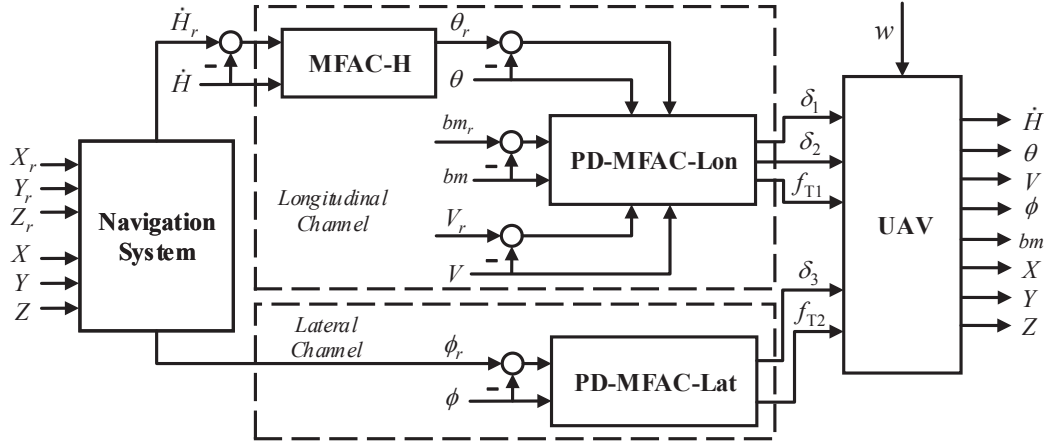


Figure 5.2: Control structure of the data-driven flight control system. \dot{H}, θ, V, bm and ϕ are the climb rate, pitch angle, forward velocity, root bending moment and roll angle, respectively. X, Y, Z are the geometric position of the aircraft. The subscript symbol r denotes the reference command. MFAC-H, PD-MFAC-Lon and PD-MFAC-Lat denote the longitudinal outer-loop climb rate controller, the longitudinal inner-loop controller and the lateral inner-loop controller, respectively.

In the longitudinal channel, we employ the two-loop control scheme to achieve altitude tracking. The outer-loop controller tracks the climb rate command received from the guidance system and generates a pitch angle command to the inner loop, which is regulated by a MFAC controller using the climb rate \dot{H} as feedback. While the inner-loop MFAC controller serves as the aeroelastic control loop for gust load alleviation, and also acts to track the pitch angle command from the outer loop and stabilize the forward velocity and root bending moment, simultaneously. This is achieved by generating longitudinal control inputs (to the corresponding flaps and thrust), using pitch angle θ , root bending moment bm and forward velocity V as feedback. Note that the objective of stabilizing the root bending moment is to maintain the aircraft at its trimmed shape during maneuver and suppress the structural vibration modes. In the lateral channel, we employ a MFAC controller to generate lateral control inputs (to the corresponding flaps and thrust) to track the roll angle command from the guidance system, using roll angle ϕ as feedback. Again, we mention that the center node of the flying wing is selected as reference point to track the aircraft flight dynamics, thus all the output measurements are defined at this reference point.

5.3.1 MFAC Algorithm Preliminaries

Before diving into the detailed control design, we briefly introduce some background on the MFAC algorithm [157, 158]. Consider a class of nonlinear single-input single-output (SISO) systems described in the discrete-time domain as follows:

$$y(k+1) = f(y(k), \dots, y(k-n_y), u(k), \dots, u(k-n_u)), \quad (5.3)$$

where $y(k)$ and $u(k)$ are the system output and control input at time k , f is an unknown nonlinear function, n_y and n_u are unknown positive integers. We define $\mathbf{U}_{L_c}(k) = [u(k), \dots, u(k-L_c+1)]^T$ as the vector of all the history control inputs within the time window $[k-L_c+1, k]$ where L_c is called the linearisation length constant, $\Delta y(k) = y(k) - y(k-1)$ and $\Delta \mathbf{U}_{L_c}(k) = \mathbf{U}_{L_c}(k) - \mathbf{U}_{L_c}(k-1)$ as the respective change of system output and control input between two consecutive time steps.

Assumption 5.1: The partial derivatives of function f with respect to the control input $u(k), \dots, u(k-L_c+1)$ are continuous, and system (5.3) satisfies the generalized Lipschitz condition: $|\Delta y(k+1)| \leq b \|\Delta \mathbf{U}_{L_c}(k)\|$ for any k and $\Delta \mathbf{U}_{L_c}(k) \neq 0$. Here, b is a positive bounded constant and $\|\cdot\|$ is the Euclidean norm of a vector.

For system (5.3) satisfying *Assumption 5.1*, when $\|\Delta \mathbf{U}_{L_c}(k)\| \neq 0$, there exists a time-varying vector $\boldsymbol{\xi}_{L_c}(k)$ called the pseudo partial derivative (PPD) vector,

such that system (5.3) can be equivalently described by the following partial form dynamic linearisation (PFDL) data model

$$\Delta y(k+1) = \boldsymbol{\xi}_{L_c}(k) \Delta \mathbf{U}_{L_c}(k) \quad (5.4)$$

in which $\boldsymbol{\xi}_{L_c}(k) = [\xi_1(k), \dots, \xi_{L_c}(k)]$ is bounded at any time k .

Based on the PFDL data model (5.4), the PFDL-MFAC algorithm for SISO systems are given as follows,

$$u(k) = u(k-1) + \frac{\rho_1 \hat{\xi}_1(k)(y_r(k+1) - y(k))}{\lambda + \left| \hat{\xi}_1(k) \right|^2} - \frac{\hat{\xi}_1(k) \sum_{i=2}^{L_c} \rho_i \hat{\xi}_i(k) \Delta u(k-i+1)}{\lambda + \left| \hat{\xi}_1(k) \right|^2}, \quad (5.5a)$$

$$\begin{aligned} \hat{\boldsymbol{\xi}}_{L_c}(k) &= \hat{\boldsymbol{\xi}}_{L_c}(k-1) + \zeta \Delta \mathbf{U}_{L_c}(k-1) * \\ &\quad \frac{(\Delta y(k) - \hat{\boldsymbol{\xi}}_{L_c}^T(k-1) \Delta \mathbf{U}_{L_c}(k-1))}{\mu + \|\Delta \mathbf{U}_{L_c}(k-1)\|^2}, \end{aligned} \quad (5.5b)$$

$$\begin{aligned} \hat{\boldsymbol{\xi}}_{L_c}(k) &= \hat{\boldsymbol{\xi}}_{L_c}(1), \text{ if } \left\| \hat{\boldsymbol{\xi}}_{L_c}(k) \right\| \leq \varepsilon, \text{ or } \|\Delta \mathbf{U}_{L_c}(k-1)\| \leq \varepsilon, \\ &\text{or } \text{sign}(\hat{\xi}_1(k)) \neq \text{sign}(\hat{\xi}_1(1)), \end{aligned} \quad (5.5c)$$

in which the controller algorithm (5.5a) is derived from minimizing the weighted one-step-ahead cost function of tracking error and control input rate,

$$J(u(k)) = |y_r(k+1) - y(k+1)|^2 + \lambda |u(k) - u(k-1)|^2,$$

while the PG estimation algorithm (5.5b) is derived similarly by minimizing the weighted cost function

$$J(\boldsymbol{\xi}(k)) = \left| \Delta y(k) - \hat{\boldsymbol{\xi}}_{L_c}^T(k) \Delta \mathbf{U}_{L_c}(k-1) \right|^2 + \mu \left\| \hat{\boldsymbol{\xi}}_{L_c}(k) - \hat{\boldsymbol{\xi}}_{L_c}(k-1) \right\|^2.$$

The reset algorithm (5.5c) is added to facilitate the PPD vector estimation algorithm (5.5b) to track time-varying parameters. $\rho_i \in (0, 1]$ and $\zeta \in (0, 2]$ are the step factors, and $\lambda > 0, \mu > 0$ are the penalty factors. $\hat{\boldsymbol{\xi}}_{L_c}(k)$ is the estimated value of PPD vector $\boldsymbol{\xi}_{L_c}(k)$. We mention that when $L_c = 1$, the PFDL-MFAC becomes the CFDL-MFAC. The stability and convergence of the MFAC algorithm (5.5) for SISO systems was discussed in [157], assuming the sign of the PPD $\xi_1(k)$ remains unchanged.

Similarly, consider a class of multiple-input multiple-output (MIMO) systems described in the discrete-time domain as

$$\mathbf{y}(k+1) = \mathbf{f}(\mathbf{y}(k), \dots, \mathbf{y}(k-n_y), \mathbf{u}(k), \dots, \mathbf{u}(k-n_u)), \quad (5.6)$$

where $\mathbf{y}(k)$ and $\mathbf{u}(k)$ are the system output and control input at time k , $\mathbf{f} = (f_1, \dots, f_m)^T$ is the unknown nonlinear vector-valued function. The vector of all the history control inputs within the time window $[k-L_c+1, k]$ is denoted as $\mathbf{H}_{L_c}(k) = [\mathbf{u}^\top(k), \dots, \mathbf{u}^\top(k-L_c+1)]^\top$.

Assumption 5.2: The partial derivatives of function $f_{i,i=1\dots m}$ with respect to all elements of the control input $\mathbf{u}(k), \dots, \mathbf{u}(k-L_c+1)$ are continuous, and system (5.6) satisfies the generalized Lipschitz condition: $|\Delta \mathbf{y}(k+1)| \leq b \|\Delta \mathbf{H}_{L_c}(k)\|$ for any k and $\Delta \mathbf{H}_{L_c}(k) \neq 0$.

For system (5.6) satisfying *Assumption 5.2*, following the same procedure by minimizing the corresponding cost functions for the controller algorithm and the estimation algorithm, the MFAC algorithm for MIMO systems (5.6) are derived as

$$\begin{aligned} \mathbf{u}(k) = & \mathbf{u}(k-1) + \frac{\rho_1 \hat{\Xi}_1^T(k)(\mathbf{y}^*(k+1) - \mathbf{y}(k))}{\lambda + \|\hat{\Xi}_1(k)\|^2} \\ & - \frac{\hat{\Xi}_1^T(k) \sum_{i=2}^{L_c} \rho_i \hat{\Xi}_i^T(k) \Delta \mathbf{u}(k-i+1)}{\lambda + \|\hat{\Xi}_1(k)\|^2}, \end{aligned} \quad (5.7a)$$

$$\begin{aligned} \hat{\Xi}_{L_c}(k) = & \hat{\Xi}_{L_c}(k-1) + \zeta \Delta \mathbf{H}_{L_c}(k-1) * \\ & \frac{(\Delta \mathbf{y}(k) - \hat{\Xi}_{L_c}^T(k-1) \Delta \mathbf{H}_{L_c}(k-1))}{\mu + \|\Delta \mathbf{H}_{L_c}(k-1)\|^2}, \end{aligned} \quad (5.7b)$$

$$\begin{aligned} \hat{\xi}_{iiq}(k) = & \hat{\xi}_{iiq}(1)_{[i,q=1,\dots,m]}, \text{ if } \left| \hat{\xi}_{iiq}(k) \right| < b_2, \text{ or} \\ & \left| \hat{\xi}_{iiq}(k) \right| > ab_2, \text{ or } \text{sign}(\hat{\xi}_{iiq}(k)) \neq \text{sign}(\hat{\xi}_{iiq}(1)), \\ \hat{\xi}_{ijq}(k) = & \hat{\xi}_{ijq}(1)_{[i,j,q=1,\dots,m,i \neq j]}, \text{ if } \left| \hat{\xi}_{ijq}(k) \right| > b_1, \\ & \text{or } \text{sign}(\hat{\xi}_{ijq}(k)) \neq \text{sign}(\hat{\xi}_{ijq}(1)), \end{aligned} \quad (5.7c)$$

where (5.7c) is the corresponding reset algorithm, and $\hat{\Xi}_{L_c}(k)$ is the estimated value of the PPD matrix $\Xi_{L_c}(k)$. The stability and convergence analysis of the MFAC algorithm for MIMO systems was discussed in [158], assuming that the PPD matrix $\Xi_1(k)$ is a diagonally dominant matrix and the sign of all the elements in $\Xi_1(k)$ remain unchanged.

Remark 1: *Assumption 5.1* (or *5.2*) is a typical constraint for general nonlinear system in the field of control system design, and imposes an upper bound on the

change rate of the system output driven by the change of the control input.

Remark 2: It is important to mention that we use two other strong assumptions when applying the MFAC algorithm in the flight control problem. First, since the aircraft's dynamics to small perturbations at any operating point can be formulated into the form of (5.6), we assume the aircraft system satisfies the description of (5.6) in the context of this work. Second, the assumption on the diagonal dominance of the PPD matrix $\Xi_1(k)$ and the fixed sign of all the elements in $\Xi_1(k)$ is implicitly satisfied by assigning a dominant control input to regulate the corresponding output (the non-dominant effects from other control inputs are taken into account via the non-diagonal elements of the PPD matrix and the damping gain parameter matrix to be introduced in the next subsection), and is guaranteed by the reset algorithm.

5.3.2 Longitudinal Inner-loop Control Design

We now design the longitudinal inner-loop controller using the MFAC scheme. However, as discussed earlier, the original MFAC algorithm cannot be applied directly. The condition of applicability of the original MFAC approach requires that the sign of pseudo partial derivative (PPD) remains unchanged, which implies the system output needs to change monotonically with the control input. Nevertheless, such condition is not satisfied in the desired control bandwidth of the inner-loop system, thus extra damping effect is required to adjust the dynamics of the closed-loop system to meet this condition. This can be normally achieved by introducing damping effect to adjust the closed-loop system phase through derivatives of the controlled signal, just as the derivative term functions in PID control. On the other hand, in the control law of the MFAC algorithm, a set of step factors are used as proportional gains to tune the speed of the closed-loop response. Faster dynamic response requires larger gains and vice versa. However, increasing the proportional gains alone to meet the performance specifications of the inner-loop control problem, may lead to undesirable overshoot, oscillations or even unstable dynamics in the system response due to the absence of damping effect. Therefore, it is of great importance to introduce derivatives of the controlled signal for control damping in the MFAC scheme to obtain an appropriate dynamic response in the desired control bandwidth.

To serve this purpose, we propose a cascaded proportional-derivative MFAC (PD-MFAC) approach, which integrates the original MFAC algorithm with necessary damping effect to accommodate the MFAC scheme in the inner-loop control design and improve the control performance of the original MFAC approach. It is clear from Fig. 5.2 that the longitudinal inner-loop system is a MIMO system, the control structure of the PD-MFAC approach for MIMO systems (denoted as

PD-MFAC-MIMO) is as depicted in Fig. 5.3.

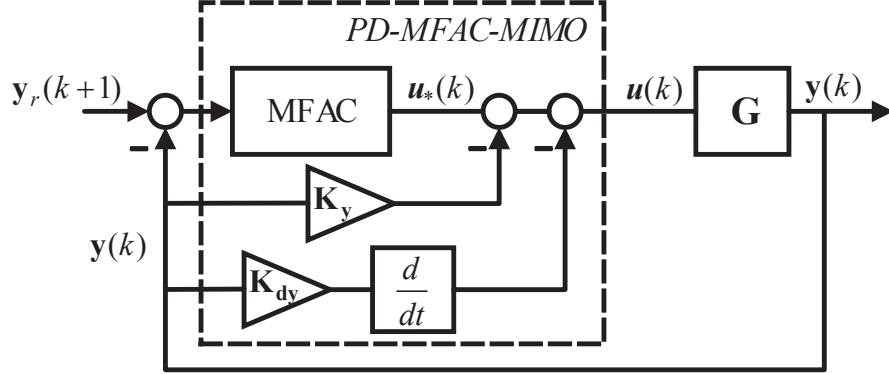


Figure 5.3: Control structure of the cascaded PD-MFAC-MIMO algorithm. \mathbf{G} denotes the unknown nonlinear system plant.

We define a vector of virtual control input $\mathbf{H}_{*L_c}(k) = [\mathbf{u}_*^\top(k), \dots, \mathbf{u}_*^\top(k - L_c + 1)]^\top$ within the moving time window $[k - L_c + 1, k]$, in which the virtual control input is given as

$$\mathbf{u}_*(k) = \mathbf{u}(k) + \mathbf{K}_y \mathbf{y}(k) + \mathbf{K}_{dy} \Delta \mathbf{y}(k)/dt. \quad (5.8)$$

Here, \mathbf{K}_y and \mathbf{K}_{dy} are the parameter matrices added to introduce the corresponding derivative terms, dt is the sampling time of the control system. Then, we derive the PD-MFAC-MIMO algorithm as below,

$$\begin{aligned} \mathbf{u}(k) = & \mathbf{u}(k-1) + \frac{\rho_1 \hat{\Xi}_{*1}^T(k) (\mathbf{y}^*(k+1) - \mathbf{y}(k))}{\lambda + \|\hat{\Xi}_{*1}(k)\|^2} \\ & - \frac{\hat{\Xi}_{*1}^T(k) \sum_{i=2}^L \rho_i \hat{\Xi}_{*i}^T(k) \Delta \mathbf{u}_*(k-i+1)}{\lambda + \|\hat{\Xi}_{*1}(k)\|^2} \\ & - \text{sign}(\hat{\Xi}_{*1}(1)) (\mathbf{K}_y \Delta \mathbf{y}(k) + \frac{\mathbf{K}_{dy}}{dt} \Delta(\Delta \mathbf{y}(k))), \end{aligned} \quad (5.9a)$$

$$\begin{aligned} \hat{\Xi}_{*L}(k) = & \hat{\Xi}_{*L}(k-1) + \zeta \Delta \mathbf{H}_{*L}(k-1) * \\ & \frac{(\Delta \mathbf{y}(k) - \hat{\Xi}_L^T(k-1) \Delta \mathbf{H}_{*L}(k-1))}{\mu + \|\Delta \mathbf{H}_{*L}(k-1)\|^2}, \end{aligned} \quad (5.9b)$$

$$\begin{aligned} \hat{\xi}_{*iiq}(k) = & \hat{\xi}_{*iiq}(1)_{[i,q=1,\dots,m]}, \text{ if } |\hat{\xi}_{*iiq}(k)| < b_2, \text{ or} \\ & |\hat{\xi}_{*iiq}(k)| > ab_2, \text{ or } \text{sign}(\hat{\xi}_{*iiq}(k)) \neq \text{sign}(\hat{\xi}_{*iiq}(1)), \\ \hat{\xi}_{*ijq}(k) = & \hat{\xi}_{*ijq}(1)_{[i,j,q=1,\dots,m,i \neq j]}, \text{ if } |\hat{\xi}_{*ijq}(k)| > b_1, \\ & \text{or } \text{sign}(\hat{\xi}_{*ijq}(k)) \neq \text{sign}(\hat{\xi}_{*ijq}(1)), \end{aligned} \quad (5.9c)$$

where $\Delta(\Delta \mathbf{y}(k)) = \Delta \mathbf{y}(k) - \Delta \mathbf{y}(k-1)$. To attenuate the impact of sensor measurement noise, a noise-tolerant tracking differentiator (TD) [163–165] can be employed to obtain the derivative signals $\Delta \mathbf{y}(k)/dt$. Based on the above analysis, we remark that the PD-MFAC scheme can be equivalently regarded as a cascade of MFAC and PD control, it extends the applicability of the MFAC approach and improves the control performance with the aid of appropriate damping effect. The longitudinal inner-loop controller is then designed based on the PD-MFAC-MIMO algorithm (5.9). The stability analysis of the algorithm (5.9) will be discussed in Section 5.3.5.

As mentioned earlier, within the original MFAC scheme, the FFDL-MFAC approach [155] taking account of the history data of system output may potentially provide an alternative solution, but its stability analysis is still an open problem, thus not considered in this thesis.

5.3.3 Lateral Inner-loop Control Design

The inner-loop system in the lateral channel is a multiple-input single-output (MISO) system. The corresponding PD-MFAC algorithm for MISO systems (PD-MFAC-MISO) based on which the lateral inner-loop controller is designed can be easily adapted from the PD-MFAC-MIMO algorithm (5.9), which is

$$\begin{aligned} \mathbf{u}(k) = & \mathbf{u}(k-1) + \frac{\rho_1 \hat{\boldsymbol{\xi}}_{*1}^T(k)(y^*(k+1) - y(k))}{\lambda + \|\hat{\boldsymbol{\xi}}_{*1}(k)\|^2} \\ & - \frac{\hat{\boldsymbol{\xi}}_{*1}^T(k) \sum_{i=2}^L \rho_i \hat{\boldsymbol{\xi}}_{*i}^T(k) \Delta \mathbf{u}_*(k-i+1)}{\lambda + \|\hat{\boldsymbol{\xi}}_{*1}(k)\|^2} \end{aligned} \quad (5.10a)$$

$$\begin{aligned} & - \text{sign}(\hat{\boldsymbol{\xi}}_{*1}(1))(\mathbf{K}_y \Delta y(k) + \frac{\mathbf{K}_{dy}}{dt} \Delta(\Delta y(k))), \\ \hat{\boldsymbol{\xi}}_{*L_c}(k) = & \hat{\boldsymbol{\xi}}_{*L_c}(k-1) + \eta \Delta \bar{\mathbf{U}}_{*L_c}(k-1) * \\ & \frac{(\Delta y(k) - \hat{\boldsymbol{\xi}}_{*L_c}^T(k-1) \Delta \bar{\mathbf{U}}_{*L_c}(k-1))}{\mu + \|\Delta \bar{\mathbf{U}}_{*L_c}(k-1)\|^2}, \end{aligned} \quad (5.10b)$$

$$\begin{aligned} \hat{\xi}_{*iq}(k) = & \hat{\xi}_{*iq}(1)_{[i,q=1,\dots,m]}, \text{ if } |\hat{\xi}_{*iiq}(k)| < b_2, \\ \text{or } & \text{sign}(\hat{\xi}_{*iq}(k)) \neq \text{sign}(\hat{\xi}_{*iq}(1)), \end{aligned} \quad (5.10c)$$

where $\bar{\mathbf{U}}_{*L_c}(k-1) = [\mathbf{u}_*^T(k), \dots, \mathbf{u}_*^T(k-L_c+1)]^T$ is the vector of the virtual control inputs $\mathbf{u}_*(k)$. \mathbf{K}_y and \mathbf{K}_{dy} are the parameter vectors added to introduce the corresponding derivative terms.

5.3.4 Longitudinal Outer-loop Control Design

In terms of the longitudinal outer-loop control design, since the change of the climb rate \dot{H} (system output) with regard to the pitch angle θ (control input) is approximately monotonic in the sense $\dot{H} \approx V\theta$ at all times (V is the forward velocity), we therefore directly employ the MFAC-SISO algorithm (5.5) to design the longitudinal outer-loop controller for climb rate control.

5.3.5 Stability Analysis

We now present the stability analysis of the cascaded PD-MFAC-MIMO algorithm. An equivalent form of the control structure of the PD-MFAC-MIMO scheme is given as in Fig. 5.4 to facilitate the analysis. It is clear that the stability analysis of the PD-MFAC-MIMO algorithm (5.9) with respect to the nonlinear system plant \mathbf{G} (see Fig. 5.3) is now converted into the stability analysis of the original MFAC-MIMO algorithm (5.9) with respect to the augmented system plant \mathbf{P} (see Fig. 5.4).

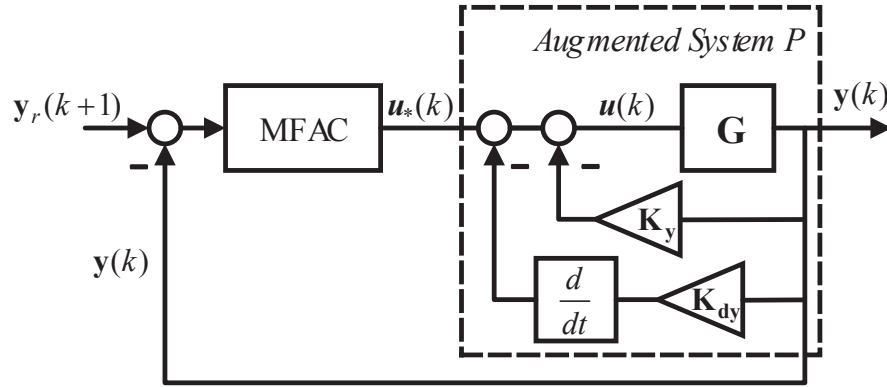


Figure 5.4: Equivalent control structure of the cascaded PD-MFAC-MIMO algorithm. \mathbf{P} denotes the augmented system plant consisting of the original system plant and the damping terms.

The existence of the PFDL data model of the augmented system plant \mathbf{P} and the stability analysis of the PD-MFAC-MIMO algorithm (5.9) follow immediately from the proof of *Theorem 3* and *Theorem 4* in [158], thus omitted here. We refer to [158] for details.

5.4 Simulation Results

In this section, we conduct simulation tests to check the performance of the data-driven flight control system developed in Section 5.3, based on the nonlinear aeroservoelastic model (2.4) of the very flexible flying wing with full-payload configuration,

for which we refer to Section 2.4 for details. The 4th-order Runge-Kutta solver *ode45* in Matlab[®] is used in the nonlinear simulations and the control inputs are updated at the frequency of 20Hz. All the control actuators are modelled as first-order lag systems with time constants of 0.3 seconds and the operating range of -100N~200N for thrust and $\pm 20^\circ$ for flap deflections (as in Chapter 4, certain negative thrust are assumed to be available to act as air brakes to increase drag and reduce speed). The distance to the reference point on the desired path in the guidance system is set as $L_T = 250m$.

5.4.1 Step Response

This subsection compares the dynamic performance of the PD-MFAC approach against the original MFAC approach. Unit step commands of pitch and roll angle are applied to the inner-loop control system from the beginning of simulations, the responses of pitch and roll angle using the original MFAC approach and the proposed PD-MFAC approach are shown in the top and middle diagrams of Fig. 5.5, respectively. Recall that with full-payload configuration, the open-loop system of the flying wing is unstable (see Section 3.3.1). As shown in Fig. 5.5, the MFAC controller fails to stabilize the system due to the lack of necessary damping effect to adjust closed-loop system phase (see Section 5.3.2 for detailed explanations), while the PD-MFAC controller successfully stabilizes the system. We mention that the dynamic responses of root bending moment, forward velocity and actuator dynamics are also satisfactory, but their plots are omitted here for brevity. Furthermore, to give a straight comparison of the dynamic performance between the PD-MFAC and the original MFAC approach, we design the inner-loop controllers using these two methods for a flying wing configuration with 40% payload (open-loop stable [19]). The corresponding step responses are shown in the bottom diagrams of Fig. 5.5. It is clear that with the MFAC controller, the pitch angle response is relatively slow with obvious oscillations, and the roll angle response exhibits large overshoot. In contrast, the PD-MFAC controller achieves faster and more smooth response in the pitch angle and roll angle, where the oscillations and overshoot are well damped by the introduced damping effect. All these results demonstrate that the PD-MFAC approach achieves better performance than the original MFAC approach.

5.4.2 Disturbance Rejection

This subsection investigates the robust performance of the data-driven control system with respect to disturbance rejection. The control system is commanded to

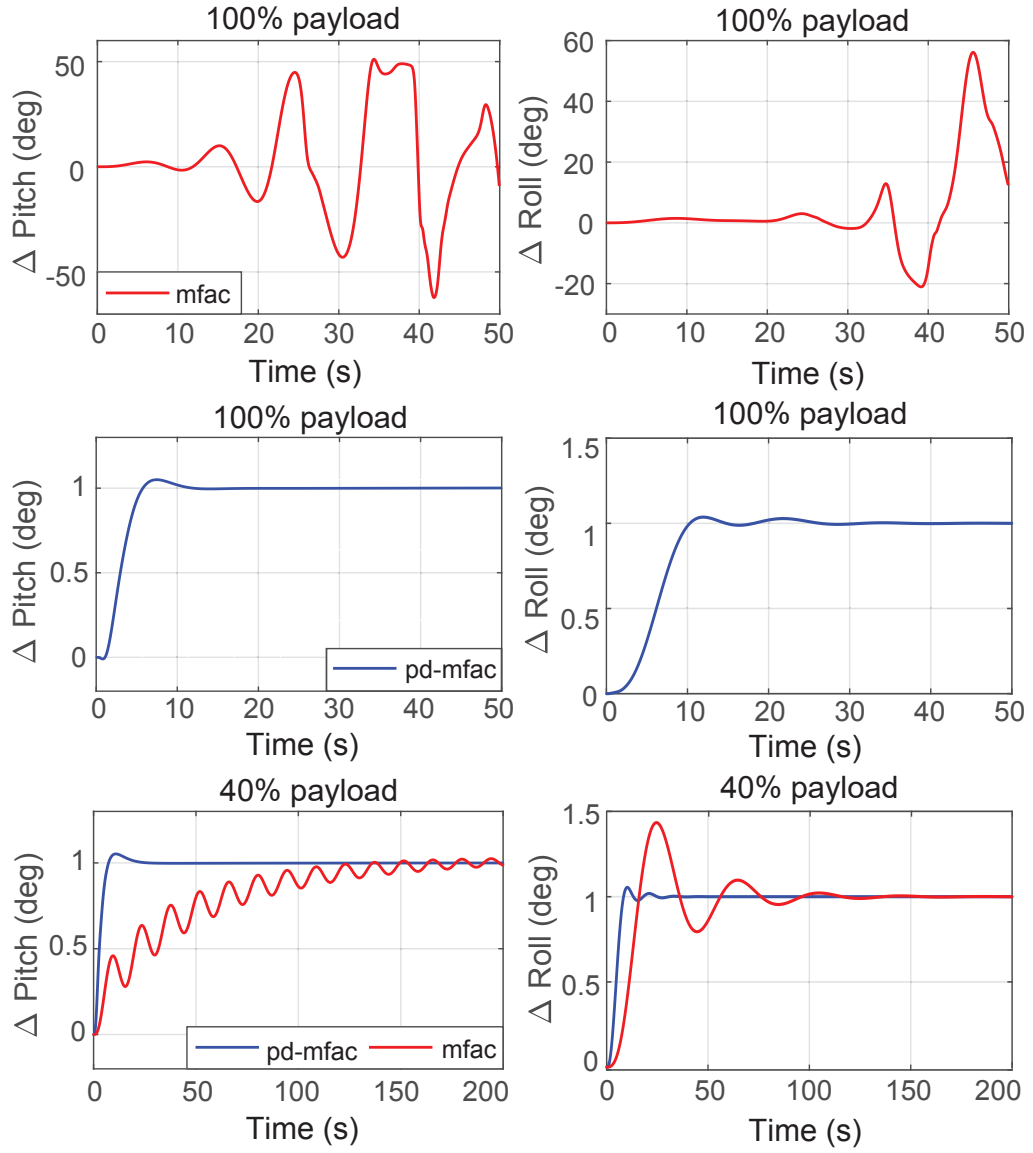


Figure 5.5: Step response of the inner-loop control system designed using the PD-MFAC approach and the original MFAC approach, respectively.

maintain the aircraft along a straight-line path at $H=0m$ in the presence of wind turbulence. A conventional model-based control system with satisfactory performance, employing H_∞ control in both the longitudinal and lateral inner loop (developed in Chapter 3), is utilized as a baseline controller for performance comparison. To facilitate a straightforward performance comparison between the PD-MFAC and H_∞ control, we use the same guidance system (see Section 5.2) and the same longitudinal outer-loop controller (see Section 5.3.4) in both control systems. The continuous three-dimensional turbulence used in the simulations are generated based on von Kármán velocity spectra with the scale length $L_w = 5m, L_u = L_v = 38.85m$ and the intensity $\sigma_w = 0.5m/s, \sigma_u = \sigma_v = 1m/s$. The time history of the turbulence applied is shown in Fig. 5.6.

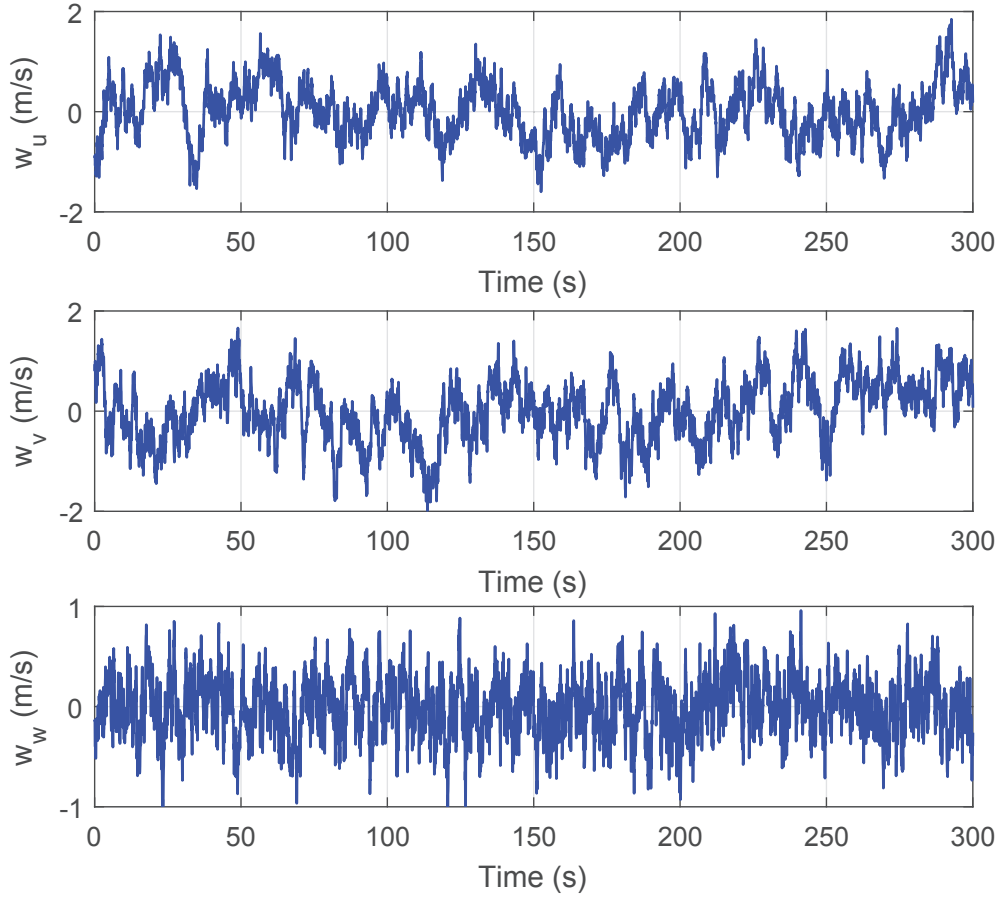


Figure 5.6: Time history of the synthetic von Kármán turbulence. u, v, w denote the lateral, forward and vertical component, respectively.

The responses of the flying wing (full-payload) with the data-driven control system are depicted in Fig. 5.7 and Fig. 5.8, compared to those with the baseline

H_∞ control system. It is clear that both control systems succeed to maintain the aircraft along the desired straight-line path in turbulence. With the data-driven control system, the root-mean-square (RMS) value of the oscillations in altitude, pitch angle, roll angle, forward velocity and root bending moment are reduced by 47%, 52%, 36%, 59% and 56%, compared to those with the H_∞ control system, while the oscillations in lateral displacement (the lateral deviation of the aircraft position to the desired path) is slightly reduced by 3%. The reductions of the left (ΔL_{Tip}) and right wing tip (ΔR_{Tip}) displacement relative to the center of the flying wing are 48% and 47%, respectively. These results show that the data-driven control system has achieved better robustness against disturbance rejection than the H_∞ controller in our case of flight control for VFA. The corresponding control input are as shown in Fig. 5.9, which shows that the corresponding control inputs are within reasonable range.

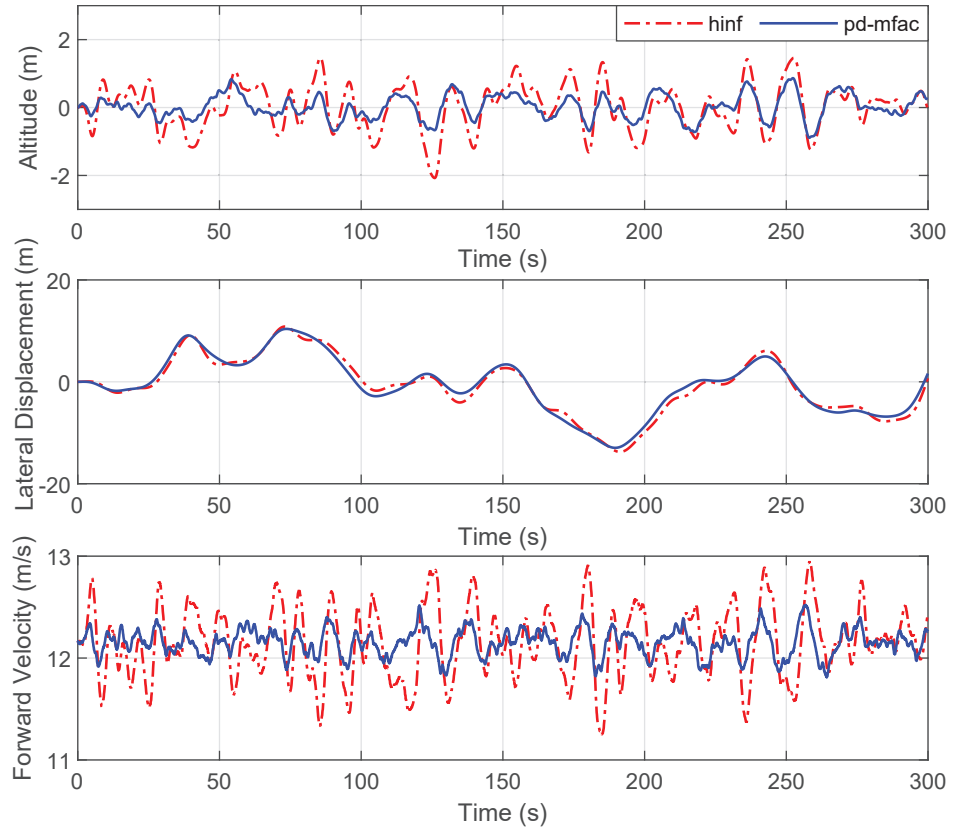


Figure 5.7: Time histories of the altitude, lateral displacement and forward velocity responses with the data-driven and H_∞ control systems in the presence of wind turbulence.

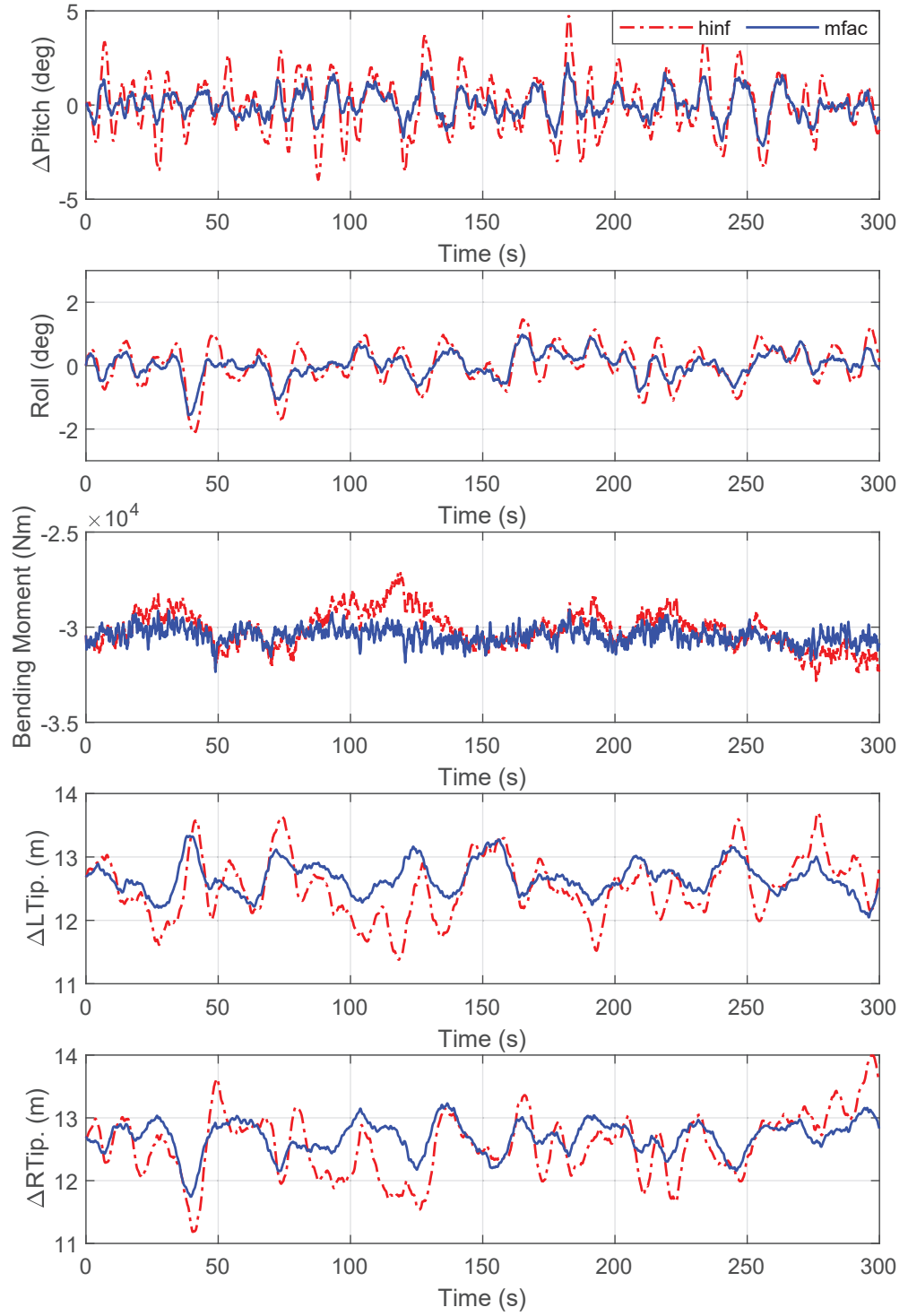


Figure 5.8: Time histories of the pitch, roll, bending moment, left wingtip and right wingtip responses with the data-driven and the H_∞ control systems in the presence of wind turbulence.

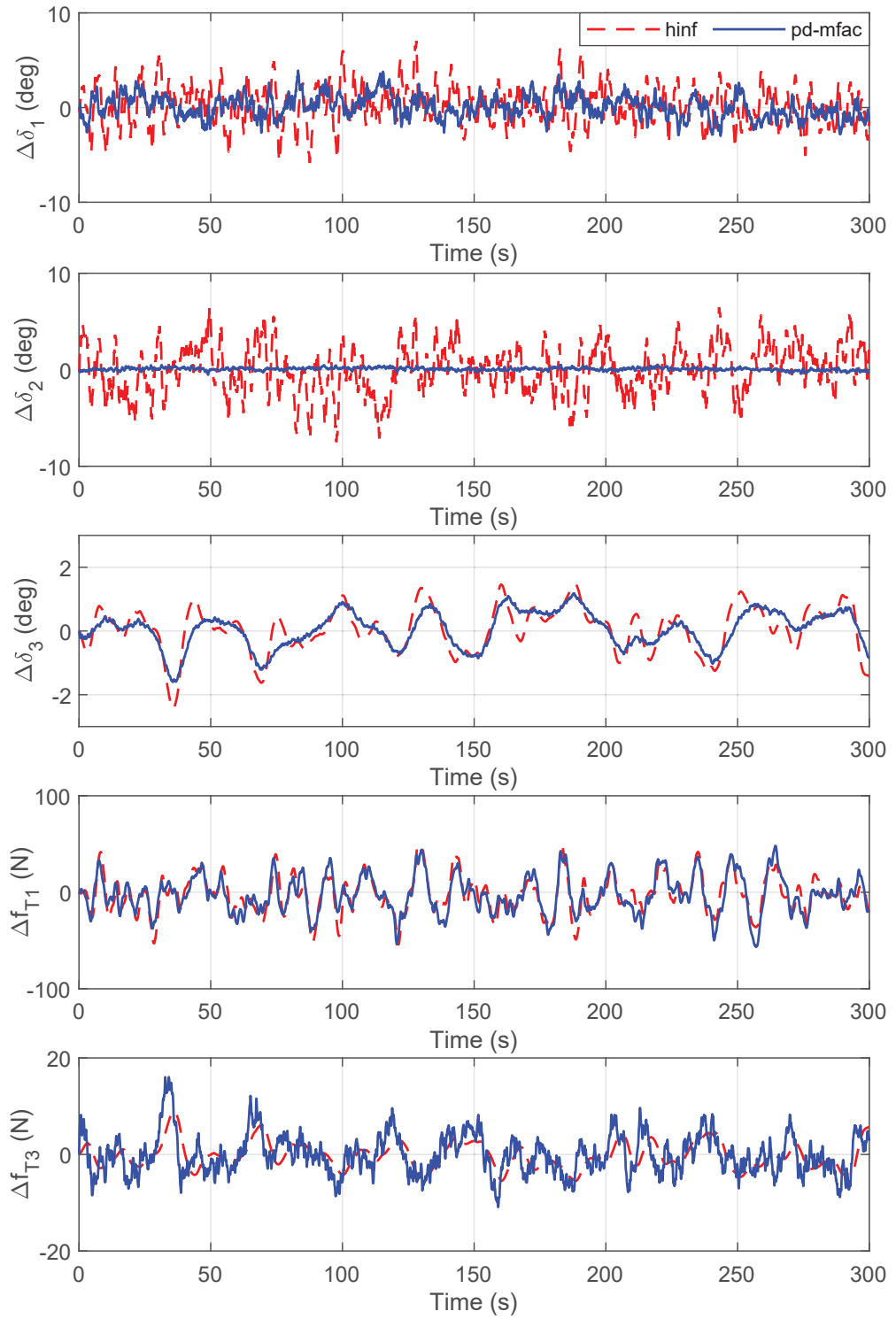


Figure 5.9: Time histories of the control inputs with the data-driven and the H_∞ control systems in the presence of wind turbulence.

5.4.3 Robust Performance

We now demonstrate the data-driven control system's robustness with respect to modelling uncertainties. We repeat the above simulations on the nonlinear aeroservoelastic model (2.4) with varying bending stiffness (EI_2), namely, the "more" ($0.9EI_2$) and "less" ($1.1EI_2$) flexible configurations relative to the nominal very flexible flying wing ($1.0EI_2$), using the same data-driven and the H_∞ control systems as in the previous section. The corresponding responses of the aircraft are shown in Fig. 5.10 and Fig. 5.11. In both figures, it shows that on the "less" flexible configuration (left-side diagrams), although the responses of all the variables become more disturbed, both control systems still succeed to maintain the aircraft along the desired path with good disturbance rejection performance, but the data-driven control system outperforms the H_∞ control system in reducing oscillations in altitude, lateral displacement, forward velocity, pitch angle, roll angle, root bending moment, left wing tip and right wing tip by 33%, 9%, 62%, 55%, 52%, 43%, 24% and 26%, respectively. In the case of "more" flexible configuration (see right-side diagrams of Fig. 5.10 and Fig. 5.11) which represents a more severe situation, the H_∞ control system fails to stabilize the aircraft while the data-driven one still works with satisfactory performance. All these results indicate the better effectiveness and robustness of the data-driven control system against modelling uncertainties. The corresponding control inputs are as shown in Fig. 5.12.

5.4.4 Path following in Turbulence

This subsection shows the path-following performance of the data-driven control system in turbulence, based on the nominal very flexible flying wing model (i.e. full-payload configuration without uncertainties in the bending stiffness EI_2). The control system aims to drive the aircraft to follow a spiral path of the turning radius $R_C = 500m$ with the climb rate $\dot{H} = 0.432m/s$. The same von Kármán turbulence used in the previous section is applied. The responses of the flying wing with the data-driven control system and the H_∞ control system are depicted in Fig. 5.13. It is clear that the data-driven control system is able to direct the aircraft to follow the desired path in the presence of wind turbulence, and all the variables are within appropriate range. Note that there exists a steady tracking error in the altitude, this is due to the slow climb rate response of the control system when tracking a varying command. As analyzed in Section 5.4.3, one can see that the data-driven control system out-performs the H_∞ control system in this test case.

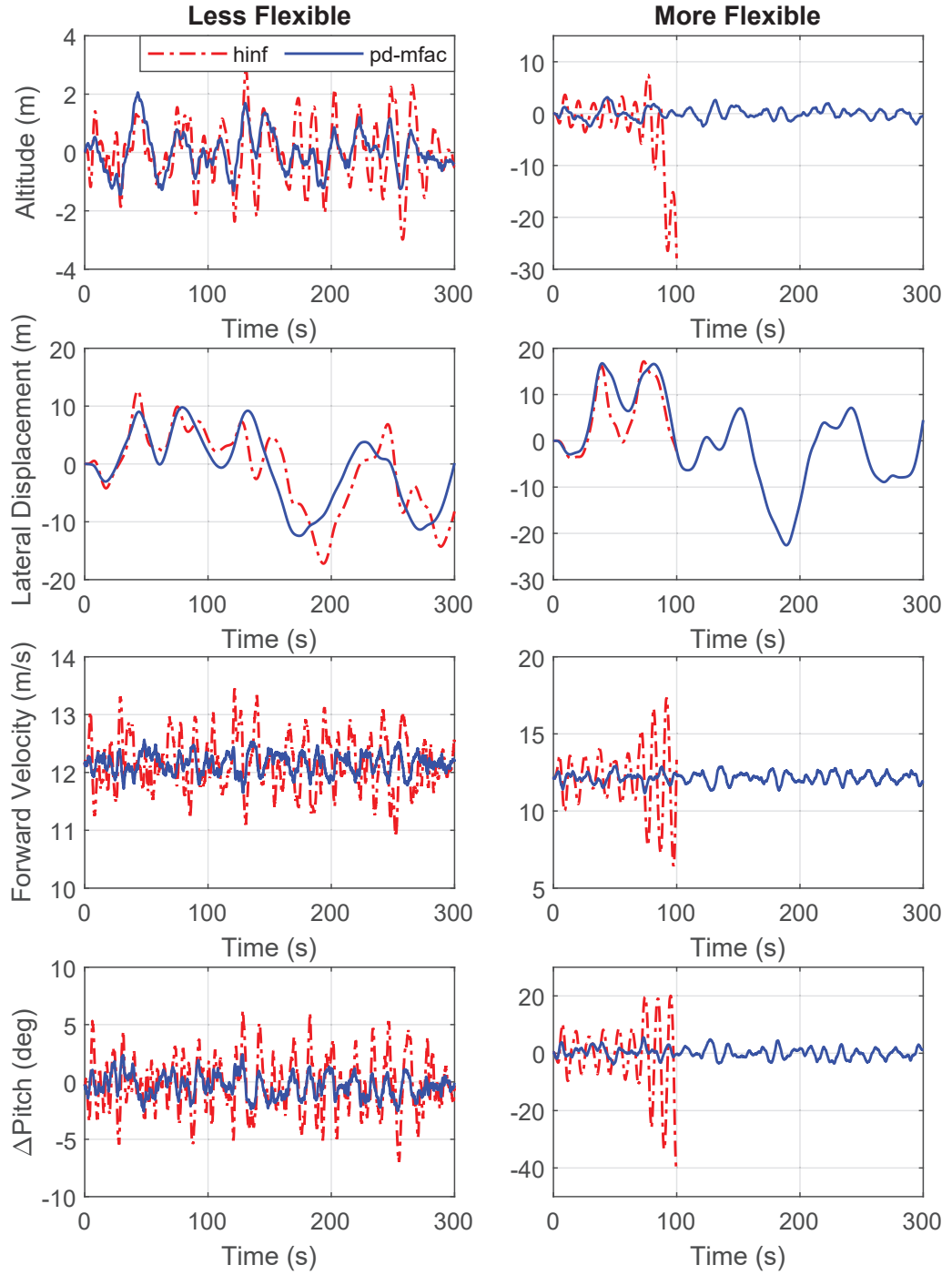


Figure 5.10: Time histories of the altitude, lateral displacement, forward velocity and pitch response with the data-driven and the H_{∞} control systems in turbulence, based on two very flexible configurations with varying bending stiffness.

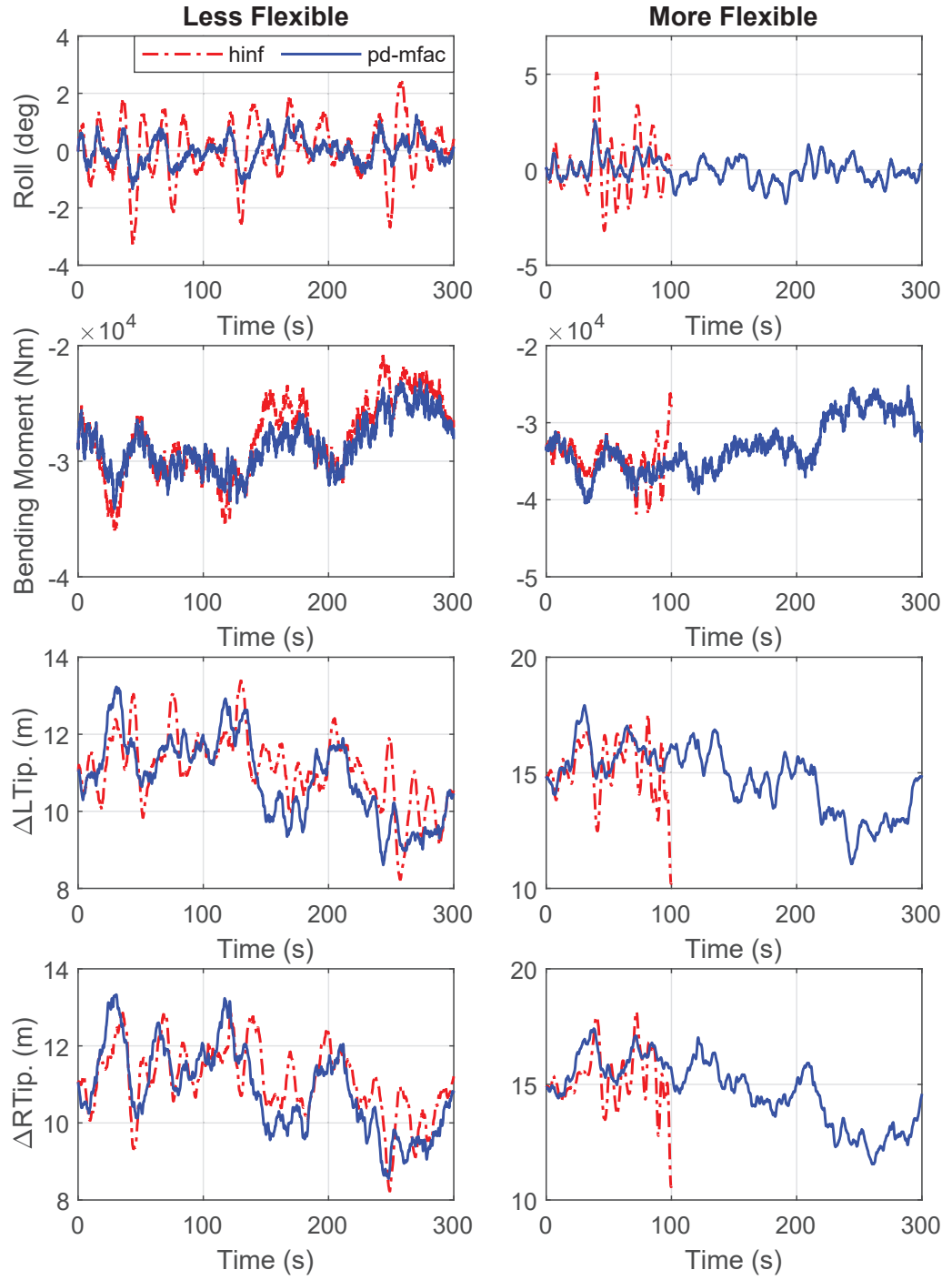


Figure 5.11: Time histories of the roll angle, bending moment, left wingtip and right wingtip response with the data-driven and the H_∞ control systems in turbulence, based on two very flexible configurations with varying bending stiffness.

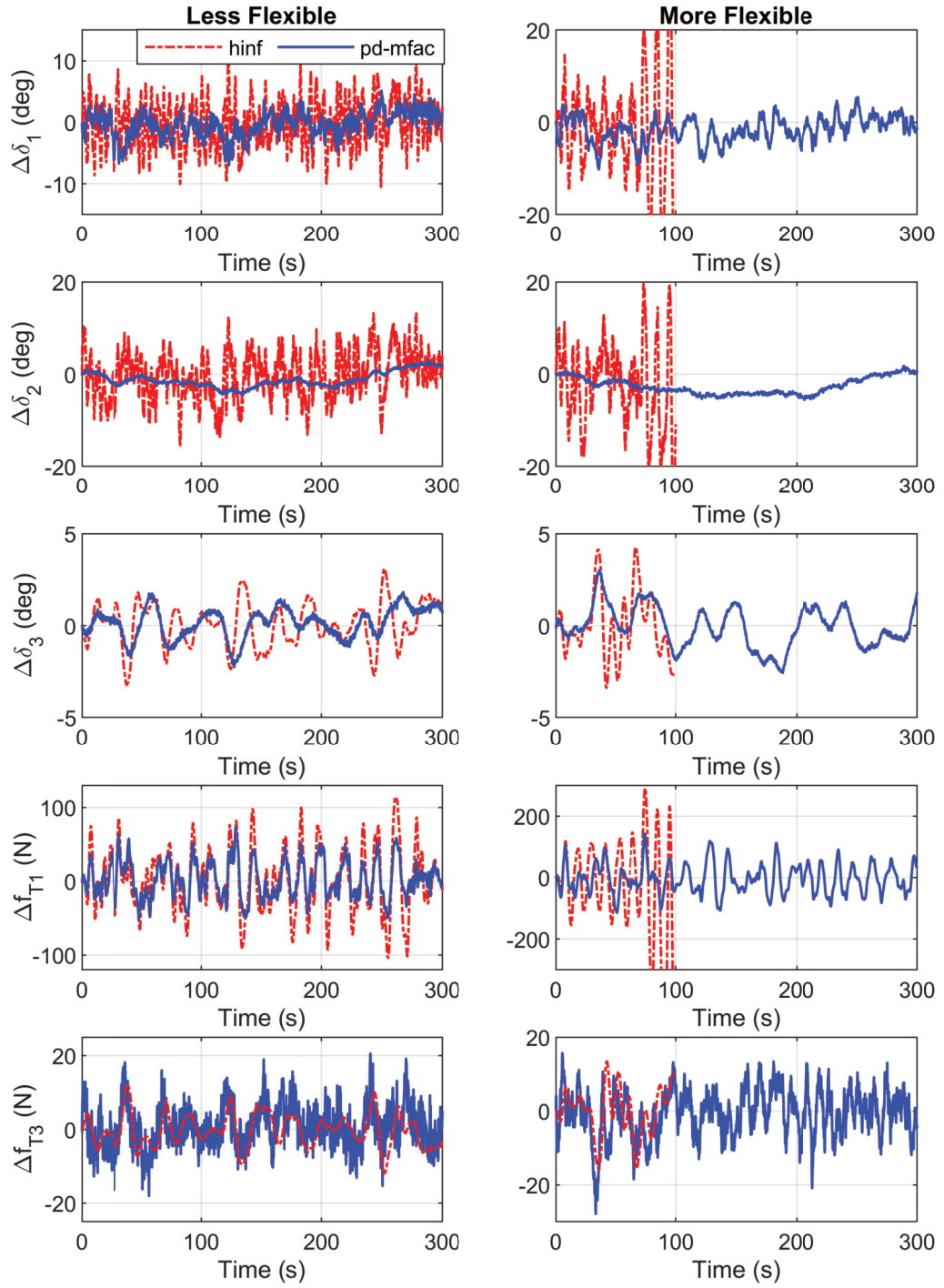


Figure 5.12: Time histories of control inputs with the data-driven and the H_∞ control systems in turbulence, based on two very flexible configurations with varying bending stiffness.

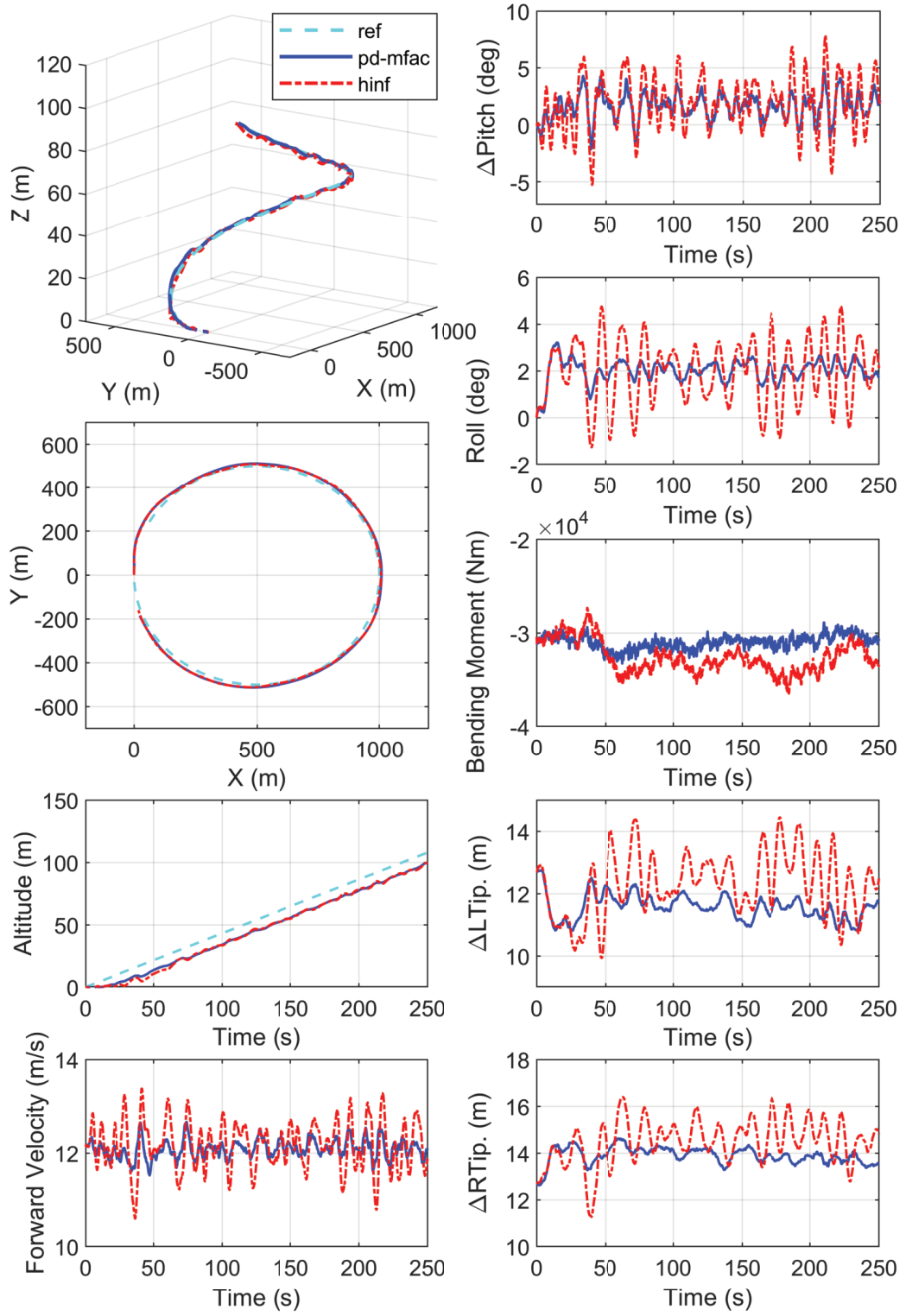


Figure 5.13: Time histories of the responses with the data-driven control system for path-following in the presence of wind turbulence.

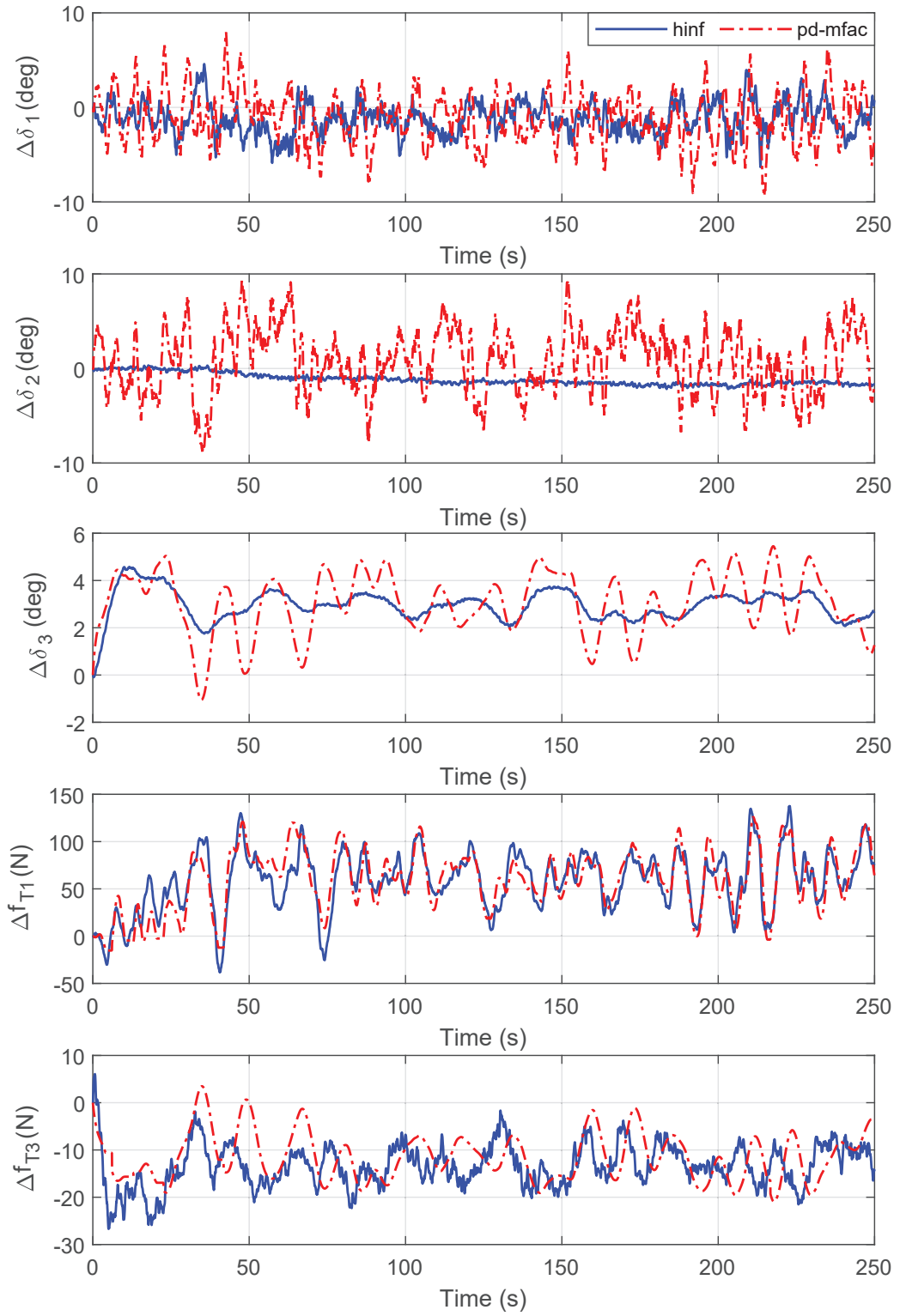


Figure 5.14: Time histories of the control actions with the data-driven control system for path-following in the presence of wind turbulence.

Furthermore, a modal contribution analysis reveals that the rigid-body modes are properly regulated to achieve satisfactory path-following in three dimensions, and the dominant flexible modes are all suppressed in disturbance rejection. Fig. 5.15 and Fig. 5.16 give examples of the modal amplitudes of the rigid-body modes and the first five dominant flexible modes in the above simulations, respectively. $q_{1j\{j=1\sim6\}}$ are the amplitudes of the rigid-body modes (lateral, forward, vertical translation, and pitch, roll, yaw rotation), while $q_{ij\{i=1\sim2, j=7\sim11\}}$ are those of the 1st symmetric out-of-plane bending, the 1st asymmetric out-of-plane bending, the 1st symmetric in-plane bending, the 1st asymmetric in-plane bending and the 2nd symmetric out-of-plane bending (with $i = 1$ for kinetic energy and $i = 2$ for strain energy of mode j), respectively.

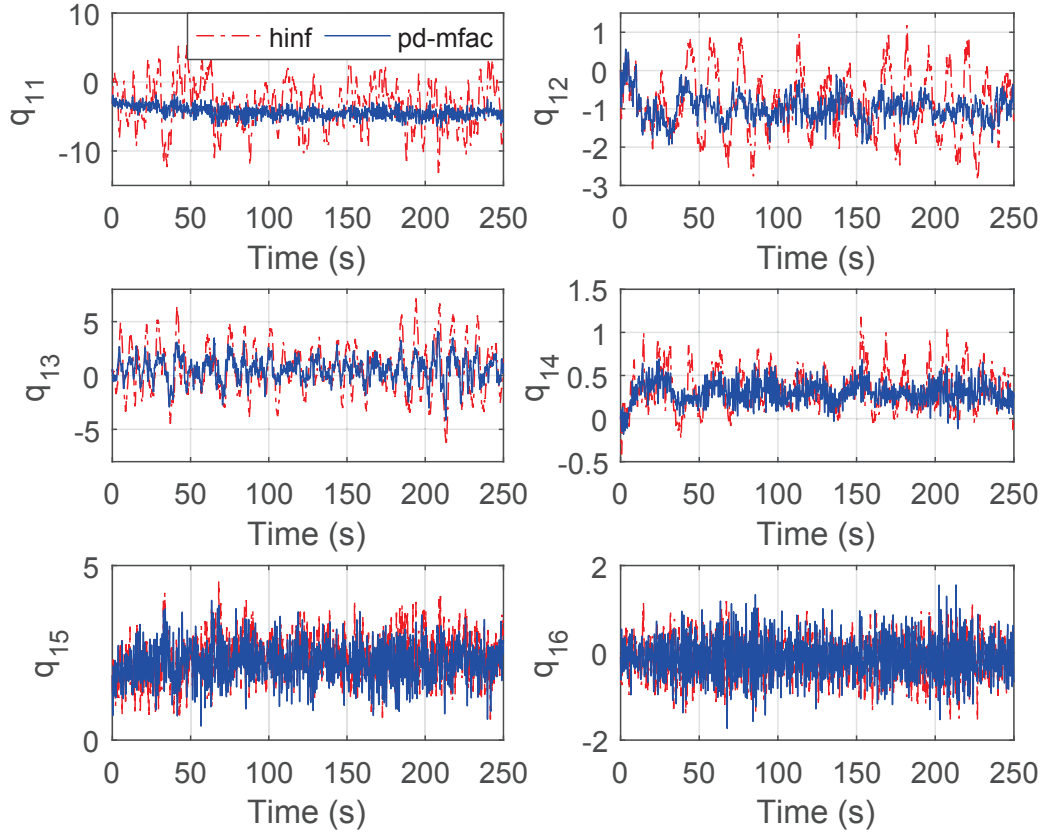


Figure 5.15: Modal amplitudes of the rigid-body modes with the data-driven control systems for path-following in presence of wind turbulence.

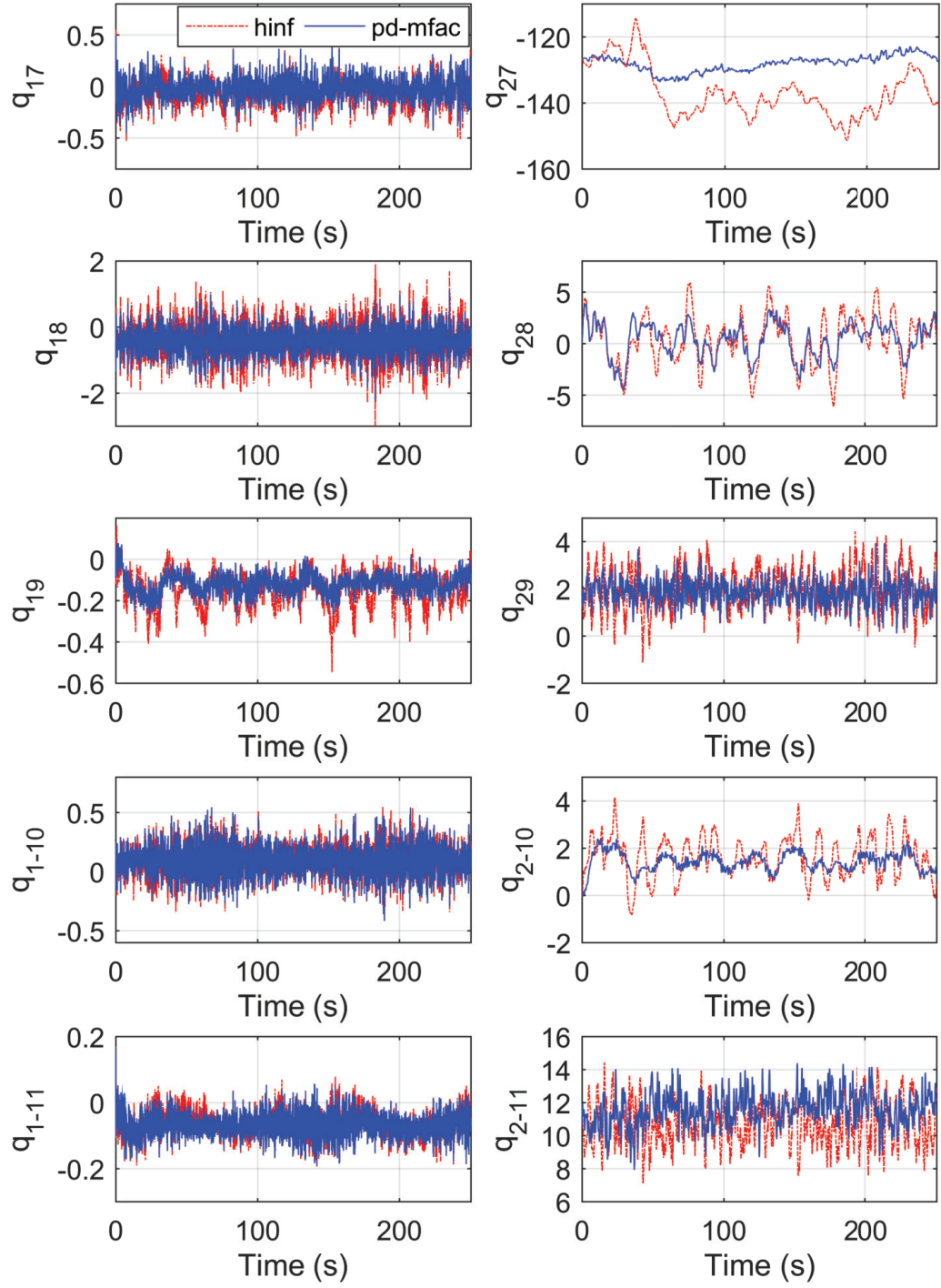


Figure 5.16: Modal amplitudes of the first five dominant flexible modes with the data-driven control systems for path-following in presence of wind turbulence.

5.5 Conclusions

This chapter investigated the aeroelastic and trajectory control of a very flexible flying wing using the Model-Free Adaptive Control (MFAC) scheme. A cascaded proportional-derivative MFAC (PD-MFAC) approach has been proposed to accommodate the MFAC scheme in a flight control problem, which also offers better control performance than the original MFAC approach by introducing necessary damping effects. The control system was designed based on a dynamic linearisation data model built from history input/output data and online updated the adaptive control law, without requiring explicit mathematical modelling of the aircraft. Simulation results showed that the proposed PD-MFAC control system was able to regulate all the rigid-body and flexible modes to achieve desirable gust load alleviation response and efficient path-following in three dimensions. The PD-MFAC control system also showed better effectiveness and robustness (against disturbance rejection and modelling uncertainties) compared to a baseline H_∞ control system. These results demonstrated the potential of the data-driven MFAC approach in addressing the flight control problem for VFA whose control design model usually has very high dimensions and/or big modelling errors when employing conventional model-based control design. However, it is important to note that strong assumptions were made to apply the MFAC scheme to address the flight control problem of VFA in this work, these assumptions must be theoretically justified in future studies, especially when using the MFAC approach in practice.

Chapter 6

Conclusions and Future Work

6.1 Conclusions

In this thesis, we have investigated the flight control of very flexible aircraft (VFA) in the scenarios of trajectory tracking and autonomous landing. Chapter 2 briefly summarized the aeroelastic modelling of a very flexible flying wing which was developed in the work of [19]. Key results of the modal aeroservoelastic formulation and using nonlinear model reduction to obtain an appropriate reduced-order model for control synthesis were presented. Chapter 3 and Chapter 4 investigated the aeroelastic and trajectory control, and the autonomous landing control for the very flexible flying wing model, respectively, using conventional model-based control methods, while Chapter 5 investigated the aeroelastic and trajectory control using data-driven control methods. The work of Chapters 3~5 is summarized in details as below.

Chapter 3 dealt with the combined aeroelastic and trajectory control of the very flexible flying wing in the presence of wind disturbance. Since VFA exhibit complex dynamics and are very sensitive to wind disturbance, it is crucial to guarantee robustness of the designed control system with respect to disturbance rejection. For this purpose, a two-loop robust control scheme based on the PI/LADRC and H_∞ control methods have been proposed, and the particle swarm optimization algorithm was employed to optimize the weighting parameters in the H_∞ control design to enhance robustness and effectiveness. The control design was based on a reduced-order linear model. Through simulation tests conducted on the full-order nonlinear model, the designed control system was shown to achieve good performance in aspects of trajectory tracking effectiveness and robustness against disturbance rejection. In the control design, the rigid-body degrees of freedom were approximated by taking sensor measurements (e.g. position, attitude angle, velocity) at the centre of the

wing, while the root bending moment which is utilized to control the first symmetric bending degree of freedom was assumed directly available to the control system. In future studies, it is necessary to investigate the optimisation of sensor configuration to obtain such information. Moreover, the very flexible flying wing model used in this work used the same conventional set of flap/thrust control actions as in [19], the optimization of actuator configuration and the fault tolerant control regarding loss or malfunction of sensors/actuators are also worthy of further investigation.

Chapter 4 addressed the autonomous landing control of the very flexible flying wing in the presence of wind disturbance. The control design followed the two-loop control scheme proposed in Chapter 3, but extended the inner-loop H_∞ controller to incorporate Lidar wind measurements and employ H_∞ preview control. A Lidar simulator was developed to measure the wind disturbances at a distance in front of the aircraft, which were provided to the control system as prior knowledge. This enabled the control system to adjust the aircraft to a proper state in advance before the wind disturbances actually affect the aircraft, therefore improved the disturbance rejection performance. Simulation studies showed that the preview-based landing control system was able to land the aircraft safely and effectively in the presence of wind disturbance. Oscillations in the longitudinal and lateral variables were observed to be largely reduced by the preview-based landing control system compared to a baseline landing control system (without preview), which indicated better landing effectiveness and disturbance rejection performance. Modal analysis further validated these results from the perspective of modal energy contributions. The proposed design has demonstrated the potential of using short-range Lidar wind measurements and preview control scheme to benefit the autonomous landing of VFA in the presence of wind turbulence. Furthermore, the proposed method is not confined to the landing scenario but can be extended to benefit trajectory tracking problems.

Chapter 5 successfully used data-driven control methods to address the aeroelastic and trajectory control of the very flexible flying wing based on the Model-Free Adaptive Control (MFAC) scheme. A cascaded proportional-derivative MFAC (PD-MFAC) approach was proposed to accommodate the MFAC scheme in a flight control problem, which offered better control performance than the original MFAC approach by introducing necessary damping effects. The data-driven MFAC control system was designed based on a dynamic linearisation data model which was built by directly using the history input/output data, without requiring any explicit information on the modelling of the aircraft, thus avoided the issues of modelling uncertainties and unmodeled dynamics. Simulation results showed that the pro-

posed PD-MFAC control system was able to regulate all the rigid-body and flexible modes to achieve desirable gust load alleviation response and efficient path-following in three dimensions. Compared with a baseline H_∞ control system, the proposed data-driven flight control system also achieved better effectiveness and robustness against disturbance rejection and modelling uncertainties. These results demonstrated the potential of data-driven scheme in addressing the flight control problem for VFA whose control design model usually has very high dimensions and/or big modelling errors when employing conventional model-based control design. However, it is important to note that strong assumptions were made to apply the MFAC scheme to address the flight control problem of VFA in this work, these assumptions must be theoretically justified in future studies, especially when using the MFAC approach in practice.

6.2 Future Work

The recommendations for future studies are as below.

(1) Optimisation of sensor configuration

The root bending moment was utilized in this work as feedback to control the first symmetric bending degree of freedom which plays a significant role in shaping the elastic mode. This work simply assumed the root bending moment was directly available, without considering the optimisation of sensor configuration to obtain such information. It is necessary to investigate the optimisation of sensor configuration, for example, the types of sensors (e.g. inertial measurement unit, accelerometer, strain gauge, etc.), the corresponding numbers and locations, etc., to reconstruct the actual shape of the wing.

(2) Optimisation of actuator configuration

This work followed the same definition of flap/thrust control actions as in [19] to control the rigid-body degrees of freedom and the structural bending degrees of freedom. It would be interesting to investigate the optimisation of actuator configuration for this particular flying wing model, for example, the number of flaps or motors, the size and location of flap surfaces, etc., to provide optimal control authorities. Given the actual sensor/actuator configurations, the fault tolerant control regarding the loss/malfunction of sensors/actuators is also an interesting topic.

(3) Reducing the conservativeness of H_∞ control design to modeling uncertainties

Standard H_∞ synthesis aims to minimize the influence of uncertainty in the

controlled plant, but the uncertainty to be dealt with is assumed to be unstructured, which means no particular description of the uncertainty is specified. However, in most practical problems, the uncertainty involved is structured (also called parametric uncertainty, for example, uncertainty in parameters of the controlled plant that are not known exactly or even time-variant, or uncertainty resulted from neglecting high-frequency dynamics due to system order reduction, etc.). This may cause the designed H_∞ controller to be conservative and limit the performance of the closed-loop system. Given appropriate uncertainty description for the very flexible aircraft, the μ synthesis method (which minimizes the upper bound of the structure singular value μ , i.e. the smallest H_∞ norm γ , such that the corresponding input-output gain of the closed-loop system stays below γ for all modelled uncertainty up to size $1/\gamma$) can be considered in future studies to reduce the conservativeness of H_∞ control design with respect to uncertainties and obtain a possibly more robust controller.

(4) Preview control with Lidar measurements under wind turbulence with large spatial velocity fluctuations

In Chapter 4, the spatial velocity fluctuations of wind turbulence was assumed to be small along the airframe, one Lidar system was used to measure the three-dimensional components of the wind velocity. However, the large wing span of the aircraft may be exposed to wind turbulence under large velocity fluctuations at different locations along the airframe. Multiple Lidar systems might be needed to measure the wind velocity at different regions to determine the actual wind speed distribution. Thus, it is necessary to investigate the corresponding preview control scheme with multiple Lidar measurement in future studies.

(5) Flight control of VFA using reinforcement learning

In Chapter 5, strong assumptions were made to apply the MFAC scheme to address the flight control problem of VFA. It would be of significance to study the application of other data-driven control methods to relax these assumptions and enable the control system with learning abilities to improve control performance. The reinforcement learning method might be a good candidate, which allows for the design of feedback controllers with combined features of adaptive control and optimal control. The controller features an actor-critic structure which can learn the optimal solutions by solving the Hamilton-Jacobi-Bellman equations online, without knowing full system dynamics. It might be also necessary to consider combining model-based and data-driven control methods to further improve control performance.

(6) Build a prototype flexible aircraft and carry out experimental flight tests to validate the modelling methods and control design.

Appendix A

Based on the work of [19], the explicit form of the aerodynamic forces on a 2D aerofoil section under linear assumptions are expressed by the local velocities used in the beam equations (2.1) (i.e. $\mathbf{x}_1 = [v_1, v_2, v_3, w_1, w_2, w_3]^\top$) as

$$\begin{aligned}
L_{AE} &= \frac{1}{2}\rho v_2 \cdot 2b \cdot (C_{L\alpha}(\frac{1}{2}(-v_3 + b(1-a)w_1) + \frac{1}{2}V_\infty \sum_{j=1}^{N_{AE}} 2A_j^{AE}b_j^{AE}\lambda_j) \\
&\quad + V_\infty(C_{L0} + C_{L\delta}\delta)) - \frac{1}{2}\rho v_3 V_\infty \cdot 2b \cdot C_{D0}, \\
D_{AE} &= -\frac{1}{2}\rho v_3 \cdot 2b \cdot (C_{L\alpha}(\frac{1}{2}(-v_3 + b(1-a)w_1) + \frac{1}{2}V_\infty \sum_{j=1}^{N_{AE}} 2A_j^{AE}b_j^{AE}\lambda_j) \\
&\quad + V_\infty(C_{L0} + C_{L\delta}\delta)) - \frac{1}{2}\rho v_2 V_\infty \cdot 2b \cdot C_{D0}, \\
M_{AE} &= \frac{1}{2}\rho V_\infty \cdot 2b \cdot 2b(-C_{L\alpha}\frac{b}{8}w_1 + V_\infty(C_{M0} + C_{M\delta}\delta)) \\
&\quad + ab\frac{1}{2}\rho V_\infty \cdot 2b(C_{L\alpha}(\frac{1}{2}(-v_3 + b(1-a)w_1) + \frac{1}{2}V_\infty \sum_{j=1}^{N_{AE}} 2A_j^{AE}b_j^{AE}\lambda_j) \\
&\quad + V_\infty(C_{L0} + C_{L\delta}\delta)),
\end{aligned} \tag{A.1}$$

where L_{AE} , D_{AE} , M_{AE} are the lift, drag and moment, respectively. ρ is the air density, b is the semi-chord of the aerofoil, a is the normalised distance of aerodynamic centre to structural centre, V_∞ is the free-stream velocity. C_{L0} , $C_{L\alpha}$, C_{D0} , C_{M0} are the steady-state lift coefficient at zero angle of attack, the slope of steady-state lift coefficient with respect to angle of attack, the steady-state drag and moment coefficient, respectively. $C_{L\delta}$, $C_{M\delta}$ are the slope of steady-state lift and moment coefficient with respect to the control surface deflections δ , respectively. N_{AE} is the number of aerodynamic states used in the unsteady aerofoil theory, A_j^{AE} and b_j^{AE} are the rational function approximation coefficients to the Theodorsen's function. The aerodynamic state λ_j is expressed as

$$\dot{\lambda}_j + \frac{b_j^{AE}V_\infty}{b}\lambda_j = -\frac{1}{b}v_3 + (1-a)w_1. \tag{A.2}$$

The above formulations can be written in a compact form as

$$\begin{aligned}\mathbf{f}_e &= \rho b(\mathcal{A}_1(\mathbf{x}_1)\mathbf{x}_1 + V_\infty \mathcal{A}_2 \mathbf{x}_1 \cdot \sum_{j=1}^{N_{AE}} 2A_j^{AE} b_j^{AE} \lambda_j + \mathcal{A}_3(\mathbf{x}_1)\mathbf{x}_1 \cdot \delta), \\ \dot{\lambda}_j &= k_{AE}^\top \mathbf{x}_1 - \frac{b_j^{AE} V_\infty}{b} \lambda_j,\end{aligned}\tag{A.3}$$

where $\mathbf{f}_e = [0 \quad D_{AE} \quad L_{AE} \quad M_{AE} \quad 0 \quad 0]$, $k_{AE}^\top = [0 \quad 0 \quad -1/b \quad (1-a) \quad 0 \quad 0]$ and the linear operators being

$$\mathcal{A}_1(\mathbf{x}_1) = \begin{pmatrix} 0 & 0 & 0 & 0 & 0 & 0 \\ 0 & -C_{D0}v_2 & \frac{C_{L\alpha}}{2}v_3 - C_{L0}v_2 & -b(1-a)\frac{C_{L\alpha}}{2}v_3 & 0 & 0 \\ 0 & C_{L0}v_2 - (\frac{C_{L\alpha}}{2} + C_{D0})v_3 & 0 & b(1-a)\frac{C_{L\alpha}}{2}v_2 & 0 & 0 \\ 0 & b((2C_{M0} + aC_{L0})v_2 - a\frac{C_{L\alpha}}{2}v_3) & 0 & b^2(a - a^2 - \frac{1}{2})\frac{C_{L\alpha}}{2}v_2 & 0 & 0 \\ 0 & 0 & 0 & 0 & 0 & 0 \\ 0 & 0 & 0 & 0 & 0 & 0 \end{pmatrix},\tag{A.4}$$

$$\mathcal{A}_2 = \begin{pmatrix} 0 & 0 & 0 & 0 & 0 & 0 \\ 0 & 0 & -1 & 0 & 0 & 0 \\ 0 & 1 & 0 & 0 & 0 & 0 \\ 0 & ab & 0 & 0 & 0 & 0 \\ 0 & 0 & 0 & 0 & 0 & 0 \\ 0 & 0 & 0 & 0 & 0 & 0 \end{pmatrix},\tag{A.5}$$

$$\mathcal{A}_3(\mathbf{x}_1) = \begin{pmatrix} 0 & 0 & 0 & 0 & 0 & 0 \\ 0 & 0 & -C_{L\delta}v_2 & 0 & 0 & 0 \\ 0 & C_{L\delta}v_2 & 0 & 0 & 0 & 0 \\ 0 & (abC_{L\delta} + 2bC_{M\delta})v_2 & 0 & 0 & 0 & 0 \\ 0 & 0 & 0 & 0 & 0 & 0 \\ 0 & 0 & 0 & 0 & 0 & 0 \end{pmatrix}.\tag{A.6}$$

Subsequently, by inserting (2.3) into the beam equations (2.1) and the aerodynamic force/moment equations (A.3), the modal aeroservoelastic formulations (2.4) are eventually derived. For example, by inserting (2.3) into (A.3), we have

$$\begin{aligned}
\mathbf{f}_e &= \rho b (\mathcal{A}_1 (\sum_{k=1}^{\infty} \phi_{1k} q_{1k}) \sum_{l=1}^{\infty} \phi_{1l} q_{1l} + V_{\infty} \mathcal{A}_2 \sum_{k=1}^{\infty} \phi_{1k} q_{1k} \cdot \sum_{j=1}^{N_{AE}} 2A_j^{AE} b_j^{AE} \lambda_j \\
&\quad + \mathcal{A}_3 (\sum_{k=1}^{\infty} \phi_{1k} q_{1k}) \sum_{l=1}^{\infty} \phi_{1l} q_{1l} \cdot \delta), \\
\dot{\lambda}_j &= k_{AE}^T \sum_{k=1}^{\infty} \phi_{1k} q_{1k} - \frac{b_j^{AE} V_{\infty}}{b} \lambda_j,
\end{aligned} \tag{A.7}$$

with λ_j being split into components corresponding to each velocity mode as

$$\lambda_j = \sum_{k=1}^{\infty} k_{AE}^T \phi_{1k} q_{a,jk}. \tag{A.8}$$

Appendix B

The guidance algorithm used in Section 3.3.3 is based on the waypoint tracking mechanism proposed in [116], we now introduce relevant details for easy reference.

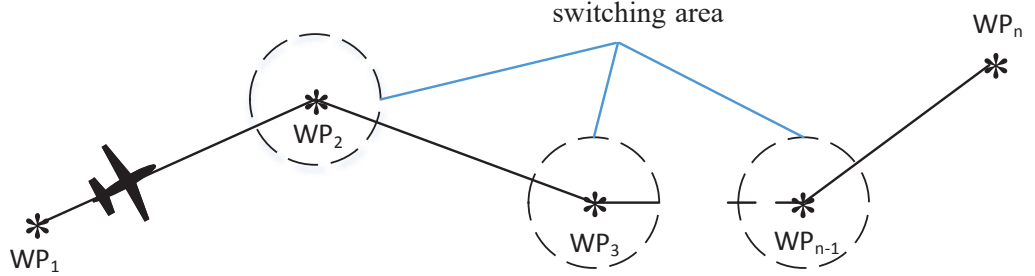


Figure 1: Illustration of the waypoint tracking.

As depicted in Fig. 1, the desired flight path is described by the connection of multiple waypoints (WP_1 to WP_n) which are defined by the altitude, longitude and latitude coordinates. The guidance algorithm aims to direct the aircraft to follow these waypoints in sequence using a waypoint switching strategy. We assume the aircraft is initially flying from WP_1 towards WP_2 , where WP_1 is denoted as the departure waypoint and WP_2 as the destination waypoint. We also define the distance between the aircraft's current position (which is sensed by onboard GPS sensors) and the destination waypoint as the "distance to travel" denoted by D_{wp} . As the aircraft approaches to WP_2 , if D_{wp} is less than a given value, the aircraft enters the switching area, in which WP_2 becomes the new departure waypoint and WP_3 becomes the new destination waypoint. The guidance algorithm then directs the aircraft to fly from WP_2 towards WP_3 and follows the same switching mechanism until the aircraft reaches the final destination waypoint WP_n . During this process, the waypoint tracking algorithm generates reference commands and necessary guidance information to the control system to achieve altitude tracking in the vertical plane and to keep the aircraft aligned with the straight line between the

departure and destination waypoint in the horizontal plane.

To perform such waypoint tracking, the "distance to travel" D_{wp} , the lateral displacement S and the lateral speed \dot{S} are required. The formulations of these variables are derived using the aircraft's current position and velocity, and the departure and destination waypoint information as below.

The lateral displacement S (see Fig. 3.5) is derived as

$$\left\{ \begin{array}{l} S = R_p \cdot \left(\frac{\pi}{2} - \arccos\left(\frac{\kappa_1 \times \kappa_0}{|\kappa_1 \times \kappa_0|} \cdot \kappa \right) \right) \\ R_p = R_c \cdot \left\{ 1 + \frac{E_D^2}{2} \cdot \left[\frac{1}{1 + (1 - E_D^2) \cdot \tan(L_{at})} - 1 \right] \right\} \\ \kappa_1 = [\cos(B_{EC1}) \cos(L_{ate}), \cos(B_{EC1}) \sin(L_{ate}), \sin(B_{EC1})]^\top \\ \kappa_0 = [\cos(B_{EC0}) \cos(L_{ats}), \cos(B_{EC0}) \sin(L_{ats}), \sin(B_{EC0})]^\top \\ \kappa = [\cos(B_{EC}) \cos(L_{at}), \cos(B_{EC}) \sin(L_{at}), \sin(B_{EC})]^\top \\ B_{EC} = \arctan\left(\left(\frac{H + R_d}{H + R_c}\right)^2 \cdot \tan(L_{at})\right) \\ B_{EC0} = \arctan\left(\left(\frac{H + R_d}{H + R_c}\right)^2 \cdot \tan(L_{ats})\right) \\ B_{EC1} = \arctan\left(\left(\frac{H + R_d}{H + R_c}\right)^2 \cdot \tan(L_{ate})\right) \end{array} \right. \quad (B.1)$$

in which $R_c \approx 6378137m$ is the Earth's equatorial radius, $R_d \approx 6356752m$ is the Earth's polar radius, $E_D \approx 0.0033523$ is the flattening of the Earth. L_{on}, L_{ons} and L_{one} are the longitude coordinate of the aircraft's current position, departure waypoint and destination waypoint, respectively. L_{at}, L_{ats} and L_{ate} are the latitude coordinate of the aircraft's current position, departure waypoint and destination waypoint, respectively. H is the altitude of the aircraft. The symbol " \times " denotes the cross product operator.

The lateral speed \dot{S} is derived as

$$\left\{ \begin{array}{l} \dot{S} = \begin{cases} V_{dn} \cdot \cos(\nu) - V_{de} \cdot \sin(\nu) & \text{if } L_{ate} < L_{ats} \\ V_{dn} \cdot \cos(\nu) + V_{de} \cdot \sin(\nu) & \text{if } L_{ate} > L_{ats} \end{cases} \\ \nu = \arccos\left(\frac{\kappa_4 \times \kappa_3}{|\kappa_4 \times \kappa_3|} \cdot \kappa_2\right) \\ \kappa_2 = [-\sin(L_{at}) \cos(L_{on}), -\sin(L_{at}) \sin(L_{on}), \cos(L_{at})]^\top \\ \kappa_3 = [\cos(L_{ats}) \cos(L_{ons}), \cos(L_{ats}) \sin(L_{ons}), \sin(L_{ats})]^\top \\ \kappa_4 = [\cos(L_{ate}) \cos(L_{one}), \cos(L_{ate}) \sin(L_{one}), \sin(L_{ate})]^\top \end{array} \right. \quad (\text{B.2})$$

where V_{dn} and V_{de} are the northern and eastern component of the ground speed, respectively, which can be obtained through the onboard GPS sensors.

The "distance to travel" D_{wp} is derived as

$$\left\{ \begin{array}{l} D_{wp} = \sqrt{\Delta x^2 + \Delta y^2} \\ \Delta x = R_p \cdot \cos(B_{EC1}) \cdot (L_{on} - L_{one}) \\ \Delta y = R_p \cdot (B_{EC} - B_{EC1}) \end{array} \right. \quad (\text{B.3})$$

where R_p , B_{EC} and B_{EC1} follow the definitions in (B.1).

Bibliography

- [1] K. P. Valavanis and G. J. Vachtsevanos, *Handbook of unmanned aerial vehicles*. Springer, 2015.
- [2] L. R. Newcome, *Unmanned aviation: a brief history of unmanned aerial vehicles*. American Institute of Aeronautics and Astronautics, 2004.
- [3] P. Oettershagen, A. Melzer, T. Mantel, K. Rudin, T. Stastny, B. Wawrzacz, T. Hinzmann, S. Leutenegger, K. Alexis, and R. Siegwart, “Design of small hand-launched solar-powered uavs: From concept study to a multi-day world endurance record flight,” *Journal of Field Robotics*, vol. 34, no. 7, pp. 1352–1377, 2017.
- [4] A. T. Klesh and P. T. Kabamba, “Solar-powered aircraft: Energy-optimal path planning and perpetual endurance,” *Journal of Guidance, Control, and Dynamics*, vol. 32, no. 4, pp. 1320–1329, 2009.
- [5] N. André, “Design of solar powered airplanes for continuous flight,” Ph.D. thesis, ETH Zurich, 2008.
- [6] D. Raymer, *Aircraft design: a conceptual approach*. American Institute of Aeronautics and Astronautics, 2018.
- [7] E. Livne and T. A. Weisshaar, “Aeroelasticity of nonconventional airplane configurations-past and future,” *Journal of Aircraft*, vol. 40, no. 6, pp. 1047–1065, 2003.
- [8] M. J. Patil, D. H. Hodges, and C. E. S. Cesnik, “Nonlinear aeroelasticity and flight dynamics of high-altitude long-endurance aircraft,” *Journal of Aircraft*, vol. 38, no. 1, pp. 88–94, 2001.
- [9] C. E. Cesnik, P. J. Senatore, W. Su, E. M. Atkins, and C. M. Shearer, “X-hale: A very flexible unmanned aerial vehicle for nonlinear aeroelastic tests,” *AIAA Journal*, vol. 50, no. 12, pp. 2820–2833, 2012.

- [10] G. Romeo, G. Frulla, and E. Cestino, “Design of a high-altitude long-endurance solar-powered unmanned air vehicle for multi-payload and operations,” *Proceedings of the Institution of Mechanical Engineers, Part G: Journal of Aerospace Engineering*, vol. 221, no. 2, pp. 199–216, 2007.
- [11] “FAI Record ID No. 16052,” *Fédération Aéronautique Internationale*, December 2012.
- [12] “FAI Record ID No. 7354,” *Fédération Aéronautique Internationale*, August 2001.
- [13] T. E. Noll, J. M. Brown, and M. E. Perez-Davis, “Investigation of the helios prototype aircraft mishap report,” *Technical report*, NASA, 2004.
- [14] A. Hern, “Facebook’s solar-powered drone under investigation after ‘accident’.” <https://www.theguardian.com/technology/2016/nov/22/facebook-solar-powered-aquila-drone-under-investigation>. The Guardian, December, 2017.
- [15] “Aviation accident final report, NTSB identification: DCA16CA197,” *National Transportation Safety Board*, June 2016.
- [16] W. Su and C. E. S. Cesnik, “Dynamic response of highly flexible flying wings,” *AIAA Journal*, vol. 49, no. 2, pp. 324–339, 2011.
- [17] M. J. Patil and D. H. Hodges, “Flight dynamics of highly flexible flying wings,” *Journal of Aircraft*, vol. 43, no. 6, pp. 1790–1799, 2006.
- [18] Z. Wang, P. C. Chen, D. D. Liu, and D. T. Mook, “Nonlinear-aerodynamics/nonlinear-structure interaction methodology for a high-altitude long-endurance wing,” *Journal of Aircraft*, vol. 47, no. 2, pp. 556–566, 2010.
- [19] Y. Wang, A. Wynn, and R. Palacios, “A nonlinear modal aeroservoelastic analysis framework for flexible aircraft,” *AIAA Journal*, vol. 54, no. 10, pp. 3075–3090, 2016.
- [20] R. Palacios, J. Murua, and R. Cook, “Structural and aerodynamic models in nonlinear flight dynamics of very flexible aircraft,” *AIAA Journal*, vol. 48, no. 11, pp. 2648–2659, 2010.
- [21] L. Meirovitch and I. Tuzcu, “Unified theory for the dynamics and control of maneuvering flexible aircraft,” *AIAA Journal*, vol. 42, no. 4, pp. 714–727, 2004.

- [22] H. Hesse and R. Palacios, “Consistent structural linearisation in flexible-body dynamics with large rigid-body motion,” *Computers & Structures*, vol. 110, pp. 1–14, 2012.
- [23] N. Nguyen and I. Tuzcu, “Flight dynamics of flexible aircraft with aeroelastic and inertial force interactions,” in *AIAA Atmospheric Flight Mechanics Conference*, (Chicago, Illinois, USA), August 2009.
- [24] C.-S. Chang, D. H. Hodges, and M. J. Patil, “Flight dynamics of highly flexible aircraft,” *Journal of Aircraft*, vol. 45, no. 2, pp. 538–545, 2008.
- [25] N. T. Nguyen, K. Reynolds, E. Ting, and N. Nguyen, “Distributed propulsion aircraft with aeroelastic wing shaping control for improved aerodynamic efficiency,” *Journal of Aircraft*, vol. 55, no. 3, pp. 1122–1140, 2017.
- [26] R. Palacios, Y. Wang, and M. Karpel, “Intrinsic models for nonlinear flexible-aircraft dynamics using industrial finite-element and loads packages,” in *53rd AIAA/ASME/ASCE/AHS/ASC Structures, Structural Dynamics and Materials Conference 20th AIAA/ASME/AHS Adaptive Structures Conference 14th AIAA*, (Honolulu, Hawaii, USA), April 2012.
- [27] Y. Wang, A. Wynn, and R. Palacios, “Nonlinear aeroelastic control of very flexible aircraft using model updating,” *Journal of Aircraft*, vol. 55, no. 4, pp. 1551–1563, 2017.
- [28] W. Shyy, H. Aono, S. K. Chimakurthi, P. Trizila, C.-K. Kang, C. E. Cesnik, and H. Liu, “Recent progress in flapping wing aerodynamics and aeroelasticity,” *Progress in Aerospace Sciences*, vol. 46, no. 7, pp. 284–327, 2010.
- [29] M. Richter and M. Patil, “Influence of wing flexibility on the stability of flapping flight,” in *AIAA Atmospheric Flight Mechanics Conference*, (Toronto, Ontario, Canada), p. August, 2010.
- [30] K. Senda, T. Obara, M. Kitamura, N. Yokoyama, N. Hirai, and M. Iima, “Effects of structural flexibility of wings in flapping flight of butterfly,” *Bioinspiration & Biomimetics*, vol. 7, no. 2, pp. 1–26, 2012.
- [31] A. Gogulapati, P. P. Friedmann, E. Kheng, and W. Shyy, “Approximate aeroelastic modeling of flapping wings in hover,” *AIAA Journal*, vol. 51, no. 3, pp. 567–583, 2013.

- [32] S. Na, L. Librescu, M.-H. Kim, I.-J. Jeong, and P. Marzocca, “Aeroelastic response of flapped-wing systems using robust estimation control methodology,” *Journal of Guidance, Control, and Dynamics*, vol. 29, no. 1, pp. 199–202, 2006.
- [33] B. F. Ng, R. Palacios, and J. M. R. Graham, “Model-based aeroelastic analysis and blade load alleviation of offshore wind turbines,” *International Journal of Control*, vol. 90, no. 1, pp. 15–36, 2017.
- [34] V. V. Volovoi, D. H. Hodges, C. E. Cesnik, and B. Popescu, “Assessment of beam modeling methods for rotor blade applications,” *Mathematical and Computer Modelling*, vol. 33, no. 10-11, pp. 1099–1112, 2001.
- [35] B. F. Ng, H. Hesse, R. Palacios, J. M. R. Graham, and E. C. Kerrigan, “Aeroservoelastic state-space vortex lattice modeling and load alleviation of wind turbine blades,” *Wind Energy*, vol. 18, no. 7, pp. 1317–1331, 2015.
- [36] L. Wang, X. Liu, and A. Kolios, “State of the art in the aeroelasticity of wind turbine blades: Aeroelastic modelling,” *Renewable and Sustainable Energy Reviews*, vol. 64, pp. 195–210, 2016.
- [37] Y. Wang, W. Andrew, and R. Palacios, “Nonlinear model reduction for aeroelastic control of flexible aircraft described by large finite-element models,” in *55th AIAA/ASME/ASCE/AHS/ASC Structures, Structural Dynamics, and Materials Conference*, (National Harbor, Maryland, USA), January 2014.
- [38] M. Goland, “The flutter of a uniform cantilever wing,” *Journal of Applied Mechanics-Transactions of the Asme*, vol. 12, no. 4, pp. A197–A208, 1945.
- [39] D. Tang and E. H. Dowell, “Experimental and theoretical study on aeroelastic response of high-aspect-ratio wings,” *AIAA Journal*, vol. 39, no. 8, pp. 1430–1441, 2001.
- [40] T. Belytschko, W. K. Liu, B. Moran, and K. Elkhodary, *Nonlinear finite elements for continua and structures*. John wiley & sons, 2013.
- [41] R. E. Gordnier and R. Fithen, “Coupling of a nonlinear finite element structural method with a navier–stokes solver,” *Computers & structures*, vol. 81, no. 2, pp. 75–89, 2003.
- [42] L. Demasi and E. Livne, “Dynamic aeroelasticity of structurally nonlinear configurations using linear modally reduced aerodynamic generalized forces,” *AIAA Journal*, vol. 47, no. 1, pp. 70–90, 2009.

- [43] D. Tang, H. Yamamoto, and E. Dowell, “Flutter and limit cycle oscillations of two-dimensional panels in three-dimensional axial flow,” *Journal of Fluids and Structures*, vol. 17, no. 2, pp. 225–242, 2003.
- [44] D. H. Hodges, “Geometrically exact, intrinsic theory for dynamics of curved and twisted anisotropic beams,” *AIAA Journal*, vol. 41, no. 6, pp. 1131–1137, 2003.
- [45] D. H. Hodges, *Nonlinear composite beam theory*. American Institute of Aeronautics and Astronautics, 2006.
- [46] P. Cartraud and T. Messenger, “Computational homogenization of periodic beam-like structures,” *International Journal of Solids and Structures*, vol. 43, no. 3-4, pp. 686–696, 2006.
- [47] J. Dizy, R. Palacios, and S. T. Pinho, “Homogenisation of slender periodic composite structures,” *International Journal of Solids and Structures*, vol. 50, no. 9, pp. 1473–1481, 2013.
- [48] P. F. Pai, *Highly flexible structures: modeling, computation, and experimentation*. American Institute of Aeronautics and Astronautics, 2007.
- [49] R. J. Simpson and R. Palacios, “Numerical aspects of nonlinear flexible aircraft flight dynamics modeling,” in *54th AIAA/ASME/ASCE/AHS/ASC Structures, Structural Dynamics, and Materials Conference*, (Boston, Massachusetts, USA), April 2013.
- [50] J. Murua, H. Hesse, R. Palacios, and J. M. R. Graham, “Stability and open-loop dynamics of very flexible aircraft including free-wake effects,” in *52nd AIAA/ASME/ASCE/AHS/ASC Structures, Structural Dynamics and Materials Conference 19th AIAA/ASME/AHS Adaptive Structures Conference 13t*, (Denver, Colorado, USA), April 2011.
- [51] J. Murua, R. Palacios, and J. M. R. Graham, “Assessment of wake-tail interference effects on the dynamics of flexible aircraft,” *AIAA Journal*, vol. 50, no. 7, pp. 1575–1585, 2012.
- [52] M. Gams, I. Planinc, and M. Saje, “The strain-based beam finite elements in multibody dynamics,” *Journal of sound and vibration*, vol. 305, no. 1-2, pp. 194–210, 2007.

- [53] W. Su and C. E. Cesnik, “Strain-based geometrically nonlinear beam formulation for modeling very flexible aircraft,” *International Journal of Solids and Structures*, vol. 48, no. 16-17, pp. 2349–2360, 2011.
- [54] W. Su and C. E. Cesnik, “Strain-based analysis for geometrically nonlinear beams: a modal approach,” *Journal of Aircraft*, vol. 51, no. 3, pp. 890–903, 2014.
- [55] D. H. Hodges, “A mixed variational formulation based on exact intrinsic equations for dynamics of moving beams,” *International journal of solids and structures*, vol. 26, no. 11, pp. 1253–1273, 1990.
- [56] M. J. Patil, D. H. Hodges, and C. E. Cesnik, “Limit-cycle oscillations in high-aspect-ratio wings,” *Journal of fluids and structures*, vol. 15, no. 1, pp. 107–132, 2001.
- [57] J. A. Garcia, “Numerical investigation of nonlinear aeroelastic effects on flexible high-aspect-ratio wings,” *Journal of Aircraft*, vol. 42, no. 4, pp. 1025–1036, 2005.
- [58] J. J. McNamara and P. P. Friedmann, “Flutter boundary identification for time-domain computational aeroelasticity,” *AIAA journal*, vol. 45, no. 7, pp. 1546–1555, 2007.
- [59] R. Palacios and C. Cesnik, “Static nonlinear aeroelasticity of flexible slender wings in compressible flow,” in *46th AIAA/ASME/ASCE/AHS/ASC Structures, Structural Dynamics and Materials Conference*, (Austin, Texas, USA), April 2005.
- [60] J. Katz and A. Plotkin, *Low-speed aerodynamics*, vol. 13. Cambridge university press, 2001.
- [61] J. Murua, R. Palacios, and J. M. R. Graham, “Applications of the unsteady vortex-lattice method in aircraft aeroelasticity and flight dynamics,” *Progress in Aerospace Sciences*, vol. 55, pp. 46–72, 2012.
- [62] H. Hesse and R. Palacios, “Reduced-order aeroelastic models for dynamics of maneuvering flexible aircraft,” *AIAA Journal*, vol. 52, no. 8, pp. 1717–1732, 2014.
- [63] R. J. Simpson, R. Palacios, and J. Murua, “Induced-drag calculations in the unsteady vortex lattice method,” *AIAA Journal*, vol. 51, no. 7, pp. 1775–1779, 2013.

- [64] Z. Zhao and G. Ren, “Multibody dynamic approach of flight dynamics and nonlinear aeroelasticity of flexible aircraft,” *AIAA Journal*, vol. 49, no. 1, pp. 41–54, 2011.
- [65] C. M. Shearer and C. E. Cesnik, “Nonlinear flight dynamics of very flexible aircraft,” *Journal of Aircraft*, vol. 44, no. 5, pp. 1528–1545, 2007.
- [66] C. M. Shearer and C. E. S. Cesnik, “Trajectory control for very flexible aircraft,” *Journal of Guidance, Control, and Dynamics*, vol. 31, no. 2, pp. 340–357, 2008.
- [67] W. Su and C. E. Cesnik, “Nonlinear aeroelasticity of a very flexible blended-wing-body aircraft,” *Journal of Aircraft*, vol. 47, no. 5, pp. 1539–1553, 2010.
- [68] M. Dillsaver, C. Cesnik, and I. Kolmanovsky, “Gust load alleviation control for very flexible aircraft,” in *AIAA Atmospheric Flight Mechanics Conference*, (Portland, Oregon, USA), August 2011.
- [69] M. Dillsaver, C. Cesnik, and I. Kolmanovsky, “Gust response sensitivity characteristics of very flexible aircraft,” in *AIAA Atmospheric Flight Mechanics Conference*, (Minneapolis, Minnesota, USA), August 2012.
- [70] C. E. S. Cesnik, P. J. Senatore, W. Su, E. M. Atkins, and C. M. Shearer, “X-hale: A very flexible unmanned aerial vehicle for nonlinear aeroelastic tests,” *AIAA Journal*, vol. 50, no. 12, pp. 2820–2833, 2012.
- [71] J. R. Jones and C. E. Cesnik, “Preliminary flight test correlations of the x-hale aeroelastic experiment,” *The Aeronautical Journal*, vol. 119, no. 1217, pp. 855–870, 2015.
- [72] H. Hesse and R. Palacios, “Dynamic load alleviation in wake vortex encounters,” *Journal of Guidance, Control, and Dynamics*, vol. 39, no. 4, pp. 801–813, 2016.
- [73] A. del Carre, A. Muñoz-Simón, N. Goizueta, and R. Palacios, “Sharpy: A dynamic aeroelastic simulation toolbox for very flexible aircraft and wind turbines,” *Journal of Open Source Software*, vol. 4, no. 44, p. 1885, 2019.
- [74] Y. Wang, R. Palacios, and A. Wynn, “A method for normal-mode-based model reduction in nonlinear dynamics of slender structures,” *Computers & Structures*, vol. 159, pp. 26–40, 2015.

- [75] Q. Hu, Z. Wang, and H. Gao, "Sliding mode and shaped input vibration control of flexible systems," *IEEE Transactions on Aerospace and Electronic systems*, vol. 44, no. 2, pp. 503–519, 2008.
- [76] C. Zhong, Z. Chen, and Y. Guo, "Attitude control for flexible spacecraft with disturbance rejection," *IEEE Transactions on Aerospace and Electronic Systems*, vol. 53, no. 1, pp. 101–110, 2017.
- [77] S. Di Gennaro, "Output stabilization of flexible spacecraft with active vibration suppression," *IEEE Transactions on Aerospace and Electronic systems*, vol. 39, no. 3, pp. 747–759, 2003.
- [78] S. Ding and W. X. Zheng, "Nonsmooth attitude stabilization of a flexible spacecraft," *IEEE Transactions on Aerospace and Electronic Systems*, vol. 50, no. 2, pp. 1163–1181, 2014.
- [79] R. G. Cook, R. Palacios, and P. Goulart, "Robust gust alleviation and stabilization of very flexible aircraft," *AIAA Journal*, vol. 51, no. 2, pp. 330–340, 2013.
- [80] B. Moore, "Principal component analysis in linear systems: Controllability, observability, and model reduction," *IEEE transactions on automatic control*, vol. 26, no. 1, pp. 17–32, 1981.
- [81] H. Kwakernaak and R. Sivan, *Linear optimal control systems*. Wiley, 1972.
- [82] K. Willcox and J. Peraire, "Balanced model reduction via the proper orthogonal decomposition," *AIAA Journal*, vol. 40, no. 11, pp. 2323–2330, 2002.
- [83] L. Demasi and E. Livne, "Aeroelastic coupling of geometrically nonlinear structures and linear unsteady aerodynamics: two formulations," *Journal of Fluids and Structures*, vol. 25, no. 5, pp. 918–935, 2009.
- [84] F. Silvestre and P. Paglione, "Dynamics and control of a flexible aircraft," in *AIAA Atmospheric Flight Mechanics Conference and Exhibit*, (Honolulu, Hawaii, USA), August 2008.
- [85] N. Aouf, B. Boulet, and R. Botez, "H2 and h-inf optimal gust load alleviation for a flexible aircraft," in *American Control Conference*, (Chicago, Illinois, USA), June 2000.

- [86] D. Alazard, “Robust h design for lateral flight control of highly flexible aircraft,” *Journal of guidance, control, and dynamics*, vol. 25, no. 3, pp. 502–509, 2002.
- [87] T. Gibson, A. Annaswamy, and E. Lavretsky, “Modeling for control of very flexible aircraft,” in *AIAA Guidance, Navigation, and Control Conference*, (Portland, Oregon, USA), August 2011.
- [88] F. Allgöwer and A. Zheng, *Nonlinear model predictive control*. Birkhäuser, 2012.
- [89] J. A. Rossiter, *Model-based predictive control: a practical approach*. CRC press, 2017.
- [90] S. Haghghat, H. H. Liu, and J. R. Martins, “Model-predictive gust load alleviation controller for a highly flexible aircraft,” *Journal of Guidance, Control and Dynamics*, vol. 35, no. 6, pp. 1751–1766, 2012.
- [91] R. J. Simpson, R. Palacios, H. Hesse, and P. Goulart, “Predictive control for alleviation of gust loads on very flexible aircraft,” in *55th AIAA/ASME/ASCE/AHS/ASC Structures, Structural Dynamics, and Materials Conference*, (National Harbor, Maryland, USA), January 2014.
- [92] H. Giessler, M. Kopf, P. Varutti, T. Faulwasser, and R. Findeisen, “Model predictive control for gust load alleviation,” *IFAC Proceedings Volumes*, vol. 45, no. 17, pp. 27–32, 2012.
- [93] X. Liu, Q. Sun, and J. Cooper, “Lqg based model predictive control for gust load alleviation,” *Aerospace Science and Technology*, vol. 71, pp. 499–509, 2017.
- [94] K. Shao, Z. Wu, C. Yang, L. Chen, and B. Lv, “Design of an adaptive gust response alleviation control system: simulations and experiments,” *Journal of Aircraft*, vol. 47, no. 3, pp. 1022–1029, 2010.
- [95] Z. Qu, E. Lavretsky, and A. M. Annaswamy, “An adaptive controller for very flexible aircraft,” in *AIAA Guidance, Navigation, and Control Conference*, (Boston, Massachusetts, USA), August 2013.
- [96] H. Benaroya and T. Wei, “Hamilton’s principle for external viscous fluid-structure interaction,” *Journal of Sound and Vibration*, vol. 238, no. 1, pp. 113–145, 2000.

- [97] A. Wynn, Y. Wang, R. Palacios, and P. J. Goulart, “An energy-preserving description of nonlinear beam vibrations in modal coordinates,” *Journal of Sound and Vibration*, vol. 332, no. 21, pp. 5543–5558, 2013.
- [98] R. Palacios and B. Epureanu, “An intrinsic description of the nonlinear aeroelasticity of very flexible wings,” in *52nd AIAA/ASME/ASCE/AHS/ASC Structures, Structural Dynamics and Materials Conference 19th AIAA/ASME/AHS Adaptive Structures Conference 13t*, (Denver, Colorado, USA), April 2011.
- [99] B. Cockburn, S. Hou, and C. Shu, “The runge-kutta local projection discontinuous galerkin finite element method for conservation laws. iv. the multidimensional case,” *Mathematics of Computation*, vol. 54, no. 190, pp. 545–581, 1990.
- [100] H. G. Matthies and M. Meyer, “Nonlinear galerkin methods for the model reduction of nonlinear dynamical systems,” *Computers & structures*, vol. 81, no. 12, pp. 1277–1286, 2003.
- [101] B. Raghavan and M. J. Patil, “Flight control for flexible, high-aspect-ratio flying wings,” *Journal of Guidance, Control, and Dynamics*, vol. 33, pp. 64–74, 2010.
- [102] M. J. Dillsaver, C. E. Cesnik, and I. V. Kolmanovsky, “Trajectory control of very flexible aircraft with gust disturbance,” in *AIAA Atmospheric Flight Mechanics Conference*, (Boston, Massachusetts, USA), August 2013.
- [103] A. Dorobantu, A. Murch, and G. Balas, “H-infinity robust control design for the NASA AirSTAR flight test vehicle,” in *50th AIAA Aerospace Sciences Meeting including the New Horizons Forum and Aerospace Exposition*, (Nashville, Tennessee, USA), January 2012.
- [104] A. Marcos and M. Sato, “Flight testing of an structured H-infinity controller: An EU-Japan collaborative experience,” in *2017 IEEE Conference on Control Technology and Applications*, (Mauna Lani, Hawaii, USA), August 2017.
- [105] X. Shao, J. Liu, H. Cao, C. Shen, and H. Wang, “Robust dynamic surface trajectory tracking control for a quadrotor uav via extended state observer,” *International Journal of Robust and Nonlinear Control*, vol. 28, no. 7, pp. 2700–2719, 2018.

- [106] J. Gadewadikar, F. Lewis, K. Subbarao, and B. M. Chen, "Structured H-infinity command and control-loop design for unmanned helicopters," *Journal of Guidance, Control, and Dynamics*, vol. 31, no. 4, pp. 1093–1102, 2008.
- [107] Z. Yang, R. Huang, Y. Zhao, and H. Hu, "Design of an active disturbance rejection control for transonic flutter suppression," *Journal of Guidance, Control, and Dynamics*, vol. 40, no. 11, pp. 2905–2916, 2017.
- [108] Z. Wang, R. Zu, D. Duan, and J. Li, "Tuning of ADRC for QTR in transition process based on NBPO hybrid algorithm," *IEEE Access*, vol. 7, pp. 177219–177240, 2019.
- [109] Q. Mao, L. Dou, Q. Zong, and Z. Ding, "Attitude controller design for reusable launch vehicles during reentry phase via compound adaptive fuzzy H-infinity control," *Aerospace Science and Technology*, vol. 72, pp. 36–48, 2018.
- [110] H.-C. Kim, H. R. Dharmayanda, T. Kang, A. Budiyo, G. Lee, and W. Adiprawita, "Parameter identification and design of a robust attitude controller using H_∞ methodology for the raptor E620 small-scale helicopter," *International Journal of Control, Automation and Systems*, vol. 10, no. 1, pp. 88–101, 2012.
- [111] F. Boeren, R. van Herpen, T. Oomen, M. van de Wal, and O. Bosgra, "Enhancing performance through multivariable weighting function design in h_∞ loop-shaping: with application to a motion system," in *2013 American Control Conference*, (Washington, DC, USA), June 2013.
- [112] J. Kennedy and R. Eberhart, "Particle swarm optimization," in *Proceedings of International Conference on Neural Networks*, vol. 4, pp. 1942–1948, 1995.
- [113] I. C. Trelea, "The particle swarm optimization algorithm: convergence analysis and parameter selection," *Information processing letters*, vol. 85, no. 6, pp. 317–325, 2003.
- [114] R. Eberhart and J. Kennedy, "Particle swarm optimization," in *Proceedings of the IEEE international conference on neural networks*, vol. 4, pp. 1942–1948, 1995.
- [115] Z. Gao, "Scaling and bandwidth-parameterization based controller tuning," in *Proceedings of the American control conference*, (Denver, Colorado, USA), June 2003.

- [116] Y. Wang, Z. Cui, X. Fang, B. Tian, and Y. Wang, “A lateral guidance algorithm for unmanned aerial vehicle,” *China Patent*, no. CN101266150A.
- [117] Boeing, “Statistical summary of commercial jet airplane accidents 1959-2015,” *Technical report*, Aviation Safety Boeing Commercial Airplanes, Seattle, Washington, USA, July 2016.
- [118] S. Lee, J. Lee, S. Lee, H. Choi, Y. Kim, S. Kim, and J. Suk, “Sliding mode guidance and control for uav carrier landing,” *IEEE Transactions on Aerospace and Electronic Systems*, vol. 55, no. 2, pp. 951–966, 2018.
- [119] R. Lungu, M. Lungu, and L. T. Grigorie, “Automatic control of aircraft in longitudinal plane during landing,” *IEEE Transactions on Aerospace and Electronic Systems*, vol. 49, no. 2, pp. 1338–1350, 2013.
- [120] Z. Zhen, S. Jiang, and J. Jiang, “Preview control and particle filtering for automatic carrier landing,” *IEEE Transactions on Aerospace and Electronic Systems*, vol. 54, no. 6, pp. 2662–2674, 2018.
- [121] D. Zhang and X. Wang, “Autonomous landing control of fixed-wing uavs: from theory to field experiment,” *Journal of Intelligent & Robotic Systems*, vol. 88, pp. 619–634, 2017.
- [122] C. Chen, W.-Q. Tan, X.-J. Qu, and H.-X. Li, “A fuzzy human pilot model of longitudinal control for a carrier landing task,” *IEEE Transactions on Aerospace and Electronic Systems*, vol. 54, no. 1, pp. 453–466, 2018.
- [123] Z. Zheng, Z. Jin, L. Sun, and M. Zhu, “Adaptive sliding mode relative motion control for autonomous carrier landing of fixed-wing unmanned aerial vehicles,” *IEEE Access*, vol. 5, pp. 5556–5565, 2017.
- [124] C. Chen, W.-Q. Tan, X.-J. Qu, and H.-X. Li, “A fuzzy human pilot model of longitudinal control for a carrier landing task,” *IEEE Transactions on Aerospace and Electronic Systems*, vol. 54, no. 1, pp. 453–466, 2017.
- [125] T. Woodbury and J. Valasek, “Synthesis and flight test of automatic landing controller using quantitative feedback theory,” *Journal of Guidance, Control, and Dynamics*, vol. 39, no. 9, pp. 1994–2010, 2016.
- [126] P. Castillo, L. E. Munoz, and O. Santos, “Robust control algorithm for a rotorcraft disturbed by crosswind,” *IEEE Transactions on Aerospace and Electronic Systems*, vol. 50, no. 1, pp. 756–763, 2014.

- [127] H. Sadat-Hoseini, S. Fazelzadeh, A. Rasti, and P. Marzocca, “Final approach and flare control of a flexible aircraft in crosswind landings,” *Journal of Guidance, Control, and Dynamics*, vol. 36, no. 4, pp. 946–957, 2013.
- [128] N. Angelou, J. Mann, M. Courtney, and M. Sjöholm, “Doppler lidar mounted on a wind turbine nacelle,” *Spectrum*, vol. 100, pp. 1–46, 2010.
- [129] P. Towers and B. L. Jones, “Real-time wind field reconstruction from lidar measurements using a dynamic wind model and state estimation,” *Wind Energy*, vol. 19, no. 1, pp. 133–150, 2016.
- [130] M. J. Kavaya, J. Y. Beyon, G. J. Koch, M. Petros, P. J. Petzar, U. N. Singh, B. C. Trieu, and J. Yu, “The doppler aerosol wind (dawn) airborne, wind-profiling coherent-detection lidar system: overview and preliminary flight results,” *Journal of Atmospheric and Oceanic Technology*, vol. 31, no. 4, pp. 826–842, 2014.
- [131] G. Teschke and V. Lehmann, “Mean wind vector estimation using the velocity–azimuth display (vad) method: an explicit algebraic solution,” *Atmospheric Measurement Techniques*, vol. 10, no. 9, pp. 3265–3271, 2017.
- [132] K. Takaba, “A tutorial on preview control systems,” in *SICE 2003 Annual Conference*, (Fukui University, Japan), IEEE, 2003.
- [133] J. Laks, L. Pao, A. Wright, N. Kelley, and B. Jonkman, “The use of preview wind measurements for blade pitch control,” *Mechatronics*, vol. 21, no. 4, pp. 668–681, 2011.
- [134] X. Tong and X. Zhao, “Power generation control of a monopile hydrostatic wind turbine using an h_∞ loop-shaping torque controller and an lpv pitch controller,” *IEEE Transactions on Control Systems Technology*, vol. 26, no. 6, pp. 2165–2172, 2017.
- [135] D. Schlipf, D. J. Schlipf, and M. Kühn, “Nonlinear model predictive control of wind turbines using lidar,” *Wind Energy*, vol. 16, no. 7, pp. 1107–1129, 2013.
- [136] N. Wang, K. E. Johnson, and A. D. Wright, “Fx-rls-based feedforward control for lidar-enabled wind turbine load mitigation,” *IEEE Transactions on Control Systems Technology*, vol. 20, no. 5, pp. 1212–1222, 2011.
- [137] T. Mikkelsen, N. Angelou, K. Hansen, M. Sjöholm, M. Harris, C. Slinger, P. Hadley, R. Scullion, G. Ellis, and G. Vives, “A spinner-integrated wind lidar

- for enhanced wind turbine control,” *Wind Energy*, vol. 16, no. 4, pp. 625–643, 2013.
- [138] G. J. Rabadan, N. P. Schmitt, T. Pistner, and W. Rehm, “Airborne lidar for automatic feedforward control of turbulent in-flight phenomena,” *Journal of Aircraft*, vol. 47, no. 2, pp. 392–403, 2010.
 - [139] H. Giessler, M. Kopf, T. Faulwasser, P. Varutti, and R. Findeisen, “Gust load alleviation based on model predictive control,” in *International Forum on Aeroelasticity and Structural Dynamics*, (Bristol, UK), June 2013.
 - [140] Y. Paku, T. Shimomura, and Y. Hamada, “Gain-scheduled preview control for aircraft gust alleviation,” in *55th Annual Conference of the Society of Instrument and Control Engineers of Japan*, (Tsukuba, Japan), September 2016.
 - [141] Y. Wang, F. Li, and A. Da Ronch, “Adaptive feedforward control design for gust loads alleviation of highly flexible aircraft,” in *AIAA Atmospheric Flight Mechanics Conference*, (Dallas, Texas, USA), June 2015.
 - [142] M. Green and D. J. Limebeer, *Linear robust control*. Courier Corporation, 2012.
 - [143] D. Schlipf, E. Simley, F. Lemmer, L. Pao, and P. W. Cheng, “Collective pitch feedforward control of floating wind turbines using lidar,” *Journal of Ocean and Wind Energy*, vol. 2, no. 4, pp. 223–230, 2015.
 - [144] D. Schlipf, J. J. Trujillo, V. Basterra, and M. Kühn, “Development of a wind turbine lidar simulator,” in *2009 European Wind Energy Conference*, (Parc Chanot, Marseille, France), March 2009.
 - [145] G. I. Taylor, “The spectrum of turbulence,” *Proceedings of the Royal Society of London. Series A, Mathematical and Physical Sciences*, vol. 164, no. 919, pp. 476–490, 1938.
 - [146] G. H. Golub and C. F. Van Loan, “Matrix computations, johns hopkins u,” *Math. Sci., Johns Hopkins University Press, Baltimore, MD*, 1996.
 - [147] A. Hazell and D. J. Limebeer, “An efficient algorithm for discrete-time h^∞ preview control,” *Automatica*, vol. 44, no. 9, pp. 2441–2448, 2008.

- [148] A. Hazell, “Discrete-time optimal preview control,” Ph.D. thesis, The Department of Electrical and Electronic Engineering, Imperial College, London, 2008.
- [149] E. Cheynet, “Wind field simulation (windsim).” <https://uk.mathworks.com/matlabcentral/fileexchange/50041-wind-field-simulation?focused=6398534&tab=function>. Last updated June 3, 2016.
- [150] D. Moorhouse and R. Woodcock, “US Military Specification MIL-F-8785C,” 1980.
- [151] P. Qi, X. Zhao, Y. Wang, R. Palacios, and A. Wynn, “Aeroelastic and trajectory control of high altitude long endurance aircraft,” *IEEE Transactions on Aerospace and Electronic Systems*, vol. 54, no. 6, pp. 2992–3003, 2018.
- [152] P. Qi, X. Zhao, and R. Palacios, “Autonomous landing control of highly flexible aircraft based on lidar preview in the presence of wind turbulence,” *IEEE Transactions on Aerospace and Electronic Systems*, vol. 55, no. 5, pp. 2543–2555, 2019.
- [153] R. Skelton, “Model error concepts in control design,” *International Journal of Control*, vol. 49, no. 5, pp. 1725–1753, 1989.
- [154] Z. Hou and Z. Wang, “From model-based control to data-driven control: Survey, classification and perspective,” *Information Sciences*, vol. 235, pp. 3–35, 2013.
- [155] Z. Hou and S. Jin, *Model free adaptive control: theory and applications*. CRC press, 2013.
- [156] Z. Hou, R. Chi, and H. Gao, “An overview of dynamic-linearization-based data-driven control and applications,” *IEEE Transactions on Industrial Electronics*, vol. 64, no. 5, pp. 4076–4090, 2017.
- [157] Z. Hou and S. Jin, “A novel data-driven control approach for a class of discrete-time nonlinear systems,” *IEEE Transactions on Control Systems Technology*, vol. 19, no. 6, pp. 1549–1558, 2011.
- [158] Z. Hou and S. Jin, “Data-driven model-free adaptive control for a class of mimo nonlinear discrete-time systems,” *IEEE Transactions on Neural Networks*, vol. 22, no. 12, pp. 2173–2188, 2011.

- [159] Z. Hou and X. Bu, "Model free adaptive control with data dropouts," *Expert Systems with Applications*, vol. 38, no. 8, pp. 10709–10717, 2011.
- [160] X. Bu, Z. Hou, F. Yu, and F. Wang, "Robust model free adaptive control with measurement disturbance," *IET control theory & applications*, vol. 6, no. 9, pp. 1288–1296, 2012.
- [161] X. Bu, F. Yu, Z. Hou, and H. Zhang, "Model-free adaptive control algorithm with data dropout compensation," *Mathematical Problems in Engineering*, vol. 2012, pp. 1–14, 2012.
- [162] S. Park, J. Deyst, and J. P. How, "Performance and Lyapunov stability of a nonlinear path following guidance method," *Journal of Guidance, Control, and Dynamics*, vol. 30, no. 6, pp. 1718–1728, 2007.
- [163] B. Guo and Z. Zhao, "On convergence of tracking differentiator," *International Journal of Control*, vol. 84, no. 4, pp. 693–701, 2011.
- [164] X. Bu, X. Wu, R. Zhang, Z. Ma, and J. Huang, "Tracking differentiator design for the robust backstepping control of a flexible air-breathing hypersonic vehicle," *Journal of the Franklin Institute*, vol. 352, no. 4, pp. 1739–1765, 2015.
- [165] X. Wang, S. Yau, and J. Huang, "A study of tracking-differentiator," in *Proceedings of the 39th IEEE Conference on Decision and Control*, (Sydney, New South Wales, Australia), December 2000.